A MULTIBAND INDUCTIVE WIRELESS LINK FOR IMPLANTABLE MEDICAL DEVICES AND SMALL FREELY BEHAVING ANIMAL SUBJECTS

A Dissertation
Presented to
The Academic Faculty

by

Uei-Ming Jow

In Partial Fulfillment
of the Requirements for the Degree
Doctor of Philosophy in the
School of Electrical and Computer Engineering

Georgia Institute of Technology
May 2013

Copyright © 2013 by Uei-Ming Jow

A MULTIBAND INDUCTIVE WIRELESS LINK FOR IMPLANTABLE MEDICAL DEVICES AND SMALL FREELY BEHAVING ANIMAL SUBJECTS

Approved by:

Dr. Maysam Ghovanloo, Advisor
School of Electrical and Computer Engineering
Georgia Institute of Technology

Dr. Pamela T. Bhatti
School of Electrical and Computer Engineering
Georgia Institute of Technology

Dr. Gregory D. Durgin
School of Electrical and Computer Engineering
Georgia Institute of Technology

Dr. Mary A. Weitnauer
School of Electrical and Computer Engineering
Georgia Institute of Technology

Dr. Joseph R. Manns
Department of Psychology
Emory University

Date Approved: January 9, 2013

To my family, friends, and loved ones

ACKNOWLEDGEMENTS

I would like to express my deepest gratitude to my advisor, Dr. Maysam Ghovanloo for his guidance and generous support. Indeed, it is my greatest honor and pleasure to work under his supervision for my Ph.D. research. His dedication to research, teaching, and students, has truly inspired and influenced me in many ways. If I ever become an educator one day, part of the reason will be because of him. I used to work with engineers, but now I enjoy working more with graduate students.

I would like to thank Dr. Pamela T. Bhatti for taking time to serve as the chair of my Ph.D proposal examination. Dr. Bhatti has been really helpful and approachable during this stressful period. In addition, I am grateful to the rest of my committee members, Dr. Gregory D. Durgin and Dr. Mary A. Ingram. They have been generous in sharing their expertise and suggestions, which helped to further improve my research.

It has been a very long trip. There are so many people to thank, but I would like to start by thanking all the people from my ex- and present colleagues from GT-Bionics for their contributions. My dissertation would never have completed without their support over the years. It was a great pleasure and a fun experience working with them. I wish to extend my thanks to Dr. Joseph Manns in Emory University for his help for the animal experiment and sharing his experience and suggestions for the neural sciences.

I want to express my sincerest gratitude to my family for being so supportive of me over all these years. Lastly, I would like to thank my wife, Ms. Tzuchi Lin, for her patience, understanding, and support. She is indeed a gift from God. I could not have done it without you. I love you.

TABLE OF CONTENTS

LIST OF TABLES

Page

LIST OF FIGURES

Page

SYMBOLS AND ABBREVIATIONS

Physical parameters

d_o	Outer diameter of the coil
d_i	Inner diameter of the coil
d_{avg}	Averaging of the diameter of coil $d_{avg} = (d_o + d_i)/2$
φ	Fill factor, $\varphi = (d_o - d_i)/(d_o + d_i)$
w	Wire width
s	Spacing
l	Length
Dia	Wire diameter
n	Number of turns
D	Coupling distance
t_{sub}	Substrate thickness
t_0	Metal thickness
γ	Lateral misalignment (max)
W	Weight
ω	Frequency ($\omega=2\pi f$)
Θ	Spherical coordinate system of Θ direction
Φ	Spherical coordinate system of Φ direction
Den	Mass density
A	Area
g	Geometrical coefficient

Electrical parameters

Q	Quality factor
k	Coupling coefficient
ε	Dielectric constant (F/m, farad per meter)
ε_o	Dielectric constant of free space (F/m, farad per meter)
ε_r	Relative constant
μ	Permeability (H/m, henry per meter)
μ_o	Permeability of free space (H/m, henry per meter)
μ_r	Relative permeability
$tan(\delta)$	Dielectric loss tangent
DF	Dielectric loss factor
ρ	Resistivity, $\rho=1/\sigma$ (Ω·m, ohm·meter)
σ	Conductivity, $\sigma =1/\rho$ (S/m, siemens per meter)
δ	Skin depth (m, meter)
R	Resistance (Ω, ohm)
G	Conductance (S, siemens)
Z	Impedance (Ω, ohm)
L	Inductance (H, Henry)
C	Capacitance (F, Farad)
M	Mutual inductance (H, Henry,)
η	Power transfer efficiency (PET)

SUMMARY

The objective of this research is to introduce two state-of-the-art wireless biomedical systems: (1) a multiband transcutaneous communication system for implantable microelectronic devices (IMDs) and (2) a new wireless power delivery system, called the "EnerCage," for experiments involving freely-behaving animals. The wireless multiband link for IMDs achieves power transmission via a pair of coils designed for maximum coupling efficiency. The data link is able to handle large communication bandwidth with minimum interference from the power-carrier thanks to its optimized geometry. Wireless data and power links have promising prospects for use in biomedical devices such as biosensors, neural recording, and neural stimulation devices. The EnerCage system includes a stationary unit with an array of coils for inductive power transmission and three-dimensional magnetic sensors for non-line-of-sight tracking of animal subjects. It aims to energize novel biological data-acquisition and stimulation instruments for long-term experiments, without interruption, on freely behaving small animal subjects in large experimental arenas. The EnerCage system has been tested in one-hour *in vivo* experiment for wireless power and data communication, and the results show the feasibility of this system.

The contributions from this research work are summarized as follows:

1. Development of an inductive link model.
2. Development of an accurate PSC models, with parasitic effects for implantable devices.
3. Proposing the design procedure for the inductive link with optimal physical geometry to maximize the PTE.

4. Design of novel antenna and coil geometry for wireless multiband link: power carrier, forward data link, and back telemetry.
5. Development of a model of overlapping PSCs, which can create a homogenous magnetic in a large experimental area for wireless power transmission at a certain coupling distance.
6. Design and optimization for multi-coil link, which can provide optimal load matching for maximum PTE.
7. Design of the wireless power and data communication system for long-term animal experiments, without interruption, on freely behaving small animal subjects in any shape of experimental arenas.

CHAPTER I

INTRODUCTION

Wireless biomedical communication efforts attempt to meet the device design requirements of minimizing the size, maximizing the performance, and minimizing the power consumption of the system while assuring user safety. Most of wireless devices require a battery [1] that increases the weight and needs to be replaced regularly. Consequently, over the past few decades, researchers have focused on wireless data and power transmission for biomedical devices to overcome the limits of the batteries. However, wireless power is associated with three issues: low power efficiency, short transmission distance, and high electromagnetic interference. The objective of this research includes two categories to solve these problems: an optimized multiband (data and power channels) telemetry module for implantable microelectronic devices (IMDs) and a novel monitoring system using wireless power on a freely behaving animal in large experimental arenas.

1.1 Multiband Transmission for Implantable Devices

The multiband transmission for IMDs is necessary for clinical applications to reduce the patients' risk of infection and discomfort. Therefore, the proposed IMD wireless link is expected to perform three functions [2], [3]:

(1) Power transmission (inductive link): Since the long-term power consumption of IMDs is higher than what a battery can provide, an efficient wireless power transmission from outside into the human body is the most suitable solution. Even if the battery is placed outside the body, it needs to be small and light and have a long lifetime [1]. Hence, an iterative design methodology to find the geometric parameters of the planar spiral

coils (PSC) [5]–[8] with the maximum power transmission efficiency is proposed. In the real application, implantable devices need to be hermetically sealed in biocompatible materials and placed in a conductive environment with high permittivity (tissue), which can affect the PSC characteristics. A detailed model that includes the effects of the surrounding environment on the PSC parasitic components is constructed for the maximum power transfer efficiency (PTE). This model is combined with an iterative design method that starts with a set of realistic design constraints and ends with the optimal PSC geometries.

(2) Forward data transmission (inductive link): The stimulation data should be transmitted to the IMD of the body from the external device. However, because of the conflicting requirements between power and data by the inductive links, a separate pair of coils for data transmission is used, and two types of data coils with minimum interference are proposed. First, a pair of vertical coils is wound across the diameter of the power PSCs [9], whose orthogonal magnetic field orientation can minimize the interference of the power carrier. Second, a pair of planar figure-eight (figure-8) coils, which is similar to the numerical symbol of eight (8) [10], has the electromotive force (EMF) induced from the power carrier in one loop and opposes the same in the other loop. Hence, the total EMF interference from the power carrier can be very small when the two coils are aligned.

(3) Back telemetry (wideband antenna): Recording the neural response to the stimulation in neuroprostheses and closing the control feedback loop in the brain machine interface (BMI) require a wideband back telemetry. Therefore, the impulse-radio ultra-

wideband (IR-UWB) [11] communication, which can provide a wide bandwidth with a simple and low-power transmitter, is most suitable for this purpose.

Figure 1.1 shows the block diagram of a high-performance neuroprosthetic device that has wireless neural recording and stimulation capabilities with emphasis on the proposed multiband wireless link. The external power PSC is L_1 and the internal power PSC is L_2; the latter is implanted under the skin flap. The forward data coils are L_3 and L_4. The back telemetry utilizes the UWB antennas, A1 and A2.

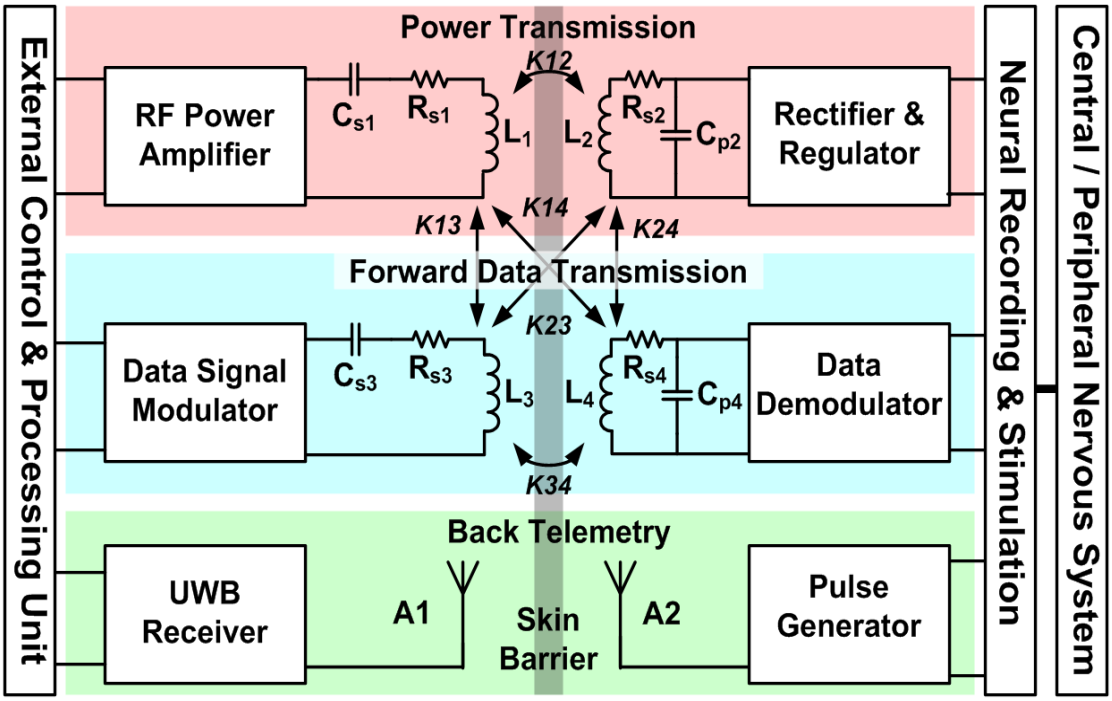

Figure 1.1: Block diagram of the multiband wireless link in a high-performance IMD.

1.2 EnerCage

Another topic of the research is monitoring the freely behaving animal by the continuously wireless power transmission for the wireless neural recording and stimulation systems [12] to overcome the limits of the battery power [13]–[16]. A battery increases the size and weight of the wireless system [17]. Moreover, users of such

systems always have to make a compromise between the duration of the experiment and how much payload the animal can carry. Hence, the proposed system, called EnerCage, allows neuroscientists to continuously run the neural interfaces without replacing the batteries. EnerCage is used to develop an *in vivo* electrophysiology data-acquisition system that transmits the recorded signals wirelessly and also receives its power wirelessly. Two key features of the EnerCage system are (1) inductive powering through a scalable array of modular PSCs that can conform to any recording arena and (2) accurate position/orientation tracking of an animal's head in three-dimension (3-D) [18] when using an array of magnetic sensors. Geometry of the PSC array, shown in Figure 1.2, which tiles the floor of the arena will be optimized for minimum coupling variations and maximum PTE at a nominal coupling distance that depends on the average size of the animal model [23]. A closed-loop power control (CLPC) mechanism based on radio-frequency identification (RFID) technology will maintain the received power across the Rx coil constant most of the times except when the coil is rotated > 60° or the animal stands on its rear limbs. In these conditions, the power management circuit uses its internal power storage to prevent any possible interruptions.

The system will also track the animal position in real time using an array of three-axial magnetic sensor modules (the red dots in Figure 1.2) [20], [21]. The magnetic tracking algorithm [18], [19] provides valuable information, which is not only important from behavioral perspective but also necessary in activating the Tx coil that is in the best position to couple onto the Rx coil(s). Furthermore, unlike the optical tracking method, the magnetic 3D tracking can operate in both open and covered spaces, such as tunnels, which might be a more natural environment for burrowing animals.

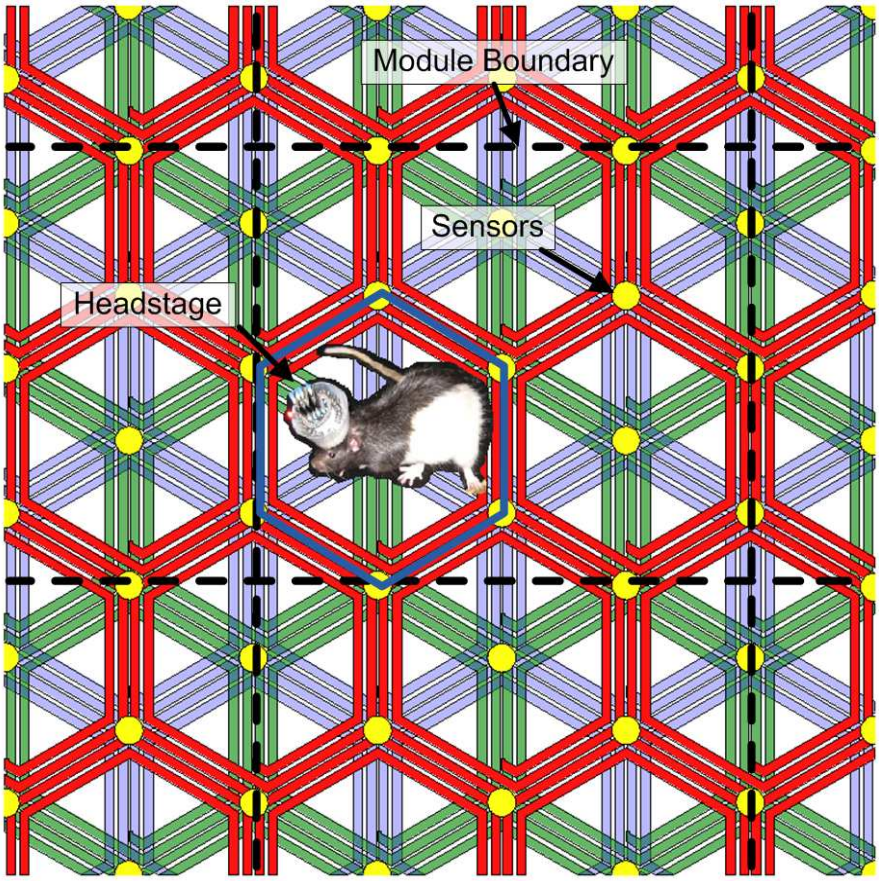

Figure 1.2: Top view rendering of an overlapping planar hexagonal PSC array designed to generate a homogeneous magnetic field for wireless power transmission to one or more awake freely behaving small animal subject(s).

Therefore, the EnerCage system can overcome the major limitations of existing neural-recording instrumentation that use a cable connection. The EnerCage system is meant to allow researchers to create natural and enriched environments for small freely behaving animal subjects, and run experiments for virtually unlimited time periods without worrying about the potential bias from tethering effects and heavy payloads.

The structure of the thesis is as follows: In Chapter 2, a background on wireless power and data combination for biomedical application is introduced. It includes the system review and the related coil/antenna design. In Chapter 3 [4]-[8], a model of the PSC for wireless power is discussed, and the model considers all of the possible parasitic

components, which are affected by the environment. An iterative design methodology to maximize their PTE for PSCs is also concluded in Chapter 3. In Chapter 4 [3], [4], a multiband module design, which includes power carrier, forward link, and back telemetry is introduced, and the optimal data coils with minimum interference from power carrier is also studied. The EnerCage system is presented in Chapter 5 to 7. The system architecture of preliminary EnerCage is presented in Chapter 5 [20]–[22]. This system includes magnetic sensor tracking [19] and closed-loop power regulation. Chapter 6 [23] describes the optimal PSC array design, this array can minimum the coupling variation. In other words, the homogenous magnetic can provide a stable wireless power for long-term animal experiment. In Chapter 7, an improved EnerCage system is discussed, and the freely moving animal experiment is presented. Finally, the contributions of this dissertation and suggested the future works are summarized in Chapter 8.

CHAPTER II

BACKGROUND

2.1 Wireless Link for Implantable Devices

Traditional IMDs have transcutaneous wires breaching skin, and this kind of communication could cause the risk of infection and discomfort. Hence, a wireless operation for power, forward link, and back telemetry transmission is necessary for three reasons: (1) it is safer, (2) it is more robust, (3) and it is less likely to be damaged. Another important requirement, which has made IMDs applicable to the treatment of a growing number of ailments, is its minimal invasion. Examples of such IMDs include cochlear implants [1], invasive BMIs [24], and retinal implants [25]–[26]. In Section 2.1, the modern techniques of wireless capabilities, such as those used for the IMDs, are introduced.

2.1.1 Wireless Power

Three major techniques of wireless power transmission are applied for modern IMDs: ultrasonic transmission, high-frequency electromagnetic wave transmission, inductive coupling transmission.

2.1.1.1 Ultrasonic Transmission

Since the human body is made up of approximately 60% water, which attenuates the electromagnetic wave greatly [27]–[29], wireless power transmission by ultrasound is studied in [30]–[31]. However, ultrasonic wireless power is only promising for low-power consumption applications with low efficiency (39% at 10 mm) [32]–[34]. The size of some ultrasonic systems is still too large for implants [30] as shown in Figures 2.1a

and 2.1b. Although [33] provides a novel two degrees-of-freedom device shown in Figures 2.1c and 2.1d, the power absorption of this energy converter is only 21.4 nW.

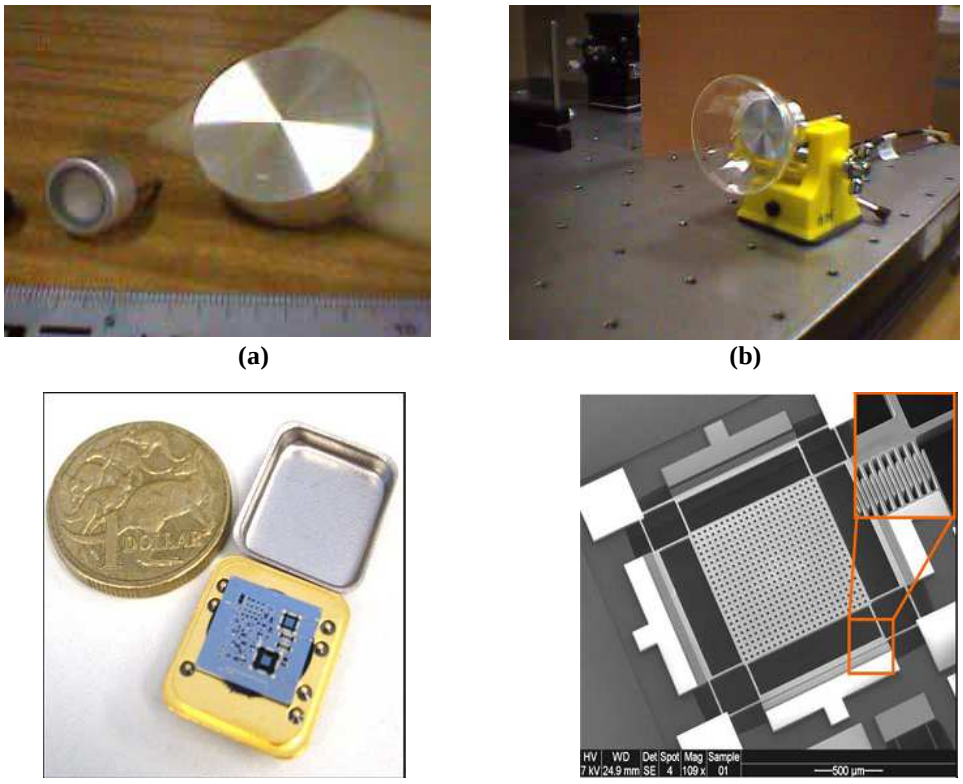

Figure 2.1: (a) The ultrasonic air transducer (left: open-type, right: enclosed-type); (b) plastic horn for transmitter [30]; (c) the ultrasonic converter [33]; (d) the packaged ultrasonic power converter [33].

2.1.1.2 High-frequency Electromagnetic Wave Transmission

The techniques used for wireless power transfer by means of high-frequency electromagnetic wave are summarized in [35]. Ultra high frequency (UHF) radio frequency identification (RFID) technology is one of the methods that offer a reliable link over large distances [36], and several companies also provide the commercial products for the wireless power link for UHF band [37], [38]. However, the received power by the high-frequency antenna is small with low power transfer efficiency (PTE) [37]–[41]. For example, the product of [37] only provides the power less than 5 mW.In fact, UHF

systems outperform (high frequency) HF systems in terms of read range. For many applications read range might be essential, but if low costs and high reliability for low-range reading are important, HF systems are often preferred. Furthermore, with the increase in frequency, the electric field radiated by the antenna of the IMDs increases the ohmic losses of the tissue [27]–[29] and increases the temperature, which is dangerous.

2.1.1.3 Inductive Coupling

The inductive power-transfer system is defined as a system where energy is transferred from a primary winding to a secondary winding by a magnetic field. In the early 20th century, Nikola Tesla [42] devoted much effort toward schemes to transport power wirelessly by Tesla coils, and the past decade has witnessed a surge in the use of such autonomous electronic devices [43]–[46]. Several companies also develop the wireless power products by inductive coupling [47]–[53] for HF band. The quick decay of received power of HF system is often exploited to restrict the read range to a defined region. For RFID applications, interrogator coil arrangements can be optimized to produce a uniformly distributed magnetic field which allows achieving reliable transponder recognition within a defined area of operation. The first developed inductive links for biomedical applications was introduced in the 1960s and focused on artificial heart systems [54]. The advantage of inductive wireless power includes the following: low cost and high efficiency. The drawbacks to inductive wireless power include (1) that the amount of power is limited to the coil geometries; (2) that the power transmission can only be accomplished at certain distances (less than one meter) [55]; (3) the coil design is based on the 2-coil coupling, which could not provide maximum wireless power transfer efficiency (PTE) [56]. Hence, the new design procedure [5] for high coupling efficiency

with small geometry for the biomedical applications is proposed to overcome the drawbacks.

2.1.2 Wireless Power Optimal Coil for Implantable Devices

The inductive power transmission for the IMD belongs to a broader category of implantable devices known as neuroprostheses and has prevented the use of batteries as the main energy source. Instead, the battery is kept out of the patient's body, and the power is delivered wirelessly across the skin through a pair of coupled coils [57]. The external part of the cochlear implants, for instance, should fit comfortably behind the user's ears. Consequently, the efficiency of the transmission from the external battery to the implanted electronic load should be maximized to extend the battery lifetime. Another motivation for achieving high efficiency is to limit the allowable tissue exposure to the alternating magnetic field which can result in excessive heat dissipation [58]–[59]. On the other hand, the interference between the RF link and other nearby electronic devices and appliances is also a concern that is regulated by the IEEE standard of the exposure [60].

2.1.2.1 Printed Spiral Coil (PSC)

Although the distance of inductive coupling is short, the coupling efficiency could be decreased because of the small coil size. These are some of the reasons why the design and optimization of the efficient inductive links have been studied over the last decades [57], [61]–[64]. More recently, a number of publications have presented new approaches to the optimization problems [65]–[68]. The traditional designs of the inductive link [62]–[63] have been based on coils made of filament wires in the form of either a single or multiple individually insulated strands. The latter type, which is known as Litz wire,

helps in reducing skin-loss resistive effects by increasing the circumferential area of the wire [69]–[70], but the wire-wound coils cannot be fabricated without sophisticated machinery. From [14], an inductively powered neural recording system is designed for a short range (< 30 mm), and the coil is made by wire-wound as shown in Figure 2.2a. The need for small footprints in the next generation of high-performance IMDs calls for geometrical precision for integration of the chip or package. This demand requires microfabrication techniques that result in lithographically defined planar structures known as the printed spiral coils (PSCs). The PSCs have the ability to conform to the body curvature with thin flexible substrates [71] as shown in Figure 2.2b, and the hermetically sealed PSCs can also be fabricated on the silicon chips or the low temperature co-fired ceramic (LTCC) packages [72]–[74]. Hence, the PSCs are the most suitable coil type for IMDs [5].

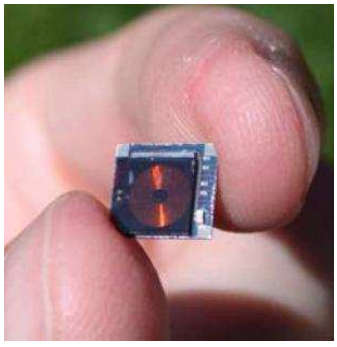

(a)

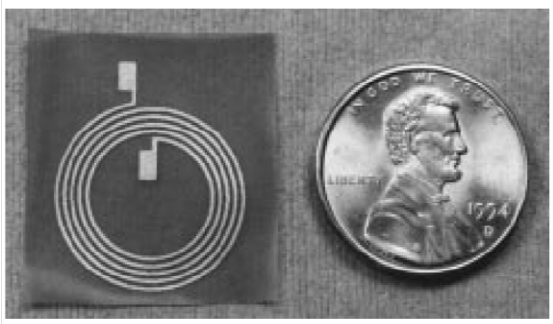

(b)

Figure 2.2: (a) Neural recording implant over a short distance [14]. (b) A 5-turn circular spiral coil fabricated on a flexible and biocompatible polyimide substrate for retinal implant [71].

2.1.2.2 Implantable Devices with Tissue and Package Model

Traditional PSC models [5] do not include the effects of the surrounding environment. Considering the effects of surroundings in PSC models is imperative in the optimization process because the materials affect the PSC parasitic components that decrease transmission efficiency. Several studies use conventional simulation tools [75]–[76] or numerical methods [77] to emulate the surrounding environment for the coil design, but these methods are time consuming. Consequently, physical coil models including the surrounding materials have developed to expedite the PSC optimization procedure [6].

2.1.3 Multiband Design for Implantable Devices

The wireless data link for the IMDs with battery power has been in development for a few decades [78]–[80]. The modern wireless link for the IMDs should include not only the data carrier but also the power carrier. For this reason, multiband techniques started to appear in the late 1980s [81]. In early design [81], [82], the bandwidth of the data transmission was limited because the data and power transmission were on the same frequency. Recently, some researchers [83], [84] operate the power and data carrier in different frequencies, but coils are designed in coaxial type that increases the cross coupling interference as shown in Figure 2.3a. [85] uses the separated coils on the same plane as shown in Figure 2.3b to reduce the interference. But, this design uses three pairs of the coil for each data and power carrier, and the total size of the IMD is increased because of the coil area. Another way for the data transmission is to use the high-frequency antenna [14], but the dielectric losses and wave trapping in the body tissues result in transmission losses [86].

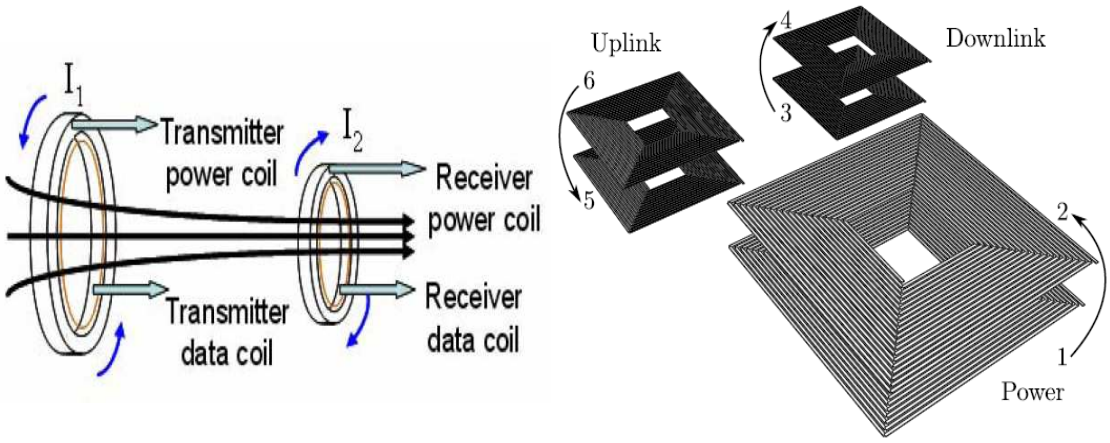

(a) **(b)**

Figure 2.3: (a) Placement of power and data coaxial coils [84]; (b) coplanar coil for multiband link [85].

In this thesis, the data link is separated in two ways, forward and backward, with minimum interference. For the forward data link, two geometries of the data coil with the minimum interference are proposed: the vertical coil [9] and figure-8 coil [87]. On the other hand, for the back telemetry, the impulse-radio ultra-wideband (IR-UWB) [88] is used because of the wide bandwidth with a simple and low-power transmitter.

2.2 Wireless Power for Freely Behaving Animals

A major goal of neuroscience is to study the functional organization of the nervous systems, as this knowledge would aid in the prevention, diagnosis, and treatment of diseases of the human brain. *In vivo* electrophysiology has been a powerful tool in pursuing that goal [89], [90]. Many of these studies are made in experimental animals that are either anesthetized or restrained [91]. However, addressing many experimental questions requires freely behaving subjects to create natural and enriched environments. Thus, the technology for recording of the biological data from biosensors or stimulation of the nerves from electrodes for freely behaving animals can accelerate the contributions of *in vivo* electrophysiology.

2.2.1 Wireless Power in the Animal Experiment

For the neural interface [92]–[96], neuroscientists cannot obtain the benefits of the wireless data-acquisition systems when the animal subjects are tethered to instrumentation through the cables. The use of these cables leads to four problems: the imitated length, the electromagnetic noise, the motion artifacts, and the entangling problem. Since cables produce these problems for animal experiments, the wireless neural recording systems involve batteries. However, the power consumption of the wireless system would limit the duration of each trial before the batteries needed to be recharged or replaced. Consequently, several recent attempts have been made to develop the wireless powered systems and eliminate the power cable or battery.

[97] proposes an array of nine coils, each 5×5 cm^2, at the bottom of a cage to power an implanted 6×6 mm^2 coil. However, this system faces large voltage variations and a significant change in magnetic flux at the edge of the adjacent coils. [98] demonstrates a simple implantable stimulator system in a chamber surrounded by three sets of coils in 3-D geometry. The chamber is only 17×16×16 cm^3 as shown in Figure 2.4a. [99] demonstrates the narrowband wireless system shown in Figure 2.4b for measuring blood pressure with a closed-loop power control. The system, however, has only a single coil and limits the animal's movement to a small cage (10×10×20 cm^3). A commercial telemetric device, called VitalView, has been developed by Mini Mitter Inc. [100]. Dimension of this inductive transceiver is limited to 56×29 cm^2 (Figure 2.4c), and its bandwidth only suits low frequency biological signals such as body temperature or heart rate. Thus, neither commercial tools nor those described in the literature would be suitable for neural interfacing in small freely behaving animals.

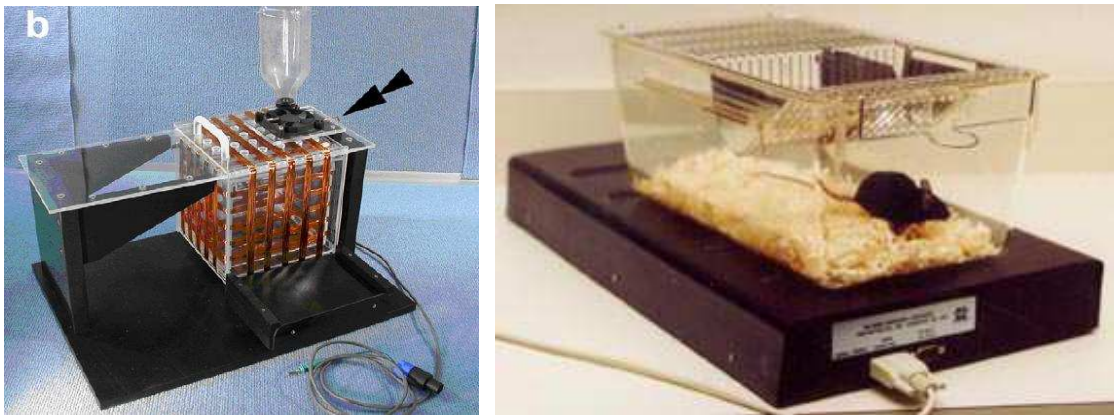

(a) **(b)**

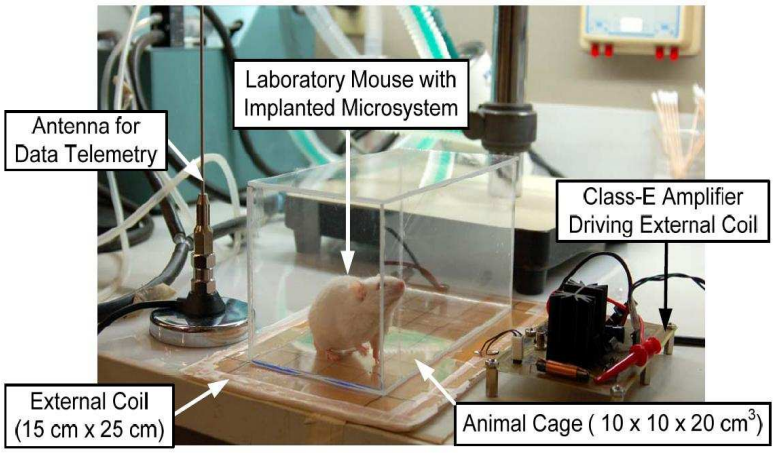

(c)

Figure 2.4: Examples of the existing inductively powered devices: (a) three sets of coils used around a small [98]; (b) wireless measurement of blood pressure [99]; (c) VitalView energizer by Mini Mitter Inc. [101].

2.2.2 Wireless Power System with Coil Array and Tracking

The wireless power for the freely behaving animals is a challenge because the separation between the primary and secondary unit is highly variable. If only one primary coil is used for this application, it becomes difficult to generate a field with sufficient power strength. Since the inductive wireless power area is limited by the coil size, the researchers are attempting to use a coil array to extend the experimental arenas [101]–[104].

For behavioral experiments on mice, rats, or a group of small social animals, such

as prairie voles, using an array of overlapping PSC, similar to the designs adopted for inductive chargers, seem to be advantageous [102], [105]. These 2-D PSCs can be lithographically defined on multilayer printed circuit boards (PCB) and geometrically arranged such that the peaks of the magnetic field generated by one coil overlap the troughs of the surrounding coils. This method can lead to a more uniform magnetic field distribution over a large experimental area. In such arrangements, instead of activating all the Tx coils at once, which results in a high power dissipation and elevated cage temperature, the position of the animal subject should be detected in real time to activate the coil(s) that are in the best position to couple onto the Rx coil and power up the attached instruments [20], [21], [105].

A group of researchers from New Zealand [106] proposed a 3×3 non-overlapping coil array for this application with each coil tuned at a different frequency as shown in Figure 2.5. While this design provided good coverage in the center of the coils, the power delivered to the Rx coil on the corners of each coil was ~20 times less than the center. In a 4-layer array of rectangular overlapping coils as shown in Figure 2.6, presented by the same group [107], the effects of mutual coupling or parasitic capacitance between the overlapping Tx coils were not considered. Moreover, there is a need to establish methods for optimizing the coil geometries for such biomedical and industrial applications while considering the constraints in PSC fabrication process on multilayer PCB to achieve realistic, functional, and cost effective solutions. Hence, the proposed EnerCage system includes an optimized hexagonal PSC array for inductive power transmission with high efficiency in the large experimental arenas and magnetic sensors for accurate tracking of the animal subjects.

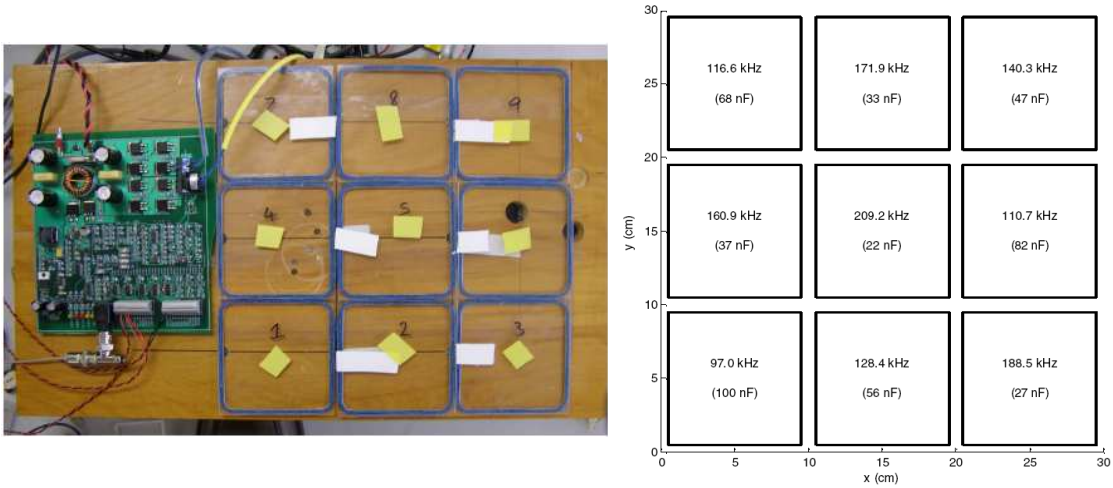

Figure 2.5: Prototype inductively coupled power transfer system with different resonant coils [106].

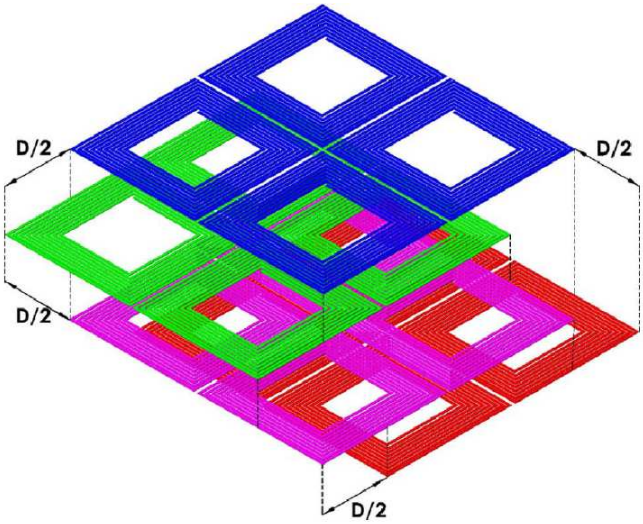

Figure 2.6: An exploded view of a four layer arrangement of PSCs which overlaps the aforementioned regions such that power is available in any orientation [107].

CHAPTER III

OPTIMIZATION OF PLANAR SPIRAL COIL

Wireless operation of implantable microelectronic devices (IMD) is necessary for clinical applications in order to reduce the risk of infection and patient discomfort, which can result from transcutaneous wires breaching the skin. A wireless implant is also safer, more robust, and less likely to be damaged as a result of broken interconnects. Another important requirement, which has made implantable devices applicable to the treatment of a growing number of ailments and conditions such as deafness, blindness, and paralysis, is being minimally invasive, which is a direct consequence of small size.

Unlike pacemakers, high power requirements and extreme size constraints in aforementioned applications, which belong to a broader category of implantable devices known as neuroprostheses, have prevented the use of batteries as the primary source of energy. Instead, the battery is kept out of the patient's body and power is delivered wirelessly across the skin through a pair of inductively coupled coils that constitute a transformer [57]. Even outside of the body, the battery needs to be small, light weight, and have a long lifetime due to portability, aesthetic, and economic reasons. Therefore, the power transmission efficiency (PTE) from the external battery to the implanted electronic load should be maximized to extend the battery lifetime. Another reason is the limited allowable tissue exposure to the AC magnetic fields, which can result in excessive heat dissipation if violated [58], [59]. Interference between the RF link and other nearby communication devices and appliances is also a concern, which is regulated by the federal communications commission (FCC) [60].

Figure 3.1a shows a simplified diagram of the transcutaneous power transfer and various losses along the way as well as the circuit model of the inductive link. The overall power transmission efficiency, $\eta = \eta_S \eta_1 \eta_T \eta_2 \eta_L$, is often dominated by $\eta_{12} = \eta_1 \eta_T \eta_2$, which is related to the coil design [24]. The important parameters of the coil models (Figure 3.2b) include the self inductance (L), parasitic resistance (R), and parasitic capacitance (C). Capacitors C_{S1} and C_2 are also added to form a pair of resonant LC-tank circuits with L_1 and L_2, respectively, at the power carrier-frequency, f_c. The lumped parasitic components of the coil models are influenced by geometry, material composition, and surrounding environment, and the inductive link optimization by the coil models for IMDs is studied.

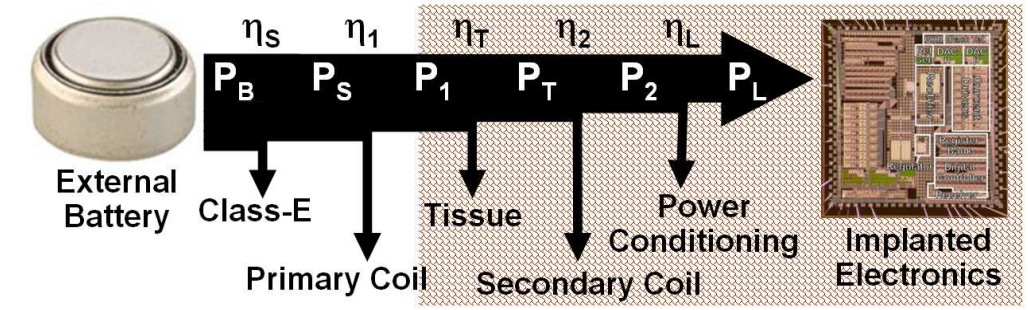

(a)

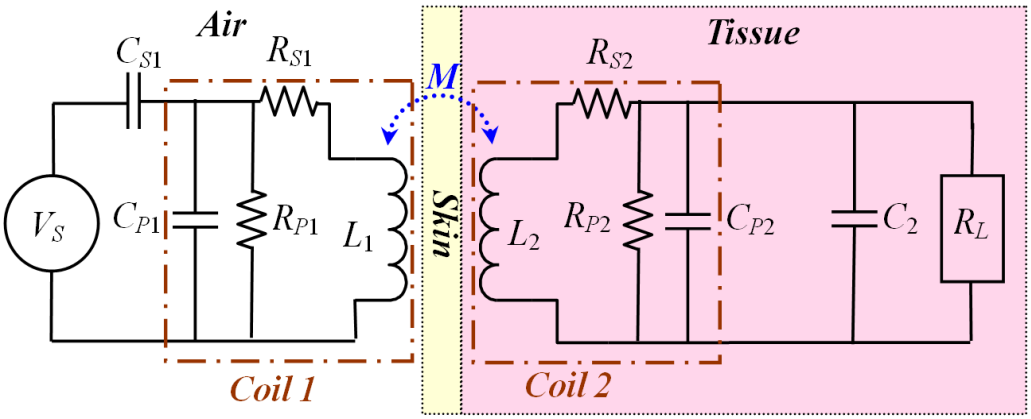

(b)

Figure 3.1: (a) Power flow diagram in a transcutaneous inductive power transmission. (b) The schematic diagram of the inductive link with lumped equivalent circuit components [5].

3.1 The Theoretical Modeling of Implanted Planar Spiral Coil

The need for small footprints in the next generation of high performance implantable devices calls for higher geometrical precision for integration on chip or on package. This would require microfabrication techniques that result in lithographically defined planar structures that are known as printed spiral coils (PSCs). PSCs offer more flexibility in defining their characteristics and have the ability to conform to the body curvature if fabricated on thin flexible substrates such as polyimide or parylene [14]. The lumped equivalent circuit model of each PSC in Figure 3.1 is enclosed in dash-dot boxes. In the following, a realistic theoretical model for PSCs is constructed to both implanted and external PSCs.

3.1.1 Inductance

In this work, all PSCs are square shaped with rounded corners that have a radius of about a tenth of the side length of the PSC (d_o/10) to eliminate sharp edges. Several closed-form equations have been proposed to approximate L in PSCs. (3.1) is adopted from [108] for square shaped PSCs,

$$L = \frac{1.27 \cdot \mu n^2 d_{avg}}{2}\left[\ln\left(\frac{2.07}{\varphi}\right) + 0.18\varphi + 0.13\varphi^2\right], \tag{3.1}$$

where n is the number of turns, $\mu = \mu_0 \mu_r$ is permeability, and $d_{avg} = (d_o + d_i)/2$, where d_o and d_i are the outer and inner side lengths of the coil, respectively. $\varphi = (d_o - d_i)/(d_o + d_i)$ is a parameter known as fill factor. From [108], different shapes of the PSCs are also studied. The accuracy of (3.1) has an indirect relationship with the s/w ratio, where w and s are the PSC metal line width and spacing, respectively. According to [108], the error in (3.1) is 8% for $s/w = 3$ and increases for $s/w > 3$. Moreover, the accuracy of (3.1) degrades with $\varphi \leq 0.1$ or $n \leq 2$.

3.1.2 Capacitance

Parasitic capacitance, C_P, is mainly determined by the spacing between planar conductive traces and their surrounding materials. Implantable PSCs are implemented on organic, ceramic, or silicon substrates and coated by an insulator such as parylene or silicone. When implanted, they are surrounded by tissue and fluids that have high permittivity, which significantly increase the parasitic capacitance of the PSCs compared to when they are operated in air. In order to model the unit length parasitic capacitance of an implanted PSC, the PSC is considered as a coplanar stripline sandwiched between several layers of dielectric substrates, as shown in Figure 3.2.

The effective relative dielectric constant, $\varepsilon_{r\text{-}eff}$, of the multilayer structure has to be estimated for the capacitive coupling between coplanar conductors. It should take into account the effect of all layers and their thicknesses as opposed to only one surrounding material. Conformal mapping is one of the spatial transformation schemes mainly used in calculation of static two-dimensional unbounded field problems. Using conformal mapping and superposition of partial capacitances, the analytical equations are derived in [109]–[111]. Figure 3.2 shows the cross section of two traces of the external PSC in multilayer environment. The planar metal traces are implemented on a substrate that provides mechanical support and coated on both sides by an insulator. One side of the PSC is air and the other side is the tissue or saline (in some of our measurements). The tissue is considered as a single homogeneous layer to simplify the calculation. In realistic situation, one should discriminate between the skin, fat, muscle, blood, and bone properties [27], [29]. From conformal mapping technique and superposition of individual layers, the total capacitance per unit length of the external PSC can be expressed as

$$C_{ext} = \varepsilon_{r-eff} C_0 = C_0 + C_{01} + C_{02} + C_{03} + C_{04} + C_{05}\,, \tag{3.2}$$

where C_0 is the capacitance between adjacent traces in free space, and C_{0i} (i = 1 to 5) is the additional partial capacitance of each planar dielectric layer in Figure 3.2. Theoretically,

$$C_0 = \varepsilon_0 \frac{K(k_0')}{K(k_0)},\ k_0 = \frac{s}{s+2w}, \text{ and } k_0' = \sqrt{1-k_0^2}\,, \tag{3.3}$$

where $K(k_0)$ is the complete elliptic integral of the first kind [109]. $\varepsilon_{r\text{-}eff}$ of coplanar metal PSC traces embedded in Figure 3.2 multilayer structure for package and tissue material can be found from,

$$\varepsilon_{r-eff} = 1 + \frac{1}{2}(\varepsilon_{r1} - 1)\frac{K(k_0)K(k'_1)}{K(k_0')K(k_1)} + \frac{1}{2}(\varepsilon_{r2} - \varepsilon_{r1})\frac{K(k_0)K(k'_2)}{K(k_0')K(k_2)} + \frac{1}{2}(\varepsilon_{r3} - 1)\frac{K(k_0)K(k'_3)}{K(k_0')K(k_3)}$$

$$+ \frac{1}{2}(\varepsilon_{r4} - \varepsilon_{r3})\frac{K(k_0)K(k'_4)}{K(k_0')K(k_4)} + \frac{1}{2}(\varepsilon_{r5} - \varepsilon_{r4})\frac{K(k_0)K(k'_5)}{K(k_0')K(k_5)} \tag{3.4}$$

$$k_i = \frac{\tanh(\pi s / 4t_i)}{\tanh(\pi(s+2w)/4t_i)},\ k_i' = \sqrt{1-k_i^2}\,,$$

ε_{ri} and t_i are the relative dielectric constant and thickness of dielectric layers in Figure 3.2, respectively [109]-[111].

Up until this point, the effect of the PCS metal thickness, t_0, is considered. A good way to include t_0, according to [111], is to adjust the PSC line width and spacing by 2Δ, where

$$\Delta = \frac{t_0}{2\pi\varepsilon_e}\left[1 + \ln\left(\frac{8\pi w}{t_0}\right)\right], \tag{3.5}$$

and ε_e is the mean value of the permittivities of the layers in contact with the strips, as shown in Figure 3.3.

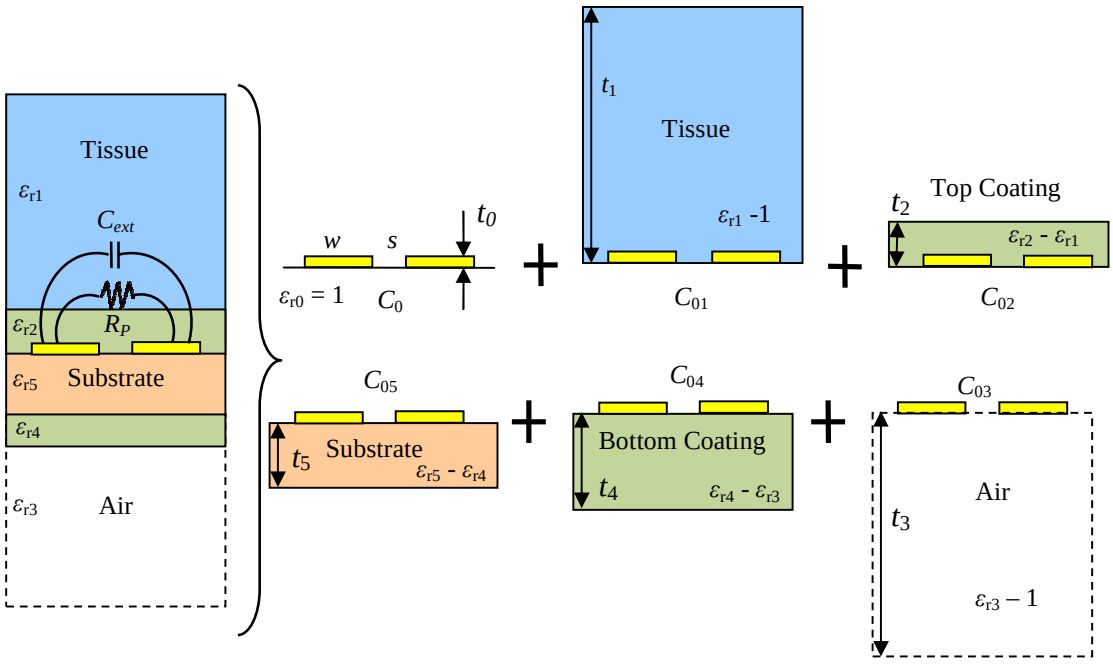

Figure 3.2: Modeling of the parasitic capacitance and parallel resistance created by the multilayer material of the external PSC by the coplanar stripline [111].

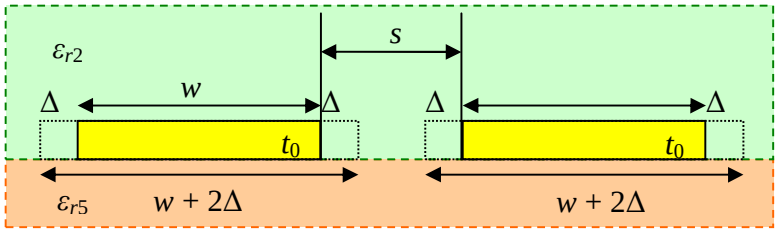

Figure 3.3: Modification of the PSC line width and spacing to account for the metal thickness, t_0 [111].

In order to access the PSC inner terminal, a conductor should bridge across all other turns of the PSC in a different layer and make a connection to the PSC metal layer through a via. This would result in additional parasitic capacitance between the two overlapping metal layers. The overlapping trace can be considered a microstrip line with the overlapping trace capacitance of

$$C_{ov} = \varepsilon_0 \varepsilon_{r\_eff\_ov} \frac{A_{ov}}{t_{ov}}, \tag{3.6}$$

where A_{ov} is the overlapping area and t_{ov} is the spacing between the two metal layers, which could be equal to t_5 in Figure 3.2 if the substrate has only two metal layers, one on each side. According to [112] , the effective dielectric constant between two conductive plates can be found from,

$$\varepsilon_{r\_eff\_ov} = \frac{\varepsilon_{r5}+1}{2} + \frac{\varepsilon_{r5}-1}{2}\left(1+\frac{12}{w/t_5}\right)^{-1/2} - \frac{\varepsilon_r - 1}{4.6}\frac{t_0/t_5}{\sqrt{w/t_5}}, \tag{3.7}$$

which includes the fringing effect and thickness of the conductive traces. Overall, the total parasitic capacitance of the external PSC can be calculated from,

$$C_P = C_{ext} \cdot l_c + C_{ov}, \tag{3.8}$$

where l_c is the PSC conductor length, found from [5],

$$l_c = 4 \cdot n \cdot d_o - 4 \cdot n \cdot w - (2n+1)^2 (s+w)\,. \tag{3.9}$$

For the implanted PSC, (3.2) to (3.9) can be used with the exception that the dielectric Layer-3 (air) should be replaced by the tissue properties, similar to Layer-1, depending on the anatomical location of the implanted device.

3.1.3 Series Resistance

The series resistance, R_S, is dominated by the DC resistance of the PSC conductive trace,

$$R_{DC} = \rho_c \frac{l_c}{w \cdot t_0}, \tag{3.10}$$

where ρ_c is the resistivity of the PSC conductive material, which is copper. The skin effect increases the AC resistance of the PSC at high frequencies

$$R_{skin} = R_{DC} \cdot \frac{t_0}{\delta \cdot (1 - e^{-t_0/\delta})} \cdot \frac{1}{1 + t_0 / w}, \tag{3.11}$$

$$\delta = \sqrt{\frac{\rho_c}{\pi \cdot \mu \cdot f}},\ \mu = \mu_r \cdot \mu_0 \tag{3.12}$$

where δ is the skin depth, μ_0 is the permeability of space, and μ_r is the relative permeability of the metal layer [113].

Another effect that contributes to the PSC parasitic resistance is the current crowding caused by the eddy currents, illustrated in Figure 3.4. When the magnetic fields of the external PSC or adjacent turns in the same PSC penetrate a planar trace normal to its surface, eddy currents are generated within that trace in a direction that opposes the changes in the magnetic field according to Lenz's law. For example, in Figure 3.4, the direction of the eddy currents corresponds to an increasing magnetic field. These currents add to the current passing through the inner side of the PSC trace, nearest to the center of the spiral, and subtract from the current passing through the outer side. This constriction in the current increases the effective resistance compared to a uniform flow throughout the trace width. The modified resistance by including the effect of eddy currents can be expressed as,

$$R_{eddy} = \frac{1}{10} R_{DC} \left(\frac{\omega}{\omega_{crit}} \right)^2, \tag{3.13}$$

$$\omega_{crit} = \frac{3.1}{\mu_0} \frac{s+w}{w^2} R_{sheet}, \tag{3.14}$$

where ω_{crit} is the frequency at which the current crowding begins to become significant and R_{sheet} is the metal trace sheet resistance [114]. Therefore, R_S at the power carrier frequency can be defined as R_{DC} when it is modified by the skin and eddy current effects [115]. The total series resistance with the parasitic effects, skin effect and eddy current, is shown as

$$R_S = R_{skin} + R_{eddy} = R_{DC}\left(\frac{t_0}{\delta\cdot(1-e^{-t_0/\delta})}\cdot\frac{1}{1+t_0/w}+\frac{1}{10}\left(\frac{\omega}{\omega_{crit}}\right)^2\right) \tag{3.15}$$

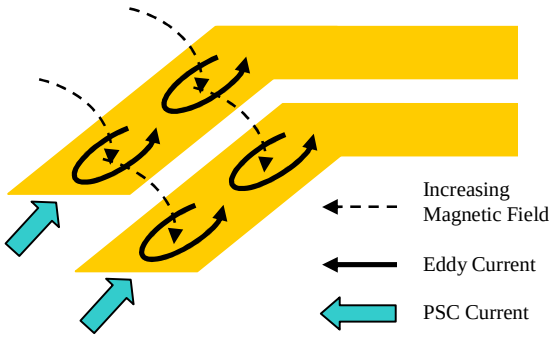

Figure 3.4: Demonstration of the current crowding effect [114].

3.1.4 Parallel Resistance

At low RF frequencies, the parallel resistance, R_P, in the PSC model of Figure 3.1 is resulted mainly from the dielectric loss and can reduce the PSC quality factor. Most dielectric materials used in the PSC substrate and coating have small dielectric loss, resulting in very large R_P. In comparison, the tissue is significantly more conductive and its effect should be considered in a multilayer material environment. The partial conductance technique combined with the conformal mapping is used to calculate the dielectric loss of the tissue. Dielectric losses can be described by the loss tangent, $tan(\delta)$, which is related to its conductivity, $\sigma = \varepsilon_0\varepsilon_r\omega tan(\delta)$. The conformal transformations required for the evaluation of partial conductivities due to different layers are similar to the partial capacitances described in Section 3.1.2 [111]. For the external coil, shown in Figure 3.2, the equivalent conductance of the PSC unit length is going to be

$$\frac{1}{R_P} = G_P = \frac{\omega\varepsilon_0}{2}\left[\varepsilon_{r1}\tan\delta_1\frac{K(k_1')}{K(k_1)}+(\varepsilon_{r2}\tan\delta_2-\varepsilon_{r1}\tan\delta_1)\frac{K(k_2')}{K(k_2)}+\varepsilon_{r3}\tan\delta_3\frac{K(k_3')}{K(k_3)}\right.$$

$$\left.+(\varepsilon_{r4}\tan\delta_4-\varepsilon_{r3}\tan\delta_3)\frac{K(k_4')}{K(k_4)}+(\varepsilon_{r5}\tan\delta_5-\varepsilon_{r4}\tan\delta_4)\frac{K(k_5')}{K(k_5)}\right], \tag{3.16}$$

where $tan(\delta_3) = 0$ for air. The same equation can be used for the internal coil equivalent conductance.

3.1.5 PSC Quality Factor

From (3.1)-(3.16), all the parameters needed for calculating the overall impedance and *Q* of the implanted and external PSCs can be derived,

$$Z = \frac{R_S + j\omega L}{(R_S + j\omega L)(G_P + j\omega C) + 1}, \tag{3.17}$$

$$Q = \frac{\mathrm{Im}(Z)}{\mathrm{Re}(Z)}. \tag{3.18}$$

From these equations, the higher parasitic capacitance decreases the PSC quality factor, and consequently the power efficiency.

3.1.6 Mutual Inductance and Power Transfer Efficiency (PTE)

A PSC can be considered a set of concentric single-turn loops with shrinking diameters, all connected in series. The mutual inductance, *M*, of a pair of PSCs, can be found by summing the partial values between every turn on one PSC and all the turns on the other PSC at a certain coupling distance, *D*, [5], [62], [115]. From *M*, the PSCs' coupling coefficient, *k*, would be

$$k = M \Big/ \sqrt{L_1 L_2}\,. \tag{3.19}$$

A PSC can be considered a set of concentric single-turn coils with shrinking diameters, connected in series. Therefore, once the mutual inductance between a pair of single-turn coils in parallel planes is found, the overall *M* can be found by summing the partial mutual inductance values between every turn on one coil and all the turns on the other coil. Using Maxwell equations, M_{ij} between a pair of parallel circular single-turn coils at radii r_i and r_j can be found from

$$M_{ij} = \mu\pi\sqrt{r_i \cdot r_j}\int_0^{\infty} J_1\left(x\sqrt{\frac{r_i}{r_j}}\right)J_1\left(x\sqrt{\frac{r_j}{r_i}}\right)J_o\left(x\frac{\gamma}{\sqrt{r_i \cdot r_j}}\right)\cdot\exp\left(-x\frac{D}{\sqrt{r_i \cdot r_j}}\right)dx \qquad (3.20)$$

where D is the relative distance between the two coils and γ is the lateral misalignment [63], [112]. J_0 and J_1 are the Bessel functions of the zeroth and first order, respectively. For perfectly aligned coaxial coils, where $\gamma = 0$, (10) can be simplified to

$$M_{ij} = \frac{2\mu}{\alpha}\sqrt{r_i \cdot r_j}\left[\left(1-\frac{\alpha^2}{2}\right)K(\alpha)-E(\alpha)\right] \qquad (3.21)$$

$$\alpha = 2\sqrt{\frac{r_i \cdot r_j}{(r_i+r_j)^2 + D^2}} \qquad (3.22)$$

where $K(\alpha)$ and $E(\alpha)$ are the complete elliptic integrals of the first and second kind, respectively [63]. By adding the partial mutual inductances between every two turns on a PSC pair,

$$M = g\sum_{i=1}^{n_1}\sum_{j=1}^{n_2} M_{ij}(r_i, r_j, D) \qquad (3.23)$$

where g, geometrical coefficient, is a factor dependent on the shape of the PSC. Even though the area of a square shaped coil with a side length of $2r$ is 27% larger than a circular coil with equal diameter, it is empirically found that M between a pair of square shaped PSCs is only 10% higher than a pair of similar circular PSCs. From the empirical results, g = 0.95, 1.0, and 1.1 for a pair of hexagonal, circular, and square shaped PSCs, respectively [7].

It can be shown mathematically that the highest voltage gain and efficiency across an inductive link can be achieved when both LC-tanks are tuned at the power carrier frequency,

$$\omega = \omega_0 = 1/\sqrt{L_1 C_{S1}} = 1/\sqrt{L_2 (C_2 + C_{P2})} \tag{3.24}$$

In practice, the secondary PSC is often loaded by the implant electronics, R_L, as shown in Figure 3.1. The loaded secondary quality factor at resonance can be found from [36],

$$Q_L = \left(\frac{R_{S2}}{\omega L_2} + \frac{\omega L_2}{R_L \parallel R_{P2}} \right)^{-1}. \tag{3.25}$$

The inductive link power transfer efficiency (PTE) can then be calculated from PSCs' k and Q [5],

$$\eta_{12} = \frac{k^2 Q_1 Q_L}{1 + k^2 Q_1 Q_L} \cdot \frac{Q_L}{Q_2 + Q_L}. \tag{3.26}$$

It should be noted that most aforementioned parameters in PSCs are interrelated. For example, increasing n in PSCs without changing d_o can increase their L and k. However, it may also decrease Q by increasing R_S due to increased l and reduced w. Therefore, there are optimal PSC geometries that would maximize η_{12} [5]. Another important parameter is the V_S output resistance, not shown Figure 3.1, which is out of the scope of this paper and needs be considered along with the driver's efficiency [116].

3.2 Optimization of Printed Spiral Coils

In this section, the detailed models built in Section 3.1 are used to design three sets of coils optimized for air, saline, and muscle tissue environments. The material properties of these volume conductors are summarized in Table 3.1 [27], [29]. The iterative design procedure [5] is adopted. The procedure starts with a set of design constraints and initial conditions imposed by the PSC application and fabrication process and ends with the optimal geometries of the PSC pair for maximum η_{12}.

Table 3.1. MATERIAL PROPERTIES

Material	Air	Saline	Muscle	FR4	Silicone
f [MHz]	13.56	13.56	13.56	13.56	13.56
σ [S/m]	0	0.60	0.58	1.33e-4	2.26e-6
ε_r	1	78	136	4.4	3.0
$tan(\delta)$	0	10.2	6.0	0.04	0.001

*Derived from [27] and [29].

3.2.1 Optimization Procedure for Power Transfer Efficiency (PTE)

An iterative design procedure has been depicted in this section which starts with a set of design constraints and initial values, and ends with the optimal PSC pair geometries. The first step is applying design constraints, and initial values are put in the equations for second step. The third step optimizes the size and fill factor, φ_1, of primary PSC, and the fourth step optimizes fill factor, φ_2, and line width, w_2, of secondary PSC. Then, the design goes back to optimize size and line width, w_1, of primary coil. From these steps, if the efficiency is not improved more than 0.1%, the iteration goes back to the third step. The flow chart of this procedure is summarized in Figure 3.5. After calculation, HFSS simulations have been used for fine tuning and verifying the values suggested by theoretical calculations. Thus, the simulation results can give the designer a good sense of how to make necessary compromises to achieve a satisfactory performance for the PSCs.

In this design example, the size of the implant is 10×10 mm^2, which is reasonable for a retinal or cortical visual prosthesis [25], [71]. The nominal coupling distance between the PSCs is considered D = 10 mm and the power carrier is set at 13.56 MHz to comply with RFID standards [36]. However, it could be set to any other band in 0.1~50 MHz range, as long as it is well below the half of the PSCs' self resonance frequency (SRF) [69], [2].

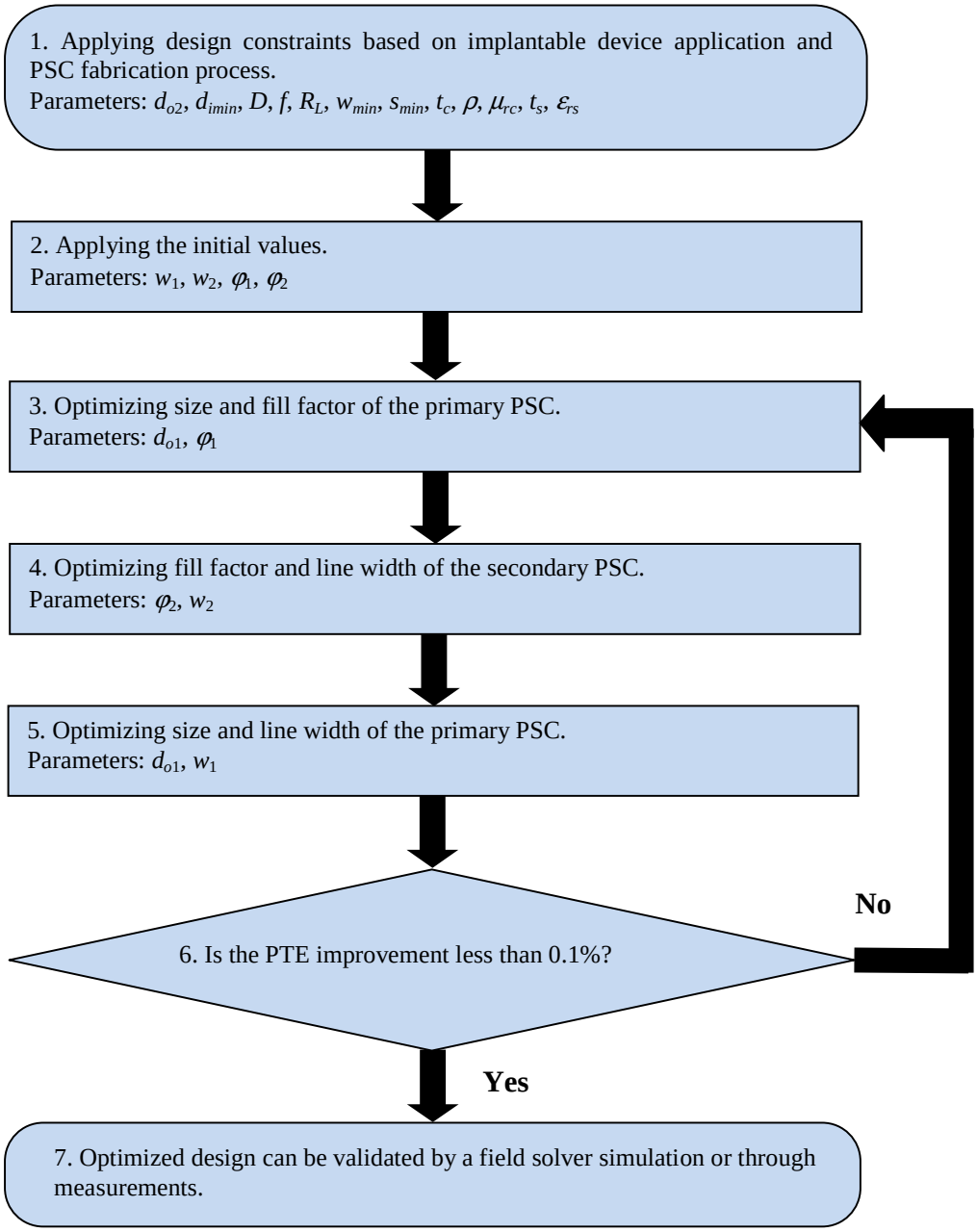

Figure 3.5: Iterative PSC design flowchart for optimal PTE.

Table 3.2 shows the geometries of the resulting PSCs, specifically optimized for each environment along with the simulation results for Q, k, and η_{12}, when the PSC pair is perfectly aligned. It should be noted that k is the highest in Set-1, resulting in

maximum efficiency in the air. However, Q of Set-1 and Set-2 are both smaller than Q of Set-3 in the muscle environment, which results in Set-3 showing the highest efficiency in muscle. Further, it can be seen that for the same implant size and coupling distance, the outer diameter (side length) of the external PSC, shrinks with increasing dielectric constant and loss tangent.

Table 3.2. OPTIMIZED PSC GEOMETRIES AND INDUCTIVE LINK CHARACTERISTICS FROM SIMULATION RESULTS*

Parameter	**Set-1**		**Set-2**		**Set-3**	
Material	**Air**		**Saline**		**Muscle**	
Name	PSC11	PSC12	PSC21	PSC22	PSC31	PSC32
d_o (mm)	38	10	30	10	24	10
d_i (mm)	14.9	5.8	11.1	5.5	9.4	7.2
φ	0.44	0.27	0.46	0.29	0.46	0.16
n (turns)	7	6	3	5	2	4
w (μm)	1500	200	3000	250	3500	150
s (μm)	150	150	150	150	150	150
L (μH)	1.66	0.51	0.26	0.33	0.12	0.34
R_S (Ω)	0.93	0.72	0.22	0.44	0.06	0.72
R_P (kΩ)	758	3120	7.19	18.34	2.36	1.68
C_P (pF)	3.12	0.18	7.88	1.37	7.72	0.77
C_{s1} / C_2 (pF)	83.0	270.1	510.2	417.5	1148	450
SRF (MHz)	70	525	122	236	165	302
Q	128	60	81	55	96	32
k	0.0697		0.0518		0.0301	
η_{12_cal} (%)♦	72.05		55.22		29.85	
η_{12_sim} (%)	74.86		49.12		27.70	
η_{12_meas} (%)♠	72.22		51.80		30.84	

*For perfectly aligned PSCs with a nominal coupling distance of D = 10 mm at f = 13.56 MHz and R_L = 500 Ω, coated with a 300 μm layer of silicone.
♦Calculation results.
♠Measurement results.

3.2.2 Optimal Coating Thickness

The receiver coil in inductively powered IMDs is often embedded in ceramic, parylene, or medical grade silicone [117]. The dielectric constant, ε_r, of silicone coating is much lower than saline or any type of human tissue, as shown in Table 3.1. Increasing the thickness of the coating will reduce C_P and increase R_P in the PSC model, both of which help increasing Q and consequently η_{12}. On the other hand, increasing the

thickness of the coating will increase *D* and the volume of the implantable device, both of which are undesired. Therefore, it is instructive to indicate the optimal coating thickness by sweeping t_2 in PSC model (Figure 3.2), while maintaining all other parameters constant. In these model-based simulations, all PSCs were in the muscle environment and maintained 10 mm between the outer surfaces of the two PSCs' coating. The actual coupling distance between the two PSCs was $D = 2t_2 + 10$ mm.

Figure 3.6 shows the results of varying the coating thickness of PSCs in Table 3.2. It can be seen from the model that the optimal thickness for Set-3, which geometries are optimized for the muscle environment, is a reasonable value of t_2 = ~300 μm. However, the other PSCs need much thicker coatings to reach their maximum efficiencies. This is because their geometries are optimized for lower loss environments and they need thicker coatings to compensate for the additional loss in the muscle environment or any other tissue environments.

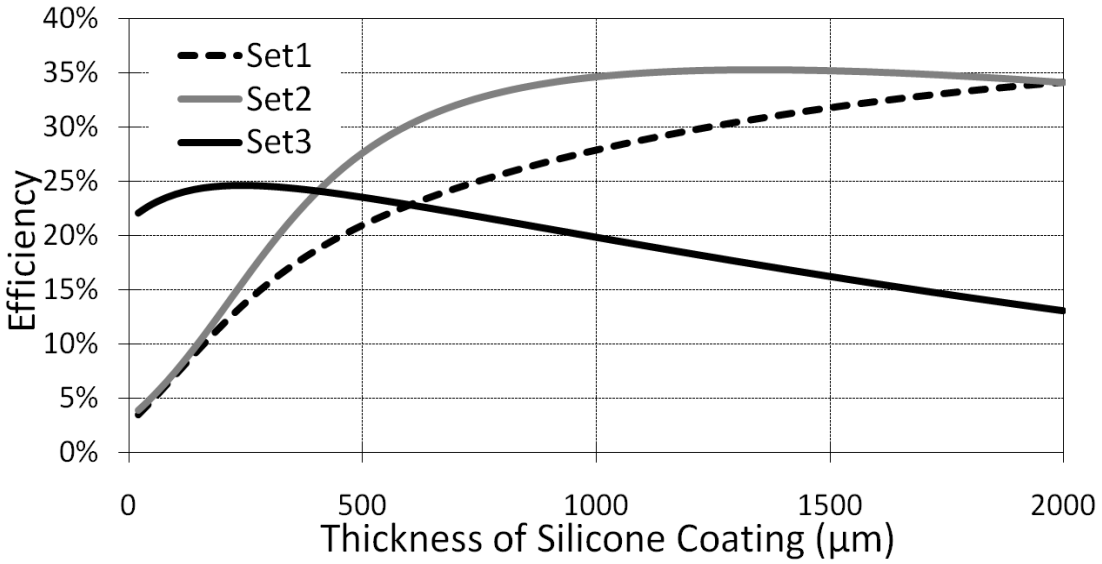

Figure 3.6: Optimal thickness of the silicone coating on both sides of each PSC with geometries given in Table 3.2 in the muscle environment. The distance between the coating surfaces that face each other is fixed at 10 mm.

3.3 Simulation and Measurement Results

Figure 3.7 shows the PSC measurement setup. A network analyzer (R&S ZVB4) is used to measure the S-parameters of each coupled PSC pair at a desired coupling distance. The S-parameters were converted to Z-parameters to calculate k and the quality factors from (3.17)-(3.21) to find η_{12} [118]. In addition to measurements in air, two plastic bags (~50 μm thickness), filled with saline or beef are used to emulate implant environments. The internal PSC was sandwiched between the two bags while the external PSC was aligned with it. The thickness of the layer between PCSs was t_1 = 10 mm, and the layers behind the internal PSCs, t_3, were 70 mm and 50 mm for saline and beef, respectively. The saline was a solution of 9 mg/L NaCl, and the beef was sirloin steak. The beef temperature at the time of measurement was 10.8 °C, and the saline was in equilibrium with the room temperature at 24.0 °C.

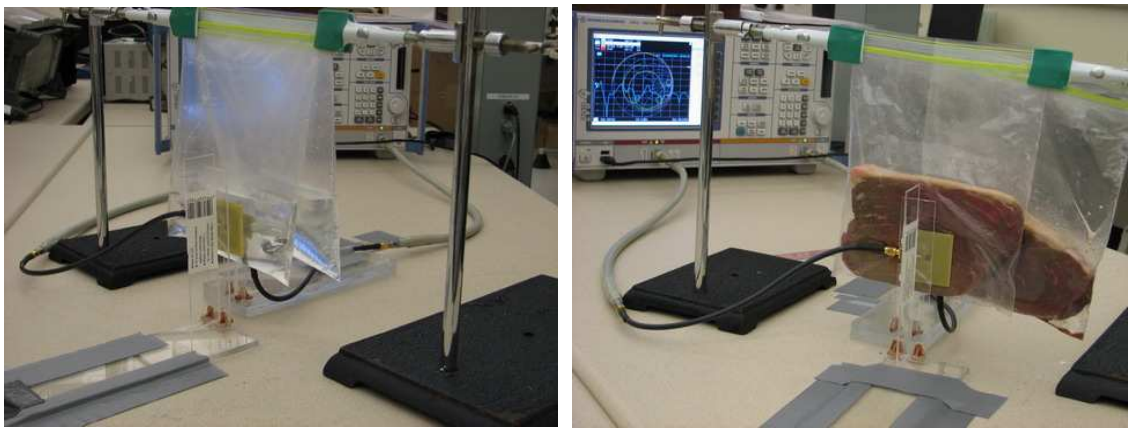

(a) **(b)**

Figure 3.7: Experimental setup for measuring inductive link properties between a pair of PSCs in the air, saline (a) and muscle (b) environments.

3.3.1 PSC Quality Factor

Each PSC pair in Table 3.2 is coated with CF16-2186 silicone elastomer from NuSil (Carpinteria, CA) up to a thickness of ~300 μm, which is optimized from Section 3.2.2. Figure 3.8 compares the theoretical calculation, HFSS simulation, and

measurement results of PSC21 and PSC31 (both external) quality factors vs. carrier frequency, with and without coating, in saline and muscle environments. It can be seen that *Q* of both PSCs have been improved with the silicone coating as predicted. This improvement is more significant for PSC31, which is coated close to its optimal coating thickness.

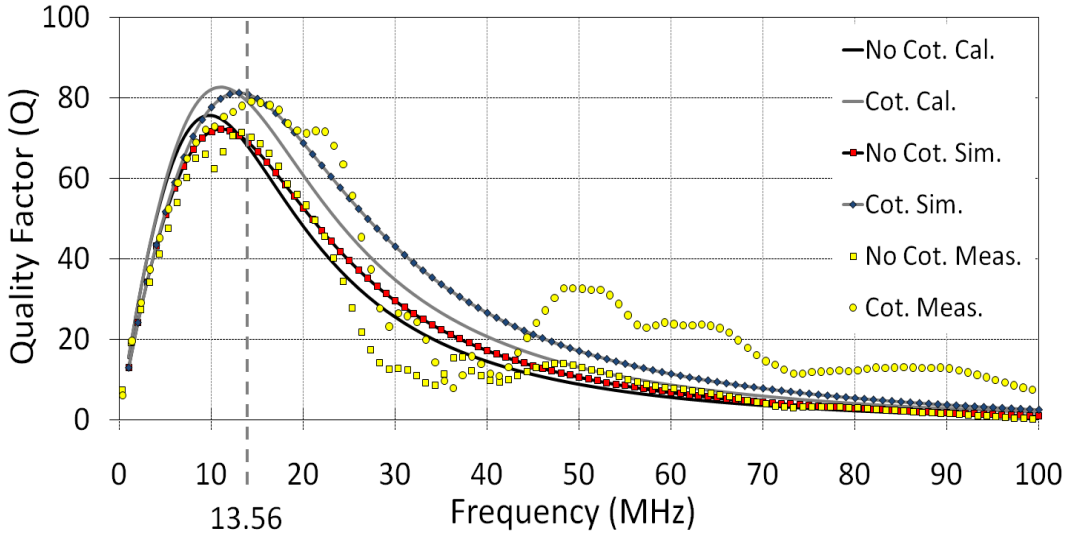

(a)

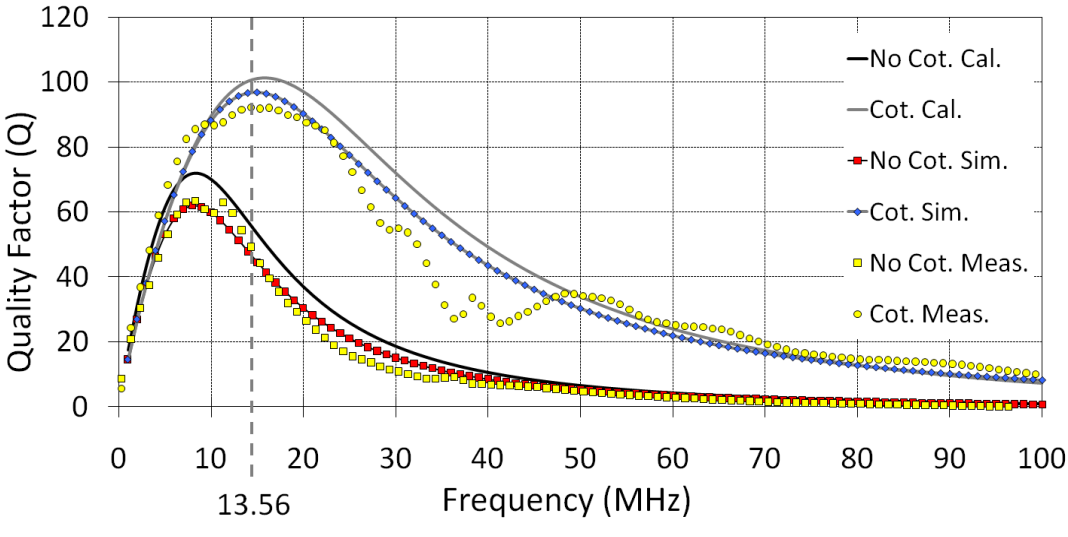

(b)

Figure 3.8: Comparison between theoretical calculations, HFSS simulations, and measurement results of *Q* variations vs. carrier frequency of (a) PSC21 in saline and (b) PSC31 in muscle, with and without 300 μm silicone coating.

Figure 3.9 shows how the Q of coated PSC11 and PSC31 change *vs.* frequency in the air and muscle environments. At 13.56 MHz, Q of PSC11 decreases by 78% from 128 in air to 28 in the muscle environment. On the other hand, the Q of PSC31 decreases only by 25% from 122 in air to 92 in muscle. The agreement among calculation, simulation, and measurement results in Figure 3.9 demonstrate the efficacy of the geometrical optimization has helped to improve the PSC quality factors by a factor of ~3.3 in the muscle environment. In fact, optimization of the implanted PSC for the surrounding environment is influenced by the changes in the geometry of the external PSC. A comparison between PSC12 and PSC32 in Table 3.2 shows that optimization for the muscle environment has reduced n_{32} and w_{32}, both of which reduce C_{P2} and R_{P2}. In measurements, Q of PSC12 and PSC32 reduced from 51.5 and 36.6 in the air to 42.3 and 36 in the muscle environment, respectively. This is because of the size constraint applied to the implanted PSC (10×10 mm^2). Therefore, the resulting the PTE in muscle for Set-3 is higher than Set-1, as discussed in Section 3.3.2.

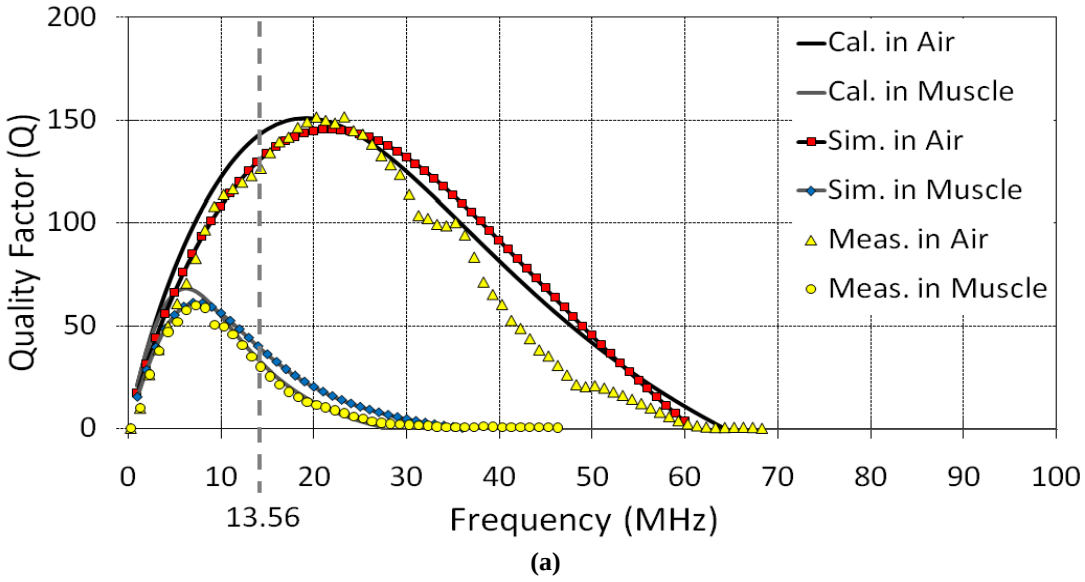

(a)

Figure 3.9: Comparison between theoretical calculations, HFSS simulations, and measurement results of Q variations vs. carrier frequency in (a) PSC11 that is optimized for air. (b) PSC31 that is optimized for muscle, in these two environments (see Table 3.2 for PSC geometries).

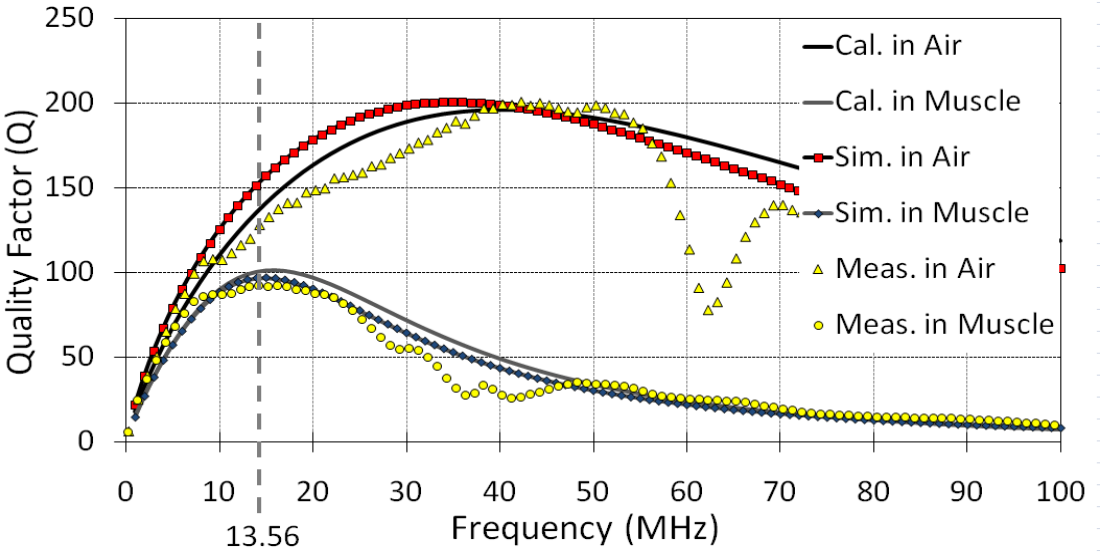

(b)

Figure 3.9: Comparison between theoretical calculations, HFSS simulations, and measurement results of *Q* variations vs. carrier frequency in (b) PSC31 that is optimized for muscle, in these two environments (see Table 3.2 for PSC geometries).

3.3.2 Power Transfer Efficiency (PTE)

PSC pair geometries affect *k* and *Q*, both of which are key factors in η_{12} according to (3.22). The comparison of the PTE of the three sets of PSCs is shown in Table 3.2 in the air, saline, and muscle environments, in Figs. 3.10a, 3.10b, and 3.10c, respectively, through model-based theoretical calculations, FEA simulations, and experimental measurements. The carrier frequency is held constant at 13.56 MHz, and the secondary PSC is loaded with R_L = 500 Ω. Figure 3.10 curves show that each set of PSCs performs best in its designated operating environment, most important of which is the muscle, where an implantable device eventually resides. Figure 3.10c obviously shows that a pair of PSCs that is optimized for air (Set-1) provides the worst η_{12} when implanted in the muscular tissue. Set-1 PSC pair can achieve more than 70% of the PTE in the air due to their high *k*, but their η_{12} drops to only 21.8% in the muscle environment due to

degradation in their Q, as seen in Figure 3.9a. Set-3 pair, on the other hand, provides η_{12} > 30% at D = 10 mm due to PSC31 smaller geometries.

Figure 3.10 curves also show reasonable agreement among theoretical calculations from our models, finite element simulations, and measurement results. There are, however, small discrepancies due to the following reasons, some of which are related to our models and some are related to the measurement setup: (1) inherent limitations in the accuracy of the closed form equations, particularly when the PSC parameters are close to or out of their valid range of parameters, (2) large line width and small number of turns, resulted from our optimization algorithm particularly for Set-3 (Table 3.2), causing the shape of PSC13 to deviate from a perfect square with rounded corners, affecting the validity of (1), (3) secondary effects such fringing and capacitive coupling between the two inductively coupled PSCs, which were not included in our models, (4) manually applied silicone coating was not quite uniformly distributed on the PSC surfaces, (5) there could be small patches of air gap between the plastic bags containing the volume conductors and the outer surface of the PSCs' silicone coating, and (6) the 50 μm thick plastic bag, made of polyethylene with ε_r = 2.3 and $tan(\delta)$ = 0.0002, which was considered to be part of the PSC silicone coating.

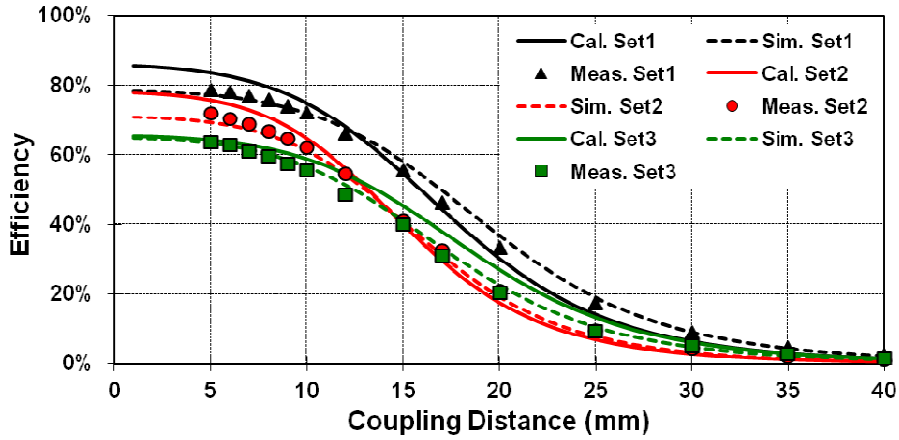

(a)

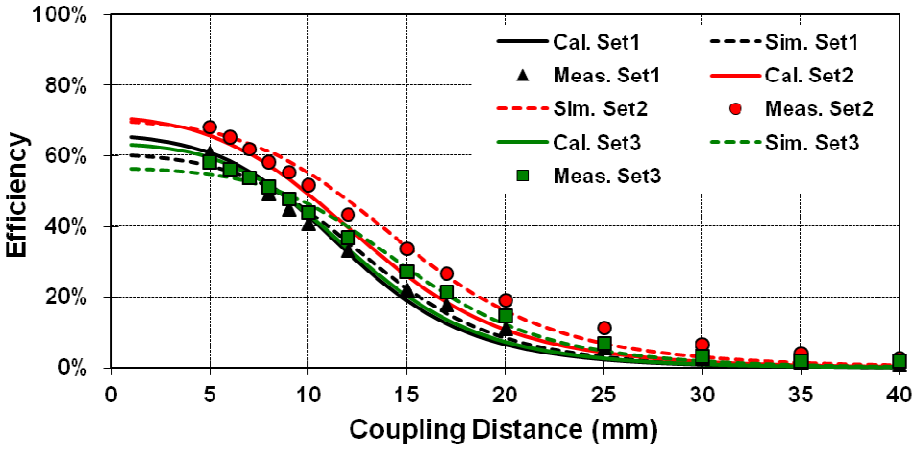

(b)

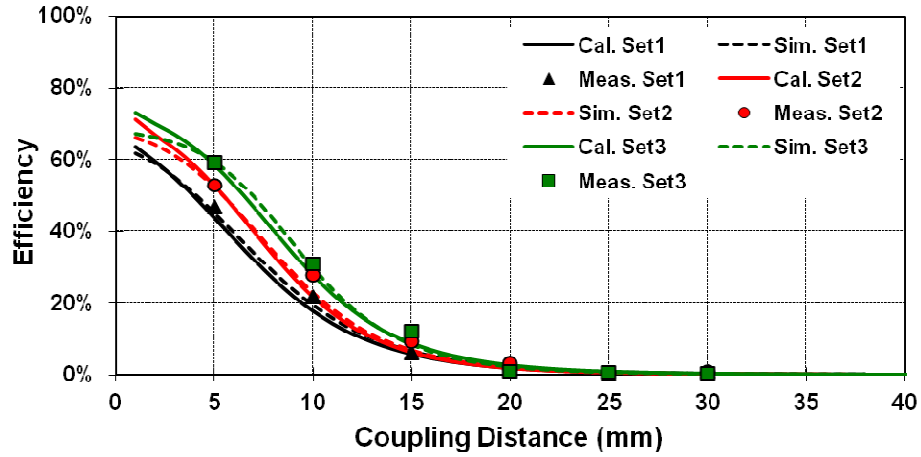

(c)

Figure 3.10: Variations of the power transfer efficiency with coupling distance at 13.56 MHz for three sets of PSCs in Table 3.2 optimized for (a) air, (b) saline, and (c) muscle environments.

3.4 Conclusions

This chapter demonstrates detailed models and devised design paradigms for small PSCs that are meant to be fabricated on rigid or flexible planar substrates, coated with biocompatible dielectric materials. Various phenomena that could result in degradation of the PSC quality factors due to coating and implantation were considered in our models. The models are combined with an iterative PSC design procedure, previously reported in [16], to optimize the PSC geometries for providing maximum PTE in tissue environments. This can result in lower heat dissipation, extended battery lifetime, and improved safety in neuroprosthetic devices, such as retinal or cortical implants, with demanding size constraints [58]. The design methodology is applied to optimize the wireless link of a 1 cm^2 implantable device example, operating at 13.56 MHz. Measurement results showed that optimized PSC pairs, coated with 0.3 mm of silicone, achieved 72.2%, 51.8%, and 30.8% efficiencies at a face to face relative distance of 10 mm, in air, saline, and muscle, respectively. The PSC which was optimized for air could only bear 40.8% and 21.8% efficiencies in saline and muscle, respectively, showing that considering the PSC surrounding environment in the design process can result in more than 10% improvement in the power transfer efficiency.

In this chapter, the PSC design maximizes the power carrier's PTE. On the other hand, wireless data communication is also important for implantable devices, and these two commutation links can interfere with each other. In the next chapter, this issue is addressed and the new coil and antenna design is introduced for both power and data links.

CHAPTER IV

MULTIBAND WIRELESS LINK FOR NEUROPROSTHETIC IMPLANTABLE DEVICES

Wireless operation of implantable microelectronic devices (IMD) is necessary in clinical neuroprostheses to reduce the risk of infection and patient discomfort, which may result from transcutaneous wires breaching the skin. The wireless link is expected to perform three major functions:

(1) *Power transmission*: The geometry of the coils used in the next generation of low-power IMDs is more likely to be planar and lithographically defined [74]. Therefore, an iterative design methodology to maximize their power transmission efficiency (PTE) for printed spiral coils (PSC) is discussed in Chapter 3 [4], [5].

(2) *Forward data transmission*: Wideband wireless data transmission from outside into the body is needed, such as the large volumes of stimulation data [119]. A separate pair of coils for the data transmission has utilized [9] because of conflicting requirements between power and data links. In this chapter, two types of data coils are studied. First, a pair of vertical coils wound across the diameter of the power PSCs whose symmetry and orthogonal magnetic field orientation would minimize the power carrier interference. Second, a pair of planar figure-8 coils, in which the electromotive force (EMF) induced from the power carrier in one loop, opposes the same in the other loop [10]. Hence, the total EMF interference from the power carrier can be very small when the two coils are perfectly aligned.

(3) *Back telemetry*: The IMDs require a wideband back telemetry link, but passive back telemetry, used in radio frequency identification (RFID) does not provide enough bandwidth for this application [36]. Therefore, the impulse-radio ultra-wideband (IR-UWB) is chosen for this purpose, which provides wide bandwidth with a simple and low-power transmitter [88]. A pair of miniature planar spiral UWB antennas was trying to put on the multiband wireless link, but the interference from the coil is still high [3]. Hence, a commercial miniature UWB antenna is for IMDs.

The detailed block diagram of the proposed multiband wireless link is proposed which is similar to Figure 1.1. L_1 is the external power PSC and, L_2 is the internal PSC that is implanted under the skin flap. L_3 and L_4 are the forward data coils. Back telemetry link utilizes miniature UWB antennas, A1 and A2.

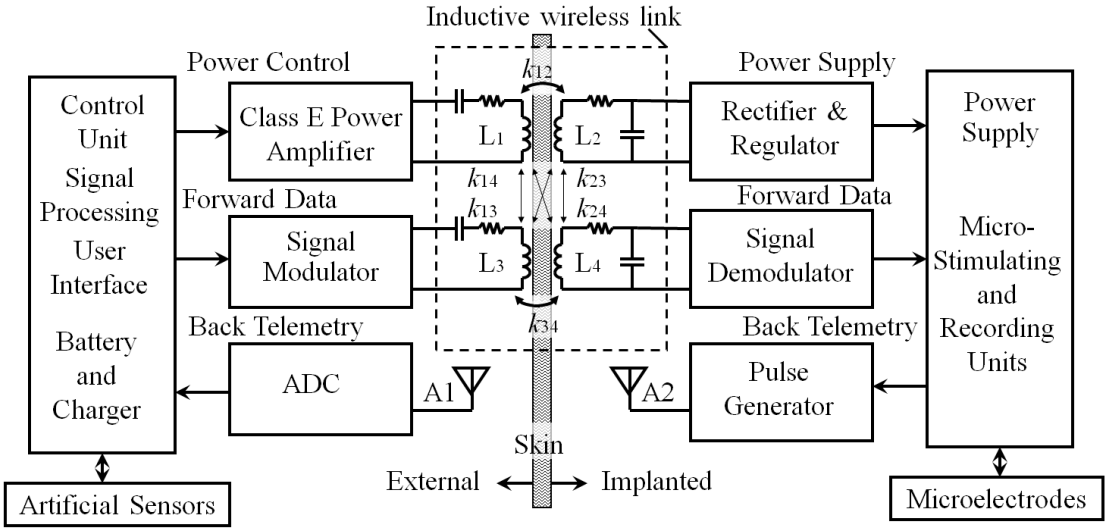

Figure 4.1: Block diagram of the multiband wireless link in a high-performance IMD [9].

The power PSCs design theory won't be discussed here since it has been covered in Chapter 3. In this chapter, a theoretical foundation for data coils is introduced in Section 4.1. Design procedure and optimization of the multiband wireless link

components is discussed in Section 4.2. Section 4.3 is dedicated to simulation and measurement results, followed by concluding remarks.

4.1 Forward Link

A separate pair of coils for the data transmission has utilized to reduce the interference from power carrier, and two types of the data coils, vertical coil and figure-8 coil, are studied in this section.

4.1.1 Vertical Data Coils

The geometry and orientation of the forward data coils are key issues, since the power carrier amplitude can be up to two orders of magnitude larger than the data carrier. In order to solve this problem, orthogonal coils by winding the data coils across the diameter of the power PSCs is proposed, as shown in Figure 4.2 [3]. In this method, due to symmetry and orthogonality of the coils' geometries, the magnetic flux generated by the power PSCs do not pass through data coils and their undesired cross coupling factors (k_{14}, k_{13}, k_{23}, and k_{24}) can theoretically be close to zero when the coils are perfectly aligned. The data coils, however, can maintain a small but adequate direct coupling, k_{34}, due to being in parallel with long conductors. One should note that k_{34} is maintained in the same range or slightly higher than the undesired couplings. Since the forward data link operates at a different frequency band, the receiver L_4C_{P4} tank helps with amplifying the received data carrier and filtering out the undesired power carrier interference [9].

In Figure 4.2, the height (h_d), width (w_d), and length (l_d) of each rectangular vertical data coil are depend on the thickness of the power PSC substrate, data coil's number of turns (n_d), and diameter of the power PSC, respectively. w_d also depends on the diameter of the chosen wire (Dia_d) and their spacing, s_d. Using these geometrical parameters in

tabular self inductance formulation in [3], the inductance of L_3 and L_4 are calculated. The detailed equations is presented in Appendix A.

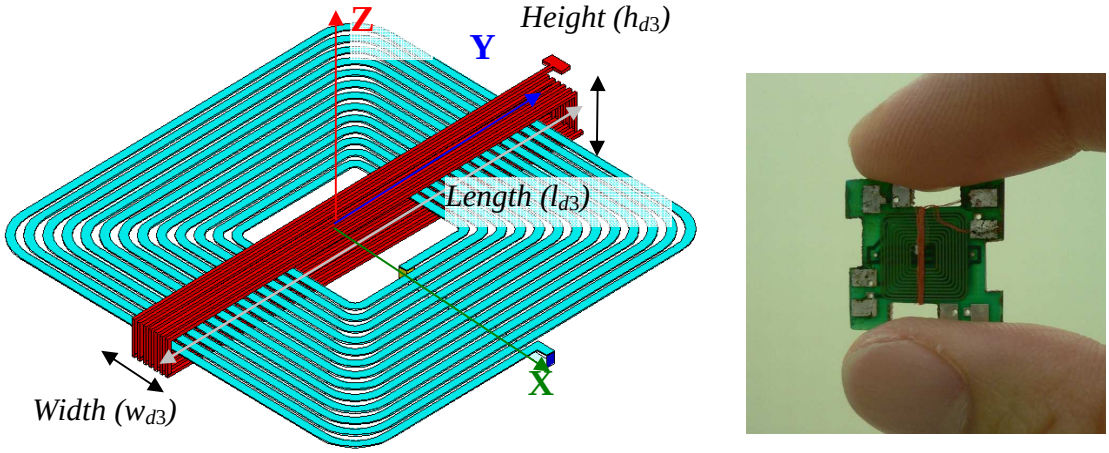

(a) **(b)**

Figure 4.2: (a) Rendering of the power and forward data transmission coils, showing their important geometrical parameters. (b) Receiver data and power coils fabricated on a 4 layer FR4 PCB [3].

The coupling coefficient between a pair of coil is defined as

$$k_{34} = M_{34} \Big/ \sqrt{L_3 L_4}\ , \tag{4.1}$$

where M_{34} is the mutual inductance between L_3 and L_4. Figure 4.3 shows the cross section of the rectangular solenoid-shaped coils. Regarding the M_{34} equations, the coils relative distance, D, and X-axis misalignment, X, are considered. The vertical data coils are robust against misalignments along the Y-axis (see Figure 4.2), and sensitive to misalignments along the X-axis. The original equations for the mutual inductance from [121] were based on circular solenoids. The height of rectangular coil (h_d) is used instead of the diameter for the circular solenoid. The area of the circular solenoid is also replaced by the area of the rectangular solenoid ($l_d \times h_d$). The simulation and measurement results showed that these approximations are valid for $l_d / h_d < 20$. Detailed equations for M_{34} are included in the Appendix A.

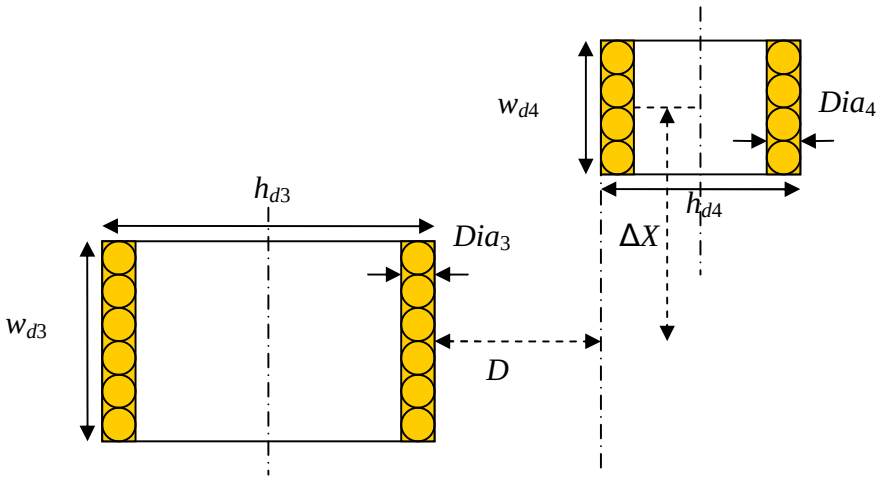

Figure 4.3: Cross section view of solenoid inductor coupling [121].

4.1.2 Figure-8 Data Coils

The second design for the data coils is based on the planar figure-8 geometry, shown in Figure 4.4a. This type of coil is often used in transcranial magnetic stimulation (TMS) [122]. The direction of windings in each loop of the coil is chosen such that when the coil is exposed to an external field symmetrical to both loops, induced currents would cancel out [123]. Therefore, even when they are in the same plane as the power PSCs, figure-8 coils can attenuate the power interference. Moreover, the mutual inductance, *M*, between two figure-8 data coils is larger than the coupling between vertical coils because these coils are facing each other. In this design, two out of four metal layers in the printed circuit board (PCB) are used to implant the figure-8 data coils with $N_{d3} = N_{d4} = 2$. L_4 is made as large as the IMD size allowed, *i.e.* filling the same area as L_2. Geometry, line width, and substrate thickness affect the self inductance and mutual coupling of the figure-8 coils. Since closed form equations for figure-8 coils are quite complicated, a commercial field solver, HFSS (Ansoft, Pittsburgh, PA) is used, to model these parameters.

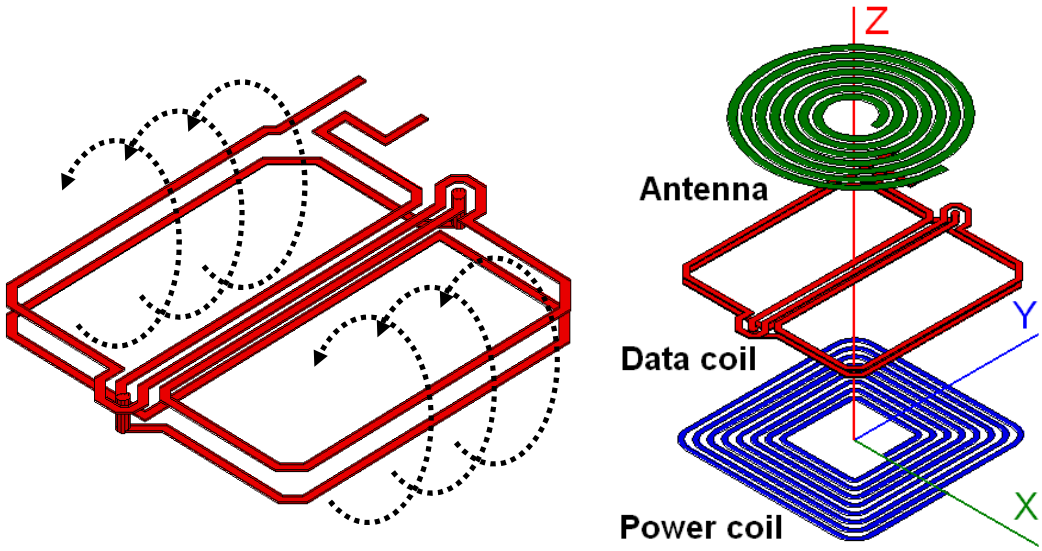

(a) (b)

Figure 4.4: (a) Planar figure-8 coil layout. (b) Exploded view of the UWB antenna stacked on top of the power PSC and figure-8 data coil in a 4-layer PCB to form the implantable side of the multiband wireless link (10×10×1.5 mm^3).

4.2 Multiband Wireless Link Design Procedure

The multiband design includes a power carrier, forward data, and back telemetry. The power carrier is introduced in Section 4.1.2, and the data links are discussed in Section 4.1.3. The design procedure includes not only optimal geometry of each link but the mutual coupling between each other.

4.2.1 Power PSC

The studies of optimization of power PSC has been summarized in Chapter 3 [3] and combined the theoretical foundation of optimal power transmission in inductive links with simple models [5]. Please note that the eddy current is not included in the model [5], in this preliminary design. Table 4.1 summarizes the design constraints for visual prosthesis application by a standard PCB fabrication process, and Table 4.2 depicts the optimized geometries for L_1 and L_2.

Table 4.1. DESIGN CONSTRAINS IMPOSED BY APPLICATION AND FABRICATION PROCESS

Parameter	Symbol	Design Value
Implanted PSC outer side	d_{o2}	10 mm
PSCs relative distance	D	10 mm
Link operating frequency	f	13.56 MHz
Secondary nominal loading	R_L	500 Ω
Conductor thickness	t_c	38 μm
Substrate thickness	t_s	1.6 mm
Substrate dielectric constant	ε_{rs}	FR4, 4.4

Table 4.2. OPTIMIZED POWER PSC GEOMETRIES AND SPECIFICATIONS

Parameter	L_1	L_2	Parameter	L_1	L_2
d_o (mm)	79	10	w (μm)	5500	290
d_i (mm)	11.2	2.96	s (μm)	150	150
φ (fill factor)	0.751	0.543	L (μH)	1.22	0.49
N (turns)	6	8	Q	102	36
Frequency (MHz)	13.56				
k_{12}	0.036				
Efficiency (%)	56.65				

*Derived from using Table 4.1 in the iterative procedure explained in [5].

4.2.2 Vertical Data Coils

In this prototype, a synchronous frequency shift keyed (FSK) carrier at f_{FD1} = 25 MHz and f_{FD0} = 50 MHz is chosen based [9] for the forward data carrier frequency. Figure 4.2a shows the geometrical parameters of the data coils (l_d, w_d, h_d, n_d). Figure 4.5 summarizes three-step design procedure. The first constraint is the size of the IMD [7]. In order to reduce thickness of L_4, the multi-strand Litz wires (MWS Wire Industries, Westlake Village, CA) are used. This wire had a diameter of Dia_4 = 100 μm with seven insulated strands of AWG-48 wires. Using Table 4.2, $l_{d4} = d_{o2} + 2Dia_4$ = 10.2 mm. The height of L_4, h_{d4}, is dictated by the IMD thickness. Increasing n_{d3} and n_{d4} improves k_{34} at the expense of decreasing the coils' self resonant frequency (SRF) and increasing undesired k_{14} and k_{23}. SRF is defined as

$$\text{SRF} = 1/2\pi\sqrt{LC}\ , \tag{4.2}$$

where L is the data coils' self-inductance, and C is their parasitic capacitance. As a rule of thumb, SRF should be at least twice the carrier frequency [69], [110]. Hence, $SRF_{3,4} \geq$ 100 MHz. Figure 4.6 shows the HFSS simulated relationship between SRF and n_{d4} for a single strand rectangular coil with l_{d4} = 10.2 mm, h_{d4} = 1.7 mm, w_{d4} = 1 mm and Dia_4 = 100 µm. It can be seen that n_{d4} = 6, SRF_4 = 96.3 MHz in simulation and SRF_4 = 98.8 MHz in measurement.

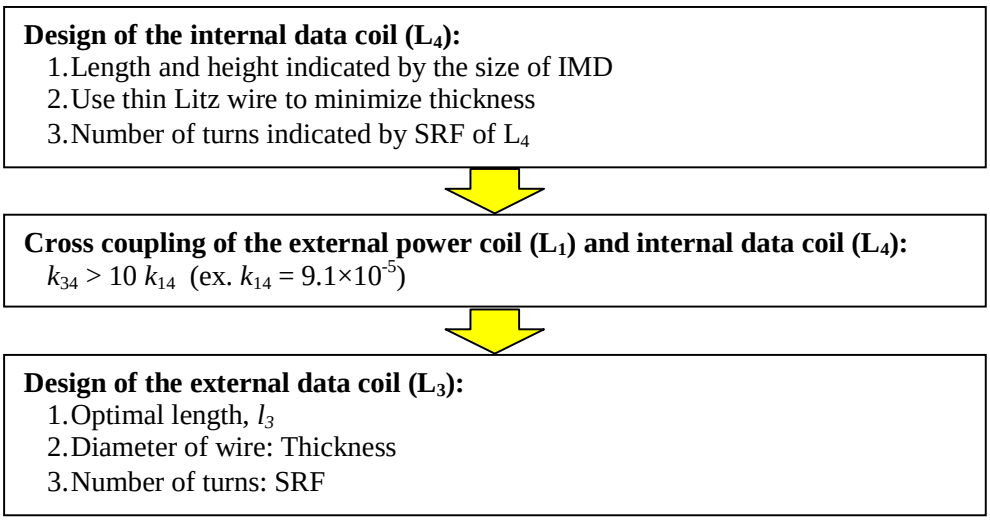

Figure 4.5: Design procedure for optimal design of the vertical data coil.

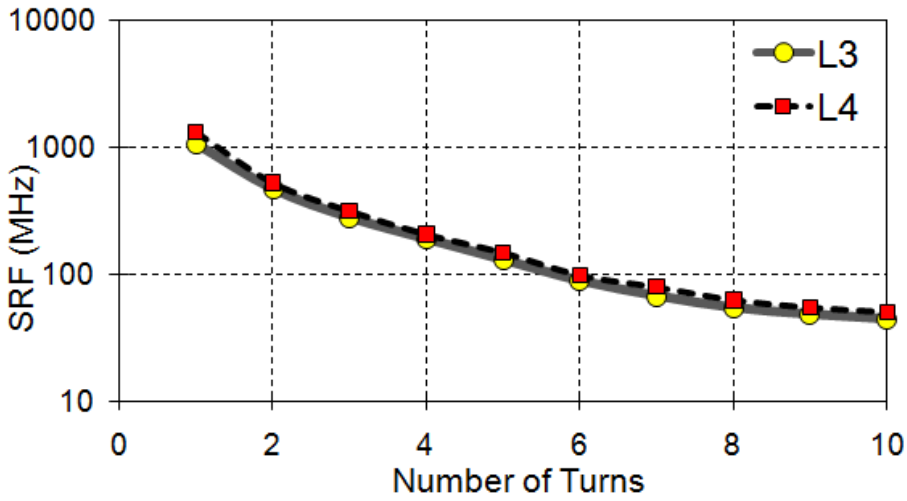

Figure 4.6: Self resonance frequency *vs.* number of turns for the vertical data coils.

In the second step, since dimensions of L_1 and L_4 as well as their relative distance, D, are known, k_{14} can be found by using a field solver to determine the power carrier interference. D is considered the distance between the closest conductors in L_1 and L_4. In the simulation result, $k_{14} = 9.1\times10^{-5}$ at 25 MHz, which is the minimum value for k_{14} when the coils are perfectly aligned. However, since the interference can be through multiple paths, the best alignment can be found by shifting L_4 horizontally about 0.5 mm in each direction from the center of the power coil. In the next step, L_3 should be designed such that k_{34} is at least an order of magnitude larger than k_{14}. A short l_{d3} turns L_3 into a solenoid with concentrated magnetic field but smaller cross section. If l_{d3} is too long, on the other hand, L_3 turns into a series of infinite parallel conductors with lower mutual coupling. Hence, there is an optimal length for l_{d3}. In order to demonstrate the effect of l_{d3} on k_{34}, Figure 4.7 shows k_{34} between L_4 and n_3 = 3, 5, and 10-turn L_3, by sweeping l_{d3} from 10 to 70 mm. Once again, D = 10 mm, and h_{d3} was set to 1.7 mm, because of PCB thickness. The results show that l_{d3} = 30 mm is the optimal length for L_3 in these conditions.

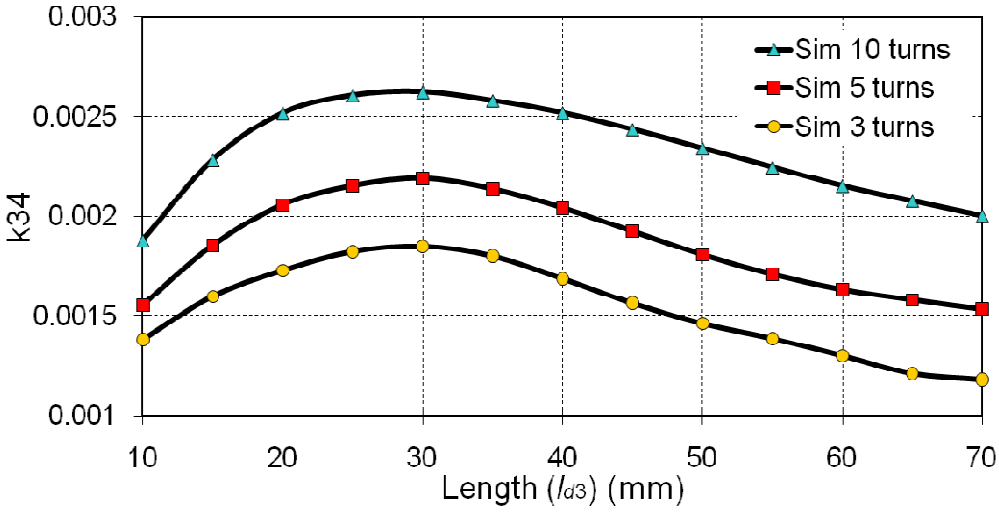

Figure 4.7: Vertical data coils direct coupling as a function of the length of L_3. D = 10 mm.

Dia_3 and n_{d3} are the other parameters, which have direct relationships with k_{34}. Figure 4.8 shows the results of k_{34} by sweeping Dia_3 and n_{d3} from 0 to 0.5 mm and 0 to 10 turns, respectively. Despite their positive effect on k_{34}, increasing Dia_3 would add to the thickness of the external coil/antenna complex, and increasing n_{d3} reduces SRF_3. The wire of L_3 is still Litz wires with Dia_3 = 350 μm, made of an insulated AWG-36 strands. This type of wire indicated by a dashed line in Figure 4.8, adds ~700 μm to the 1.6 mm thick L_1. Regarding the optimal value of n_{d3}, SRF_3 with all the known geometrical parameters of L_3 is simulated, and it can be seen in Figure 4.6 that n_{d3} = 5 would be the best choice, resulting in SRF_3 = 128.8 MHz. This point has been shown by a red dot in Figure 4.8, corresponding to k_{34} = 0.00246, which is 27 times larger than k_{14}. This concludes the optimal vertical data coils design, which specifications are listed in Table 4.3, for D = 10 mm.

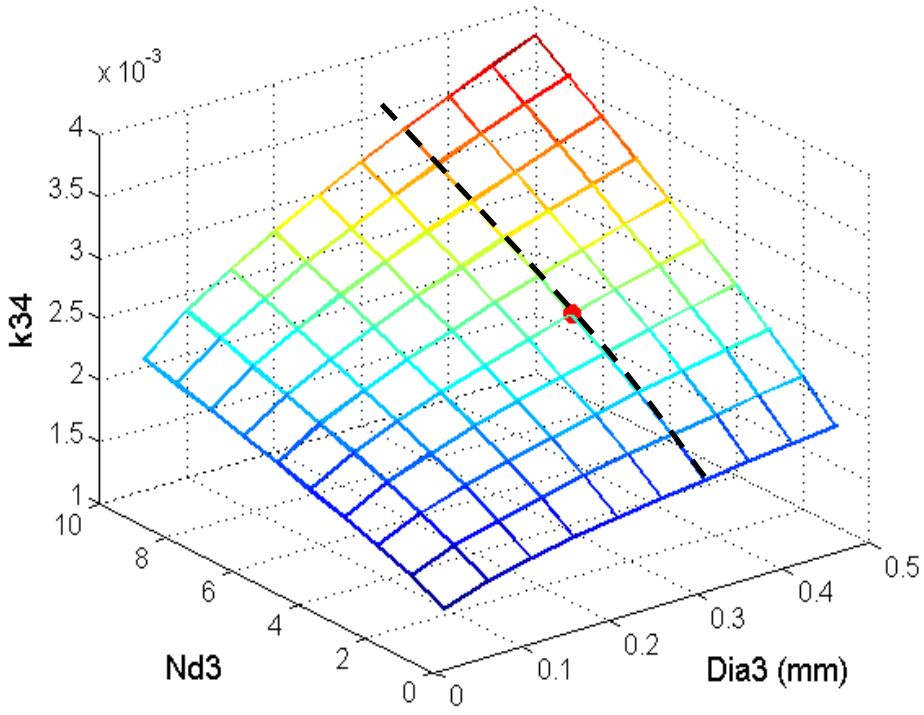

Figure 4.8: The variation of turns and the diameter for the external data coil (L_3).

Table 4.3. OPTIMIZED VERTICAL DATA COIL CHARACTERISTICS

Parameter	**L_3**	**L_4**
Type of Litz wire	7 × AWG-36	7 × AWG-48
Wire Diameter (μm)	350	100
Number of Turns	5	6
Length (mm)	30	10.2
Width (mm)	2.0	1.0
Height (mm)	2.2	1.7
Inductance (μH)*	0.3081	0.5972
SRF*	128.8	98.8
C_{s3} and C_{p4} (pF)	58.46	27.9
Q @ 50 MHz*	50.2	20.2
k_{34}*	0.0022	

*Simulated in HFSS.

4.2.3 Figure-8 Data Coils

Figure 4.4a shows the figure-8 data coil (L_4) geometry. Note that the two loops are laid out symmetrically with opposite winding directions. Similar to the vertical data coils, the largest possible area for L_4 is dictated by the IMD size, which is the size of L_2 (d_{o4} = 10 mm). The line width for L_4 to be 200 μm is chosen, slightly larger than the minimum widths possible in our PCB fabrication process. Layers-2 and -3 of a 4-layer FR4 PCB are dedicated to the implantable figure-8 data coil, which are spaced at 0.8 mm. The simulated SRF_4 with the above dimensions was 256 MHz. In order to find the best size for L_3, the coil design is learned from that the optimal radius of a 1-turn circular loop for maximum coupling with another loop that has a radius of R at distance D is ~$D\sqrt{2}$, when R is small. Since $D = R$ = 10 mm in this design, the size of L_3 is 32 × 32 mm^2, which is slightly larger than the optimal size to account for the width of the planar conductors. The line width affects not only the parasitic resistance but SRF_3. Hence, a line width of 2.0 mm is used on a 2-layer 1.6 mm thick PCB, and L_3 achieves SRF_3 = 138 MHz in simulations. Specifications of the figure-8 data coil designs and characteristics are summarized in Table 4.4.

Table 4.4. OPTIMIZED FIGURE-8 DATA COIL CHARACTERISTICS

Parameter	**L_3**	**L_4**
Line width (mm)	2	0.2
Size (mm^2)	32 × 32	10 × 10
Number of turns	2	2
Inductance (μH)*	0.1306	0.3338
SRF (MHz)*	138	256
C_{s3} and C_{p4} (pF)	137.9	52.80
Q @ 50 MHz*	46.4	38.8
k_{34}*	0.011	

*Simulated in HFSS.

4.2.4 UWB Antenna

In the compact design, spiral geometry for the UWB back telemetry antenna is used, and this design took advantage of the power coil as its ground plane. The antenna consists of seven turns of planar copper with the line width of 400 μm and line spacing of 200 μm on the backside of L_2. The feed point of the UWB antenna is at the center, and its diameter is 10 mm. However, this rough design only provides a preliminary concept, and the design of UWB antenna based on the special geometry needs to be improved in the future. However, a key advantage of this design is that it can be batch fabricated on a thin organic substrate with minimum size overhead in an actual IMD. Figure 4.4b shows an exploded view of the entire multiband coil/antenna complex on the implantable side, implemented on a 4-layer PCB.

An alternative way for multiband module is the commercial UWB chip antenna, which is mounted on the side of the power PSC and forward data coil. Although this additional antenna increases the size of the module, this antenna can provide a better performance. The chip antenna is made by ceramic (3100AT51A7200E, Johanson Tech. Inc., Camarillo, CA) in 6.0 ×10.0 × 1.2 mm^3, and the bandwidth is 3.1 to 10.3 GHz. Figure 4.9 shows the design of the module, and the spacing of the UWB antenna and coils is 4.8 mm.

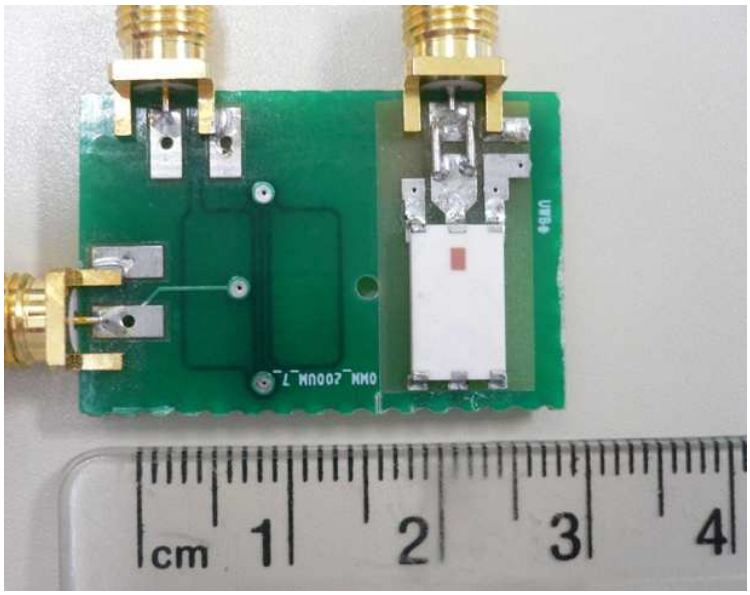

Figure 4.9: Receiver data and power coils on a 4 layer FR4 PCB (10 mm by 10 mm) with a commercial chip antenna (3100AT51A7200E, Johanson Tech).

4.3 Simulation and Measurement Results

The measurement setup is shown in Figure 4.10. The coils are connected to a 4.0 GHz vector network analyzer (R&S ZVB4) in pairs to measure their S-parameters. The S-parameters were then converted to Z-parameters to calculate the quality factors, mutual inductances, and PTE [118]. Since $d_{o1} > l_3$ (see Tables 4.2 and 4.3), a pair of via holes are create4d in L_1 PCB and pass the Litz wire through them in order to wind L_3 (Figure 4.10). The detailed power PSC design for maximum PTE and measurement results are discussed in Chapter 3 and Table 4.2. Hence, the mutual effects of each link are discussed in this section.

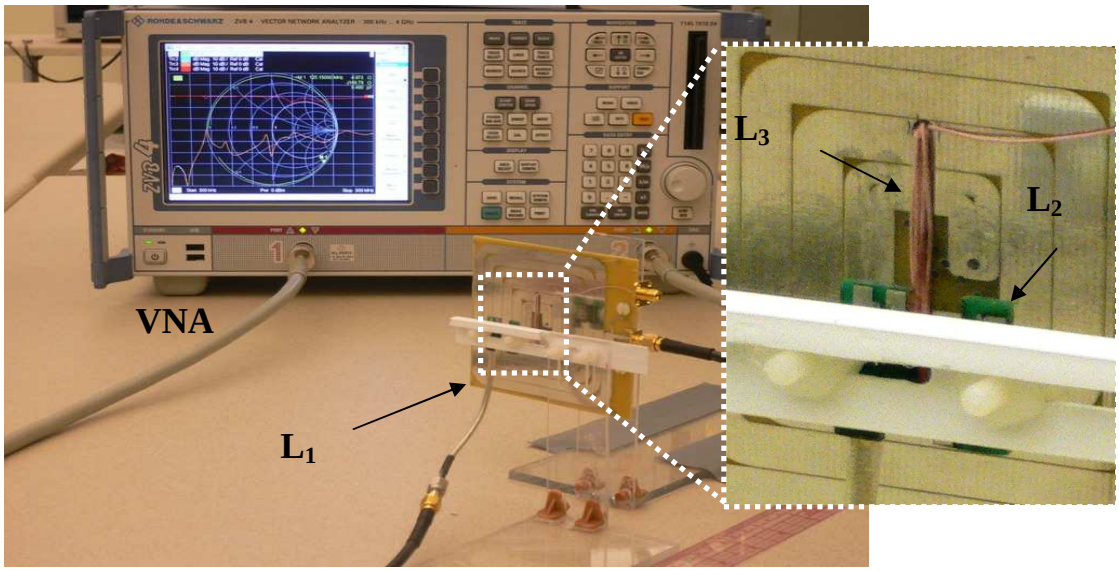

Figure 4.10: Setup for direct- and cross-coupling measurements. Inset: the relative position of the external power (L_1) and vertical data coils (L_3) with respect to implantable coils (L_2 and L_4), which are also shown separately in Figure 4.2b.

4.3.1 Linear Misalignments of Data Coils

One of the key issues in forward data transmission using a multiband wireless link is its robustness against misalignments. The misalignment along the X-axis (see Figure 4.2a) is more important than that long Y-axis as discussed. Figure 4.11a shows the result of k_{14} and k_{34} variations at D = 10 mm when vertical data coils are misaligned up to 10 mm along the X-axis. It can be seen that the desired k_{34} appears well above the undesired interference from power PSCs (k_{14}) in perfect alignment (ΔX = 0 mm) and $k_{34} > k_{14}$ for ΔX < 2.5 mm. Therefore, the conclusion is that this design can generally withstand misalignments of up to 2.5 mm for the 10×10 mm^2 implant (~25% of the implant size).

A similar set of experiments were conducted with figure-8 data coils of Section 4.2.3, and the results in Figure 4.11b show that both k_{14} and k_{34} of figure-8 coils are stronger than k_{14} and k_{34} of the vertical data coils when coils are perfectly aligned. In this

design, however, $k_{34} > k_{14}$ for $\Delta X < 8$ mm. The conclusion is that this design can withstand misalignments of up to 8 mm for the 10×10 mm^2 implant (~80% of the implant size). However, the interference, k_{14}, of figure-8 data coil is also higher than that of vertical data coil.

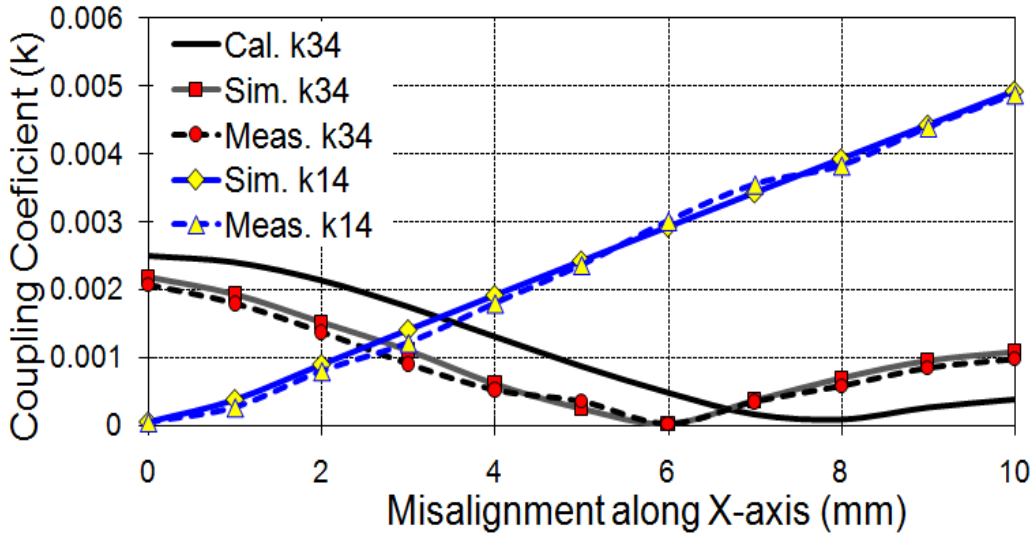

(a)

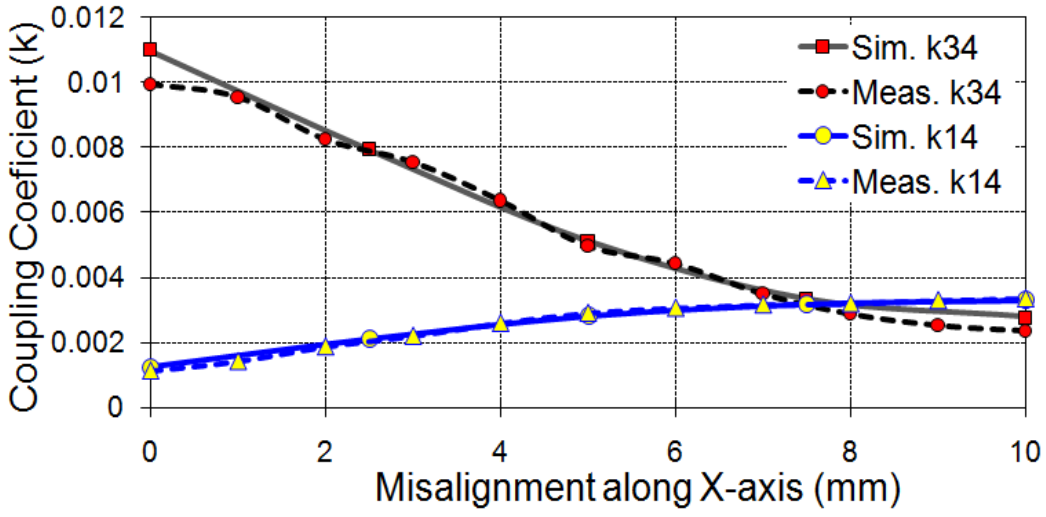

(b)

Figure 4.11: (a) Calculation (see Appendix A), simulation, and measurement of vertical data coils' direct coupling (k_{34}) and cross coupling with power PSCs (k_{14}) *vs.* misalignment along the X-axis (see Figure 4.2a). (b) Simulation and measurement of figure-8 data coils' k_{34} and k_{14} *vs.* misalignment along the X-axis (see Figure 4.8b). Coils relative distance is maintained at D = 10 mm.

4.3.2 Data Coils Rotations (Tilting Issues)

Due to coils' proximity, even small rotations affect their coupling coefficients considerably. In this section, simulations and measurements of the vertical and figure-8 data coils' k_{34} *vs.* the rotation angle are shown in Figs. 4.12a and 4.12b based on the Cartesian coordinates shown in Figs. 4.2a and 4.4b, respectively. In these measurements, L_4 is held stationary and L_3 is rotated pivotal to X-, Y-, and Z-axes, while the center to center spacing between the coils is maintained at D = 10 mm.

According to Figure 4.12a, rotations along X- and Y-axes actually increase k_{34} in vertical data coils. In figure-8 coils, however, all rotations result in k_{34} reductions. Nevertheless, without considering the changes in k_{14} it is not possible to draw any conclusions on the effects of rotations. k_{14} was too small to be shown in the same scale as k_{34}. Hence, k_{34}/k_{14} should be considered as a figure of merit (FoM) to compare the data coil designs.

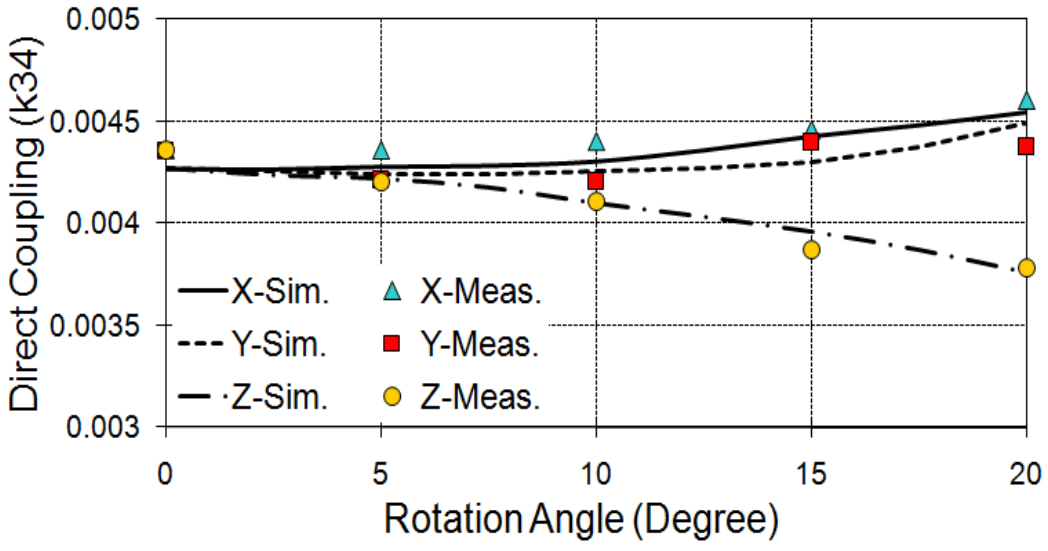

(a)

Figure 4.12: (a) Simulation and measurement results of the vertical data coils direct coupling (k_{34}) vs. rotation angle of L_3 pivotal to the X-, Y-, and Z-axes, while maintaining a center to center spacing of D = 10 mm. (b) Similar simulation and measurement results for figure-8 data coils while maintaining a center to center spacing of D = 10 mm.

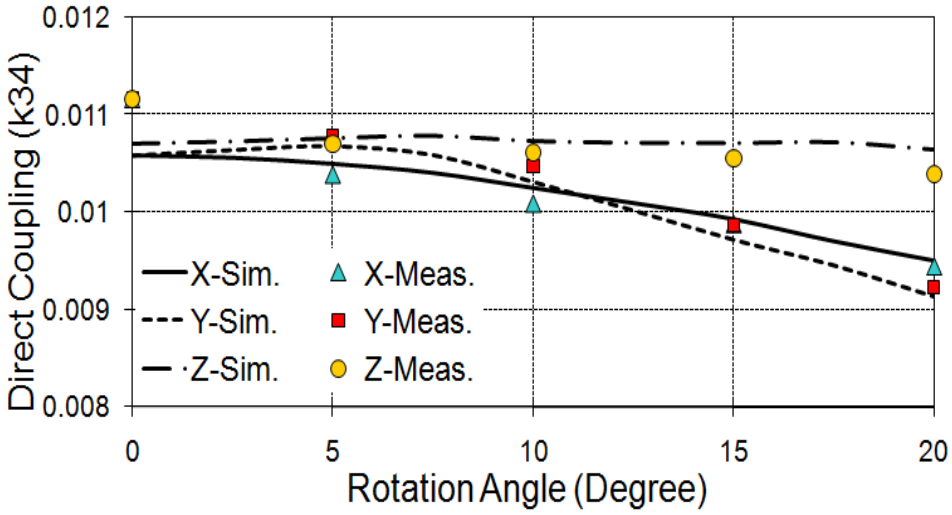

(b)

Figure 4.12: (b) Similar simulation and measurement results for figure-8 data coils while maintaining a center to center spacing of *D* = 10 mm.

4.3.3 Comparison of Data Coils

Figs. 4.13a and 4.13b show k_{34}/k_{14} *vs.* linear misalignments and rotations, respectively. The level at which $k_{34}/k_{14} = 1$ is a good measure for indicating how much misalignment or rotation can be handled by each coil design. It can be seen in Figure 4.13a that when the coils are perfectly aligned, vertical data coils are in a stronger position. However, they are affected by X-axis misalignment more rapidly than figure-8 coils. According to Figure 4.13b, vertical data coils are more robust against rotations pivotal to X- and Z-axes compared to figure-8 coils. In larger than 10° rotations pivotal to the Y-axis, however, figure-8 coils are stronger. Because this type of rotations affect the orthogonal advantage of the vertical data coils and increase their exposure to power PSCs magnetic flux (see Figure 4.2a).

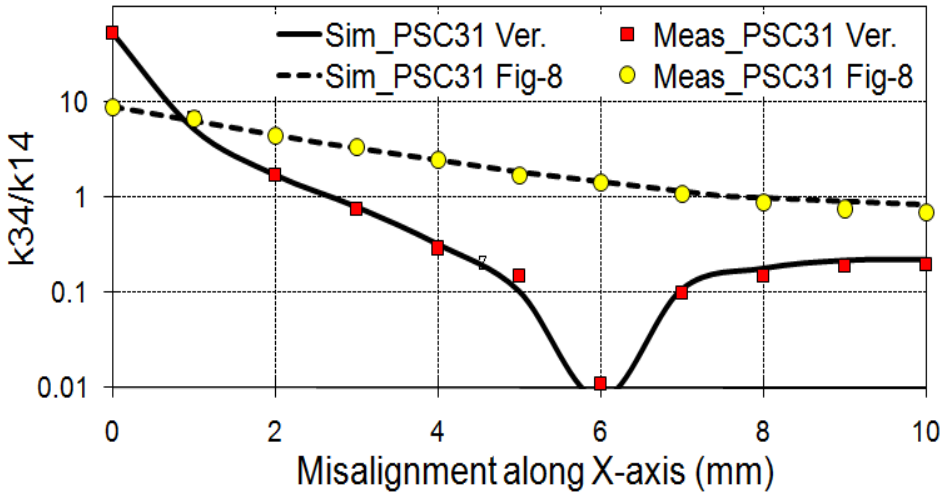

(a)

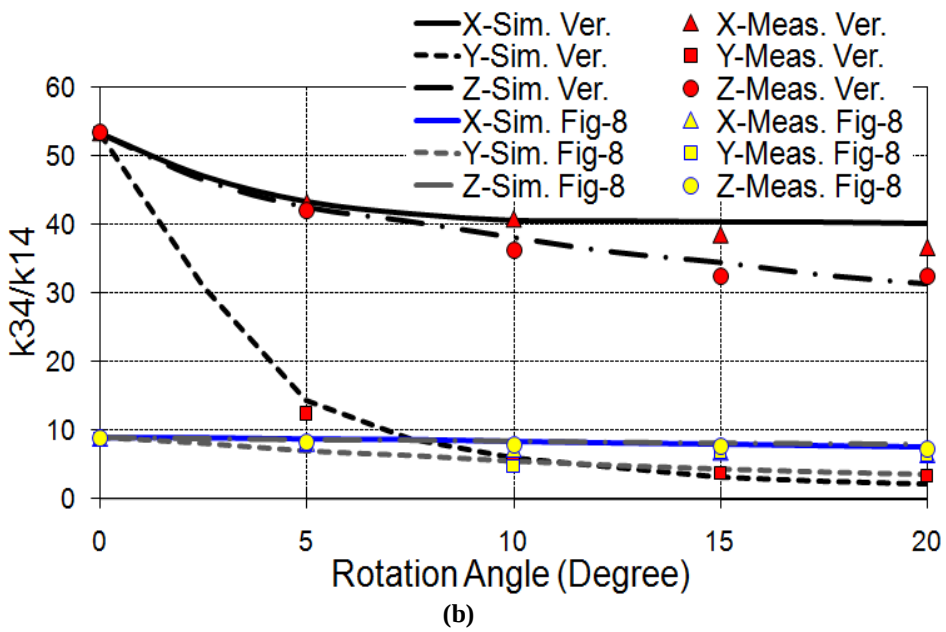

(b)

Figure 4.13: (a) Comparing k_{34}/k_{14} ratio between vertical and figure-8 data coils *vs.* linear misalignment along the X-axis. (b) Comparing k_{34}/k_{14} between vertical and figure-8 coils *vs.* rotations. Coils relative distance is maintained at D = 10 mm.

4.3.4 Power PSC and Data Coils Cross Coupling

By inspecting Figure 4.1, however, one can see that there are two other possible paths for this interference. One is the coupling from L_1 onto L_2 (the power link) and then from L_2 onto L_4. This can be represented by $k_{12} \times k_{24}$. The other is from L_1 onto L_3 and then from L_3 onto L_4 (the forward data link), which can be represented by $k_{13} \times k_{34}$.

Between these two, it is expected $k_{12} \times k_{24} > k_{13} \times k_{34}$ because of the strong coupling between L_1 and L_2 (k_{12}). In order to understand the significance of these undesired coupling paths, all three paths *vs.* X-axis misalignment in Figure 4.14 and 4.15 should be compared. Fig 4.14 shows that in vertical data coils, even though $k_{12} \times k_{24}$ and $k_{13} \times k_{34}$ are comparable to k_{14} in perfect alignment ($k_{14} = 3.9\times10^{-5}$ *vs.* $k_{12} \times k_{24} = 1.1\times10^{-5}$), they remain at about two orders of magnitude below k_{34}. Therefore, these indirect interference paths in vertical data coils can be neglected.

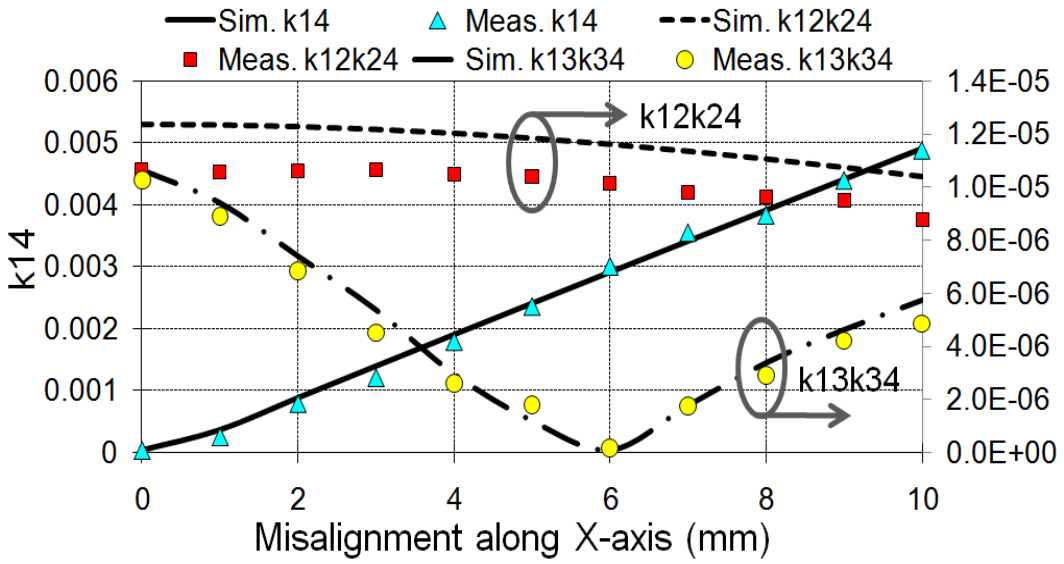

Figure 4.14: Calculation (see Appendix A), simulation, and measurement of the effect of misalignment along X-axis on indirect coupling paths in vertical data coils (see Figure 4.2a).

Figure 4.15 shows the same comparison for figure-8 data coils. In this case, $k_{13} \times k_{34}$ is very small and can be ignored. However, k_{14} and $k_{12} \times k_{24}$ are close at perfect alignment ($k_{14} = 0.8\times10^{-4}$ vs. $k_{12} \times k_{24} = 4.0\times10^{-4}$), and $k_{12} \times k_{24}$ remains smaller but comparable to k_{14}. One possible way of taking advantage of $k_{12} \times k_{24}$ is to make sure that its sign is opposing that of k_{14}. This is possible by proper selection of the direction of windings in L_1 and L_2. The result would be that in the power carrier interference through

$k_{12} \times k_{24}$ would be out of phase with the main source of interference through k_{14} and slightly weakened it.

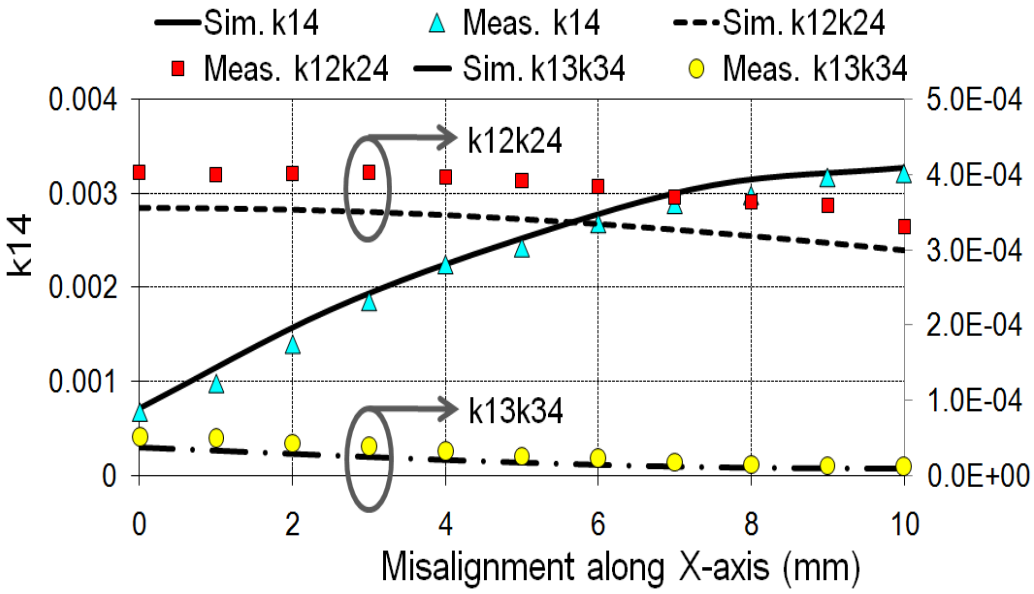

Figure 4.15: *D* = 10 mm. Effect of misalignment along X-axis on indirect coupling paths in figure-8 data coils (see Figure 4.4b).

4.3.5 UWB Antenna

Figure 4.16a shows the simulation and measurement results for the S_{11} pattern of the planar spiral UWB antenna (A2), stacked on top of the power PSC and figure-8 data coils in a 4-layer PCB, shown in Figure 4.4b. These three components, which occupy 10 × 10 × 1.7 mm^3 in the current implementation, form the implantable side of the multiband wireless link, shown on the right side of the skin in Figure 4.1. The feed point in this measurement was in the center of the spiral antenna. The spiral UWB antenna has a radiation bandwidth from 2.5 to 5.0 GHz with S_{11} < -10 dB, which is expected to be sufficient for transmitting tens of Mbps of recorded data across a short distance (10 mm) using IR-UWB technique [124]. Figure 4.16a also shows the S_{11} pattern when the vertical data coil is added to Figure 4.4b combination, as seen in Figure 4.2b. The vertical data

coil affected the frequency response of the antenna, and the 2.5 - 5 GHz window was no longer available. Therefore, the spiral UWB antenna design needs to be modified if it is intended to be used with vertical data coils. It should be noted that at high frequencies, electromagnetic power absorption in the tissue can increase the antenna losses . The multiband module with commercial UWB antenna, as shown in Figure 4.9, is also measured, and the result is shown in Figure 4.16b. It can be seen that although this module has larger size (20 × 12 × 1.7 mm^3), the bandwidth of UWB antenna is 3.1-10.8 GHz, which meets the standard UWB specification. However, these measurements are in the air environment. For the IMD, one should consider evaluating such antenna designs in saline and other tissue stimulants [125].

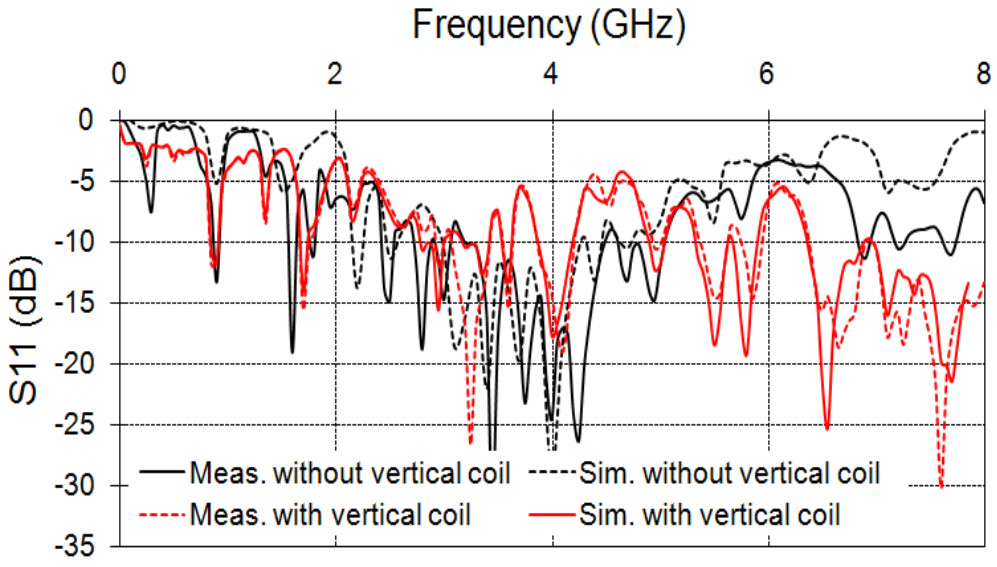

Figure 4.16: (a)Simulation and measurement of S_{11}, with and without the vertical data coil, for the UWB spiral antenna that is implemented on the same PCB as L_2 and figure-8 L_4, as shown in Figure 4.4b.

Another measurement of the multiband module as shown in Figure 4.9 is based on the commercial chip antennas (3100AT51A7200E, Johanson Tech. Inc., Camarillo, CA), which has band width from 3.1 to 10.3 GHz, and the measurement results for with and

without coils are shown in Figure 4.17. From Figure 4.17, the PCB coils do not affect the bandwidth of the UWB antenna.

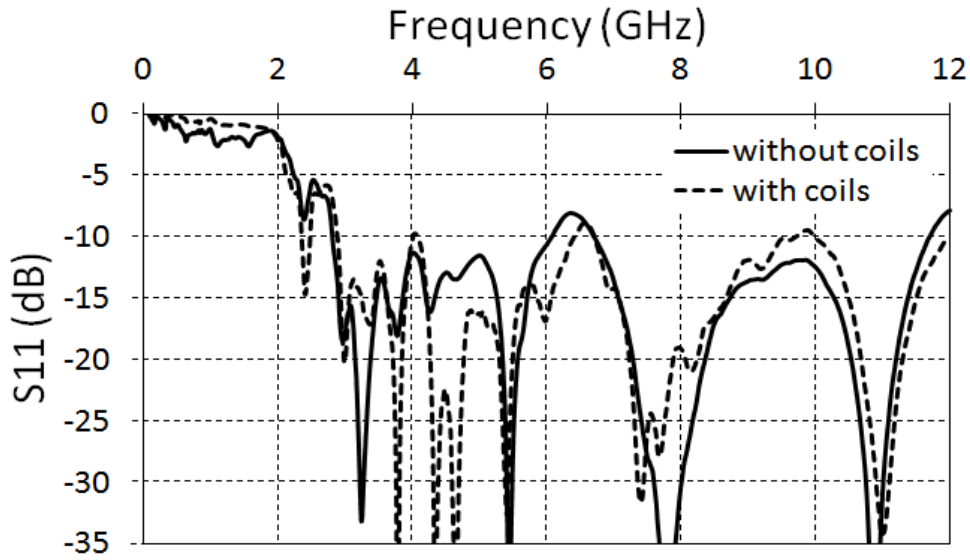

Figure 4.17: Measurement result of commercial UWB antenna with and without multiband module.

4.4 Conclusions

This chapter has presented a novel method for the design and optimization of a multiband wireless link that has a dedicated carrier signal and the coil/antenna pair for every major function that is expected from the wireless link across the skin barrier in a high performance implantable neuroprosthetic device, such as a visual prosthesis. Previously, the optimization of the PSC geometries for efficient power transmission is described in Chapter 3. In Chapter 4, a pair of PSCs, optimized in the air at 13.56 MHz, is used as the foundation for optimization of two types of coils for forward data transmission, vertical coils and figure-8 coils. The characteristic of the two types of the data coils have been analyzed in this chapter.

Considering that the power carrier at the external transmitter can be up to two orders of magnitude larger than the data carrier, minimization of the power carrier

interference on the implanted receiver data coil is of utmost importance. Vertical coils take advantage of the fact that orthogonal coils, which are symmetrical, ideally have no cross coupling. Figure-8 coils, on the other hand, take advantage of their differential windings to attenuate the effects of any common mode external electromagnetic field. A detailed comparison between the vertical and figure-8 coils revealed that the former leads to lower interference when coils are perfectly aligned, while the latter is more robust against linear misalignments. With respect to rotations, the results are mixed, but vertical coils can generally perform better. For invasive BMIs, since the movement of the modules would be very small, the vertical data coil is a suitable choice. On the other hand, the retinal implant usually has external module outside of the body, for example, the external circuit module can be design on the frame of a glass. Hence, the figure-8 data coil would be a better design.

Most of the calculations, simulations, and measurement results were in close agreement within the range of parameters needed for neuroprosthetic applications. One major deviation from practical conditions, however, was air as the surrounding medium around the coils, as opposed to neural tissue. Therefore, the optimal number of turns and size of the coils are expected to be reduced, particularly for external coils, as shown for power PSCs in [5]. On the other hand, since the permeability of tissue is close to that of the air, the difference between k in air and tissue will be small. The same design criteria that are proposed here will be applicable in the tissue.

The coil design for implantable device is introduced in Chapter 3 and 4. In latter chapters, the topic will move to long term wireless power and data communication for freely moving animal experiment.

CHAPTER V

THE ENERCAGE SYSTEM DESIGN

Bioinstruments used for long-term biological data acquisition, stimulation, and drug delivery on awake freely behaving small animal subjects usually involve cables to provide power and data [126]. However, most physiologists, particularly those who record large volumes of data from the central nervous system through multiple parallel channels, conduct their *in vivo* experiments with behaving animals that are tethered to large electrophysiology instruments without taking advantage of numerous benefits of the wireless data acquisition systems [13], [15].

In this chapter, the development of the Enercage system, a novel wireless-data acquisition system composed of a stationary base and a mobile unit (headstage) is introduced. The system can track the location of a small animal by threshold of the magnetic field produced by the headstage. Furthermore, EnerCage provides wireless power for on-board electronics of the mobile unit, which is the bionistruments. The EnerCage system has three main features:

1. A modular overlapping hexagonal-planar spiral coil (hex-PSC) array: inductive power and data transmission take place through a scalable array of PSCs that are implemented on a printed circuit board (PCB). This array can conform to an arbitrarily shaped experimental field, and the PSC geometries are optimized to maximize the power transfer efficiency (PTE) in response to misalignments. In other words, the transmitter (Tx) PSC array allows the receiver (Rx) coil to move from one PSC to another with minimal variations in the PTE.

2. Non-line-of-sight three-dimensional (3D) magnetic tracking: an array of three-axis magnetic sensors has been layered under the PSCs to track the 3D position and the orientation of a small magnetic tracer embedded in the headstage [30]. A smart algorithm running on the external controller, a central personal computer (PC) station, selects and activates the PSCs that are in the best position to deliver power to the Rx coil. The magnetic 3D tracking can operate in both open and covered spaces, such as tunnels, which might be a more natural environment for burrowing animals.

3. Closed-loop power control: the EnerCage power carrier is set at a carrier frequency, f_c, of 13.56 MHz to comply with the industrial, scientific, and medical (ISM) band [60]. The power-control mechanism uses commercially available off-the-shelf (COTS) high-frequency radio frequency identification (HF-RFID) chips to close the inductive power delivery/load shift keying (LSK) back telemetry loop [36]. The system can actively compensate for variations in the coils' coupling resulting from misalignments, tilting, or distance variations in real time to ensure a smooth power transfer to the headstage or implant.

A rendering of the proposed EnerCage system is shown in Figure 5.1. A wireless mobile unit, which is a headstage carrying the Rx coil, is inductively powered by an array of overlapping hex-PSCs that tile the floor of the experimental arena. The control circuitry has been implemented on modules that are mounted vertically under the PSC array to form the stationary unit. An array of three-axis magnetic sensor modules (red dots), evenly distributed under the hex-PSC array, locates a small permanent magnet embedded in the center of the Rx coil. The proof-of-concept prototype EnerCage system described in this paper includes five PSCs and five sensors, providing a 305 cm^2 active

experimental arena. A simple threshold-based algorithm has been used for magnetic localization [21] in this area. The size of the PSCs was optimized for use with a wireless integrated neural recording (WINeR) system-on-a-chip [127] with a funnel-shaped headstage for 32 movable tetrodes [105]. A simple threshold-based algorithm has been used for magnetic localization in lieu of the precision 3D tracking in [21].

The following section provides more details on the EnerCage system architecture and key features, such as the design of the PSC array, the closed-loop power control, and the magnetic sensor tracking mechanism. Measurement results of the system functions are included in Section 5.3, followed by concluding remarks.

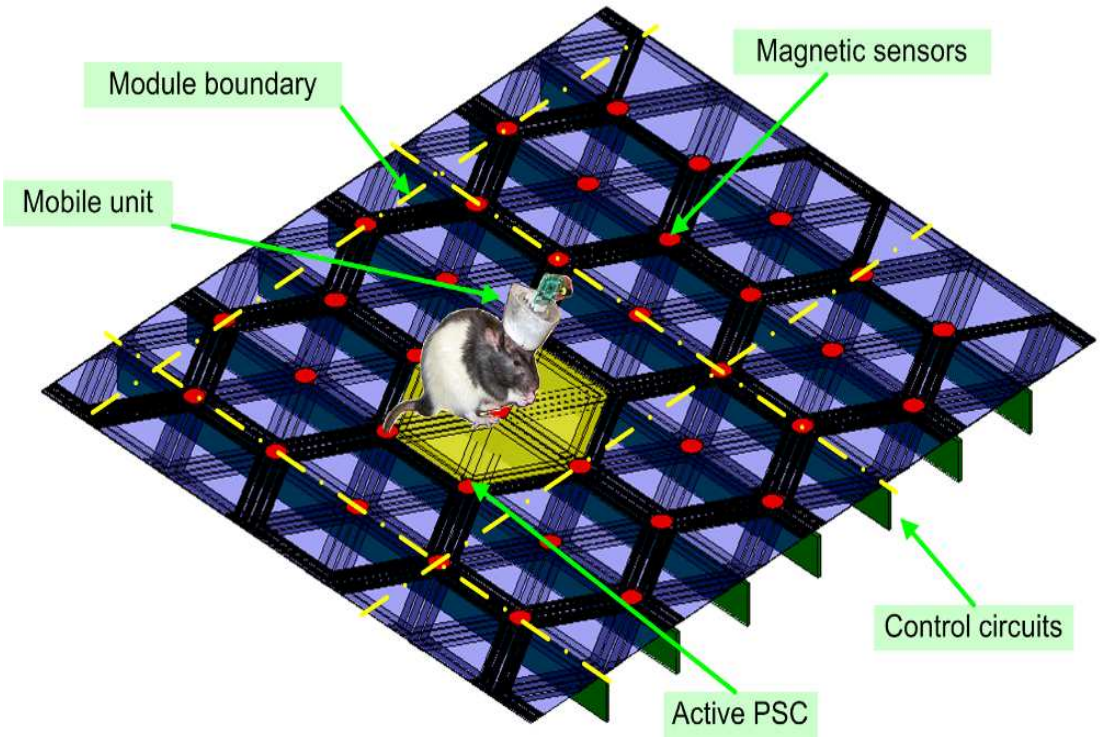

Figure 5.1: A rendering of the EnerCage system with its modular architecture. An array of overlapping hex-PSCs, and a closed-loop power controller provides the mobile unit (animal's headstage) with constant power. An array of three-axial magnetic sensors (red dots) tracks the animal in real time.

5.1 The EnerCage System Architecture

The block diagram of the EnerCage system is shown in Figure 5.2a. Each hex-PSC is driven by a class-C power amplifier (PA) with 68% efficiency, which in turn is controlled by a HF-RFID reader chip (TRF7960, Texas Instruments, Dallas, TX). Every three PSCs and their associated RFID readers were controlled by a local microcontroller (MCU) (MSP430, Texas Instruments, Dallas, TX). The power amplifiers, RFID chips, and MCU are all implemented on a single control module, as shown in Figure 5.2b. This module is connected vertically to the hex-PSC array to minimize the electromagnetic interference. Each PSC normally creates a vertical magnetic field above its surface. However, when the Rx coil is tilted > 60º, the vertical field cannot sufficiently energize it. Hence, 2:1 multiplexers (MUX) are included in the control module to feed a pair of out-of-phase input signals at 13.56 MHz to the RFID readers to handle this situation. When two adjacent PSCs are simultaneously activated with out-of-phase signals, they create a horizontal field between them to power up the tilted headstage [23].

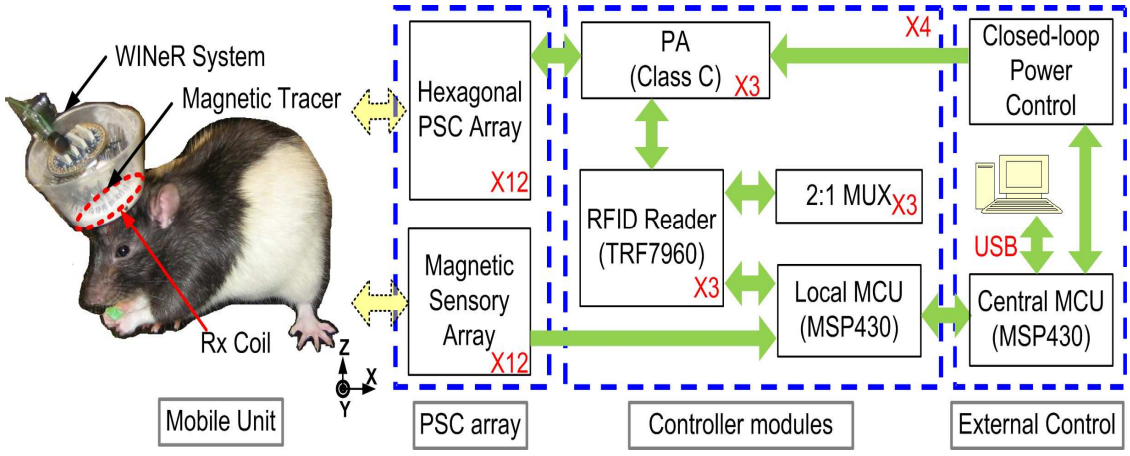

(a)

Figure 5.2: (a) Block diagram of the control electronics for every unit tile of the preliminary EnerCage system.

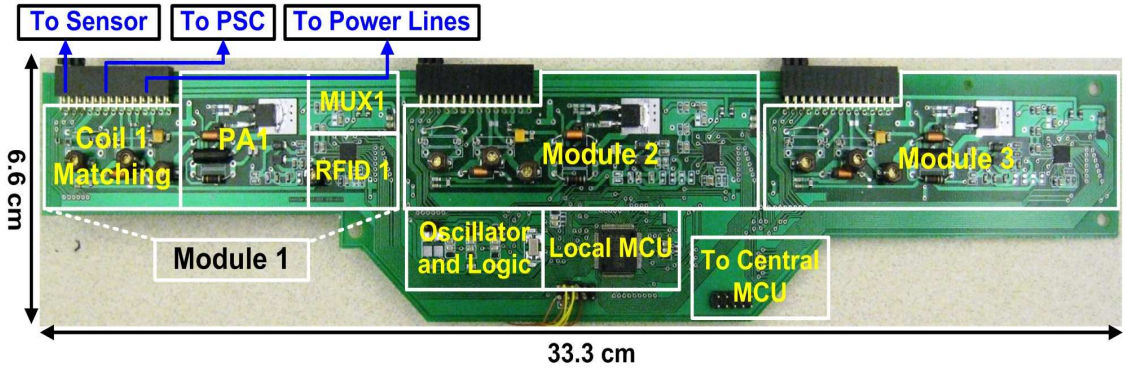

(b)

Figure 5.2: system. (b) PCB layout of the EnerCage control module for three independent PSCs.

In addition to delivering control signals, the local MCU is responsible for collecting the magnetic sensors' data for 3D tracking and the back-telemetry data (from the RFID readers) for closed-loop power control. Several local MCUs delivere the collected data to a central MCU (MSP430), which fuses all the data and relays it back to a central PC station via universal serial bus (USB) interface. The supply voltage for all class-C PAs on the controller modules is provided by a closed-loop power control block, which is also controlled by the central MCU [21].

5.1.1 PSC Design and Optimization

For the four-layer rectangular PSC module, the hex-PSCs for inductive power transmission are stacked in three layers (layer 1 to layer 3), and a fourth layer (layer 4) is used for interconnects between the hex-PSCs and their vertical controller modules, as shown in Figure 5.3a [27]. In the proof-of-concept prototype, two 2-layer (1.6 mm-thick) FR4 PCBs with 1-oz (35 μm-thick) copper are used to create the 4-layer structure, as shown in Figure 5.3b. The spacing of these two PCBs is 1.7 mm. Typically, conventional coil design for inductive power transmission is configured for the best-case scenario, in which an individual Tx coil is in perfect alignment with the Rx coil [4]-[7]. However, in this work, the hex-PSC array geometry is optimized to minimize coupling variations as

the Rx coil moved into and out of the worst-case overlapping and misalignment scenarios to provide a smooth power distribution to the headstage. In the worst case of overlapping, the black PSC1 in Figure 5.3a, (a layer 2 coil) is overlapped by six PSCs (1_1 to 1_6 in layer 1 and layer 3) and surrounded by six other PSCs (1_7 to 1_12 in layer 2). In this scenario, the largest parasitic capacitance and resistance is observed, resulting in the lowest quality (Q) factor and PTE between the PSC and the Rx coil [23]. The detailed issues (parasistic capacitance, parasistic resistance and mutual inductance) of this PSC layout will be presented in Chapter 6. The Rx coil is a wire-wound coil (WWC) [33], embedded in the headstage plastic molding for mechanical stability [38], and coil models were presented in [37]. The maximum lateral misalignment, γ_{max}, of the Rx coil happens at $1/\sqrt{3}$ of the PSC radius (r_{o1}) at a nominal coupling distance, D = 78 mm, a distance selected based on the nominal height of mature Long-Evans rats [127], [128].

Based on the conditions of coil coupling, the iterative design procedure introduced in Chapter 3 is used to maximize the PTE for the worst overlapping and lateral misalignments of the hex-PSCs. The PSC array architecture has been discussed here, but the detailed geometrical design of the optimal hex-PSCs will be described in Chapter 6 [23]. Following the theoretical design optimization, the HFSS field solver (Ansoft, Pittsburgh, PA) is used to verify and fine tune the PSC geometries, which are summarized in Table 6.1. The resulting PTE in the set of worst case conditions is 19.6%, which is quite appropriate for this application. The difference between measurement and simulation results is in part due to layer 4 metal patterns, which are approximated in the HFSS simulation model with parallel strips with the same coverage (48%) as the PCB layout (as shown in Figure 5.3d).

Table 5.1. ENERCAGE OPTIMAL COIL SPECIFICATIONS AT 13.56 MHZ

Parameter	Tx PSC (primary)	Rx coil (seconary)
Shape	Hexagonal PSC	Wire-wound
Outer diameter, d_o (mm)	168	40
Edge length (mm)	84	20 (Radius)
Number of turns	2	2
Copper trace cross section	35 μm × 10 mm	r_{wire} = 0.3 mm
Copper trace spaicng (mm)	3	~0.2
Coil inductance (μH)	0.88	0.38
Weight of copper (g)	3.6	0.7
Coil quality factor, *Q*	107	138
Nominal coupling distance, *D* (mm)	78	
Max*/Min magnetic field strength when 1 W is delivered to PSC (A/m)**	0.36 / 0.23	
Max/Min coupling coefficient, *k*	0.022 / 0.018	
Calculated Max/Min PTE (%)	43.1 / 28.8	
Simulated Max/Min PTE (%)	38.3 / 24.6	
Measured Max/Min PTE (%)	31.6 / 19.6	

* Perfect alignment. ** Maximum horizontal misalignment = 49.1 mm.

Once the optimal overlapping hex-PSC geometry is in place, it is fitted in the design of a PSC unit tile, (which comprises the floor of the experimental arena) while satisfying the constraints of the PSC manufacturing process. The layouts of the two 2-layer PCBs, shown in Figs. 6.3c and 6.3d, that are designed based on the specifications in Table 6.1. Each unit tile in this design includes five complete PSCs (two in layer 1, two in layer 2, and one in layer 3) enclosed by the dashed rectangle in Figure 5.3a, and 18 incomplete PSCs, which could form seven additional PSCs when attaches to an adjacent unit tile. Therefore, each tile has a total of 12 PSC driver coils, three for each of the four controller modules shown in Figure 5.2. Figure 5.3a also shows the layout of 23 overlapping hex-PSCs when completed by joining several adjacent tiles. This figure clearly shows how the EnerCage modular architecture can be scaled to support any arbitrarily-sized experimental arena. Each module also has 12 three-axis magnetic sensors, represented by the red dots within the unit tiles in Figure 5.1 and Figure 5.3a.

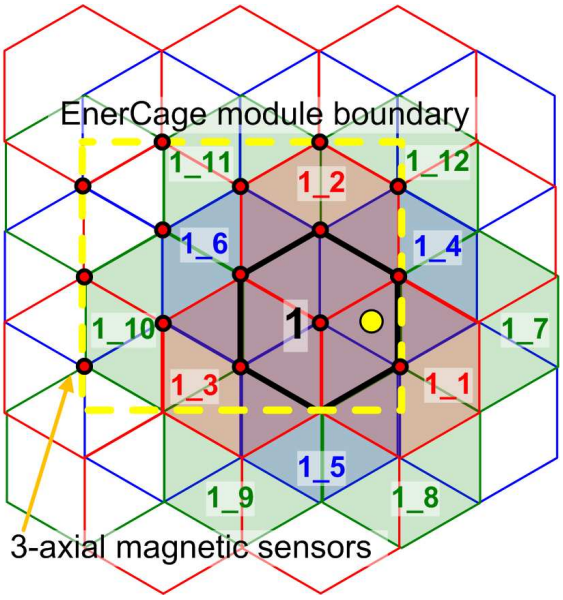

(a)

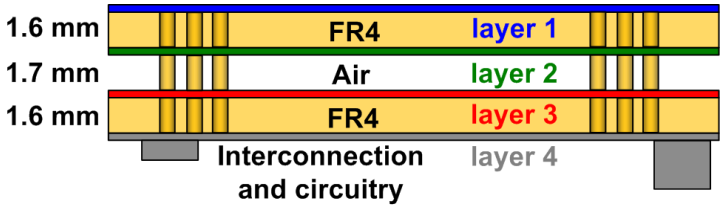

(b)

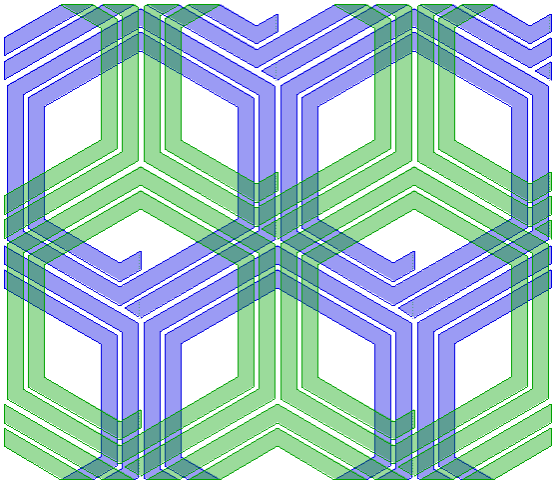

(c)

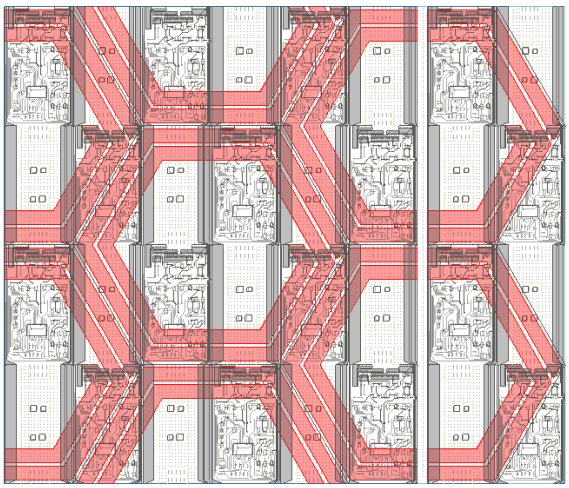

(d)

Figure 5.3: (a) The worst-case overlapping hexagonal PSC occurred to the black PSC1 in layer-2, which was surrounded by six PSCs in the same layer and overlapped by six other PSCs in layer-1 and layer-3. The worst-case lateral misalignment occurred at $\gamma_{max} = r_{o1}/\sqrt{3}$, which was indicated by a yellow dot. Each stationary unit tile (identified by a dashed-line) had 12 drivers and 12 magnetic sensors. (b) Cross section of the two two-layer PCBs forming the three overlapping hex-PSC layers plus an additional layer for interconnects. (c) PCB1 layout design for the unit tile of EnerCage (30.8 × 28.3 cm2) that provided layer 1 (red) and layer 2 (green). (d) PCB2 layout for layer 3 (blue) and layer 4 (gray).

5.1.2 Closed-loop Power Control Unit

The schematic diagram of the circuitry on the proof-of-concept mobile unit (headstage) and the global closed-loop power control unit (CLPC) [120] are shown Figure 5.4. The RFID reader, which serves as the power/data transmitter and receiver, drives a class-C PA, which is impedance matched to both the RFID output and the LC-tank. The mobile unit consists of a rectifier, a storage super capacitor, (C_s), a 3.0 V regulator, an LSK modulator (M_2), and an MCU (MSP430). The 13.56 MHz carrier is rectified by a full-wave rectifier, divided, ($0.458 \times V_{rec}$) and compared with an internal MCU reference voltage, V_{ref} = 1.5 V. If V_{rec} > 3.3 V, the LSK periodically shorts the Rx coil by closing M_2 at 700 Hz. These short pulses (20 μs wide) indicate that the received power is more than enough, and the Tx output power should be reduced. On the other hand, if V_{rec} < 3.3 V, no pulses are sent, indicating that the transmitter should increase power supplied in incremental steps. Each active RFID reader detects the back-telemetry data and sends it to the central PC station via the local and central MCUs.

The CLPC unit adjusts the Tx output power by providing a variable DC supply, Tx_V_{DD}, to all PAs. The CLPC consists of an MCU (MSP430), a digital potentiometer, and a DC-DC converter (LT1370) with >85% efficiency, as shown in Figure 5.4. Tx_V_{DD} is adjusted by the digital potentiometer (AD5160) from 5 V to 8.5 V in 256 steps. The Tx power is increased by default with an adjustable step size, unless the LSK pulses are received from the mobile unit, in which case the Tx power is decreased with an adjustable step size to maintain V_{rec} around the designated 3.3 V. This RFID-based CLPC mechanism has been discussed in more detail in [120].

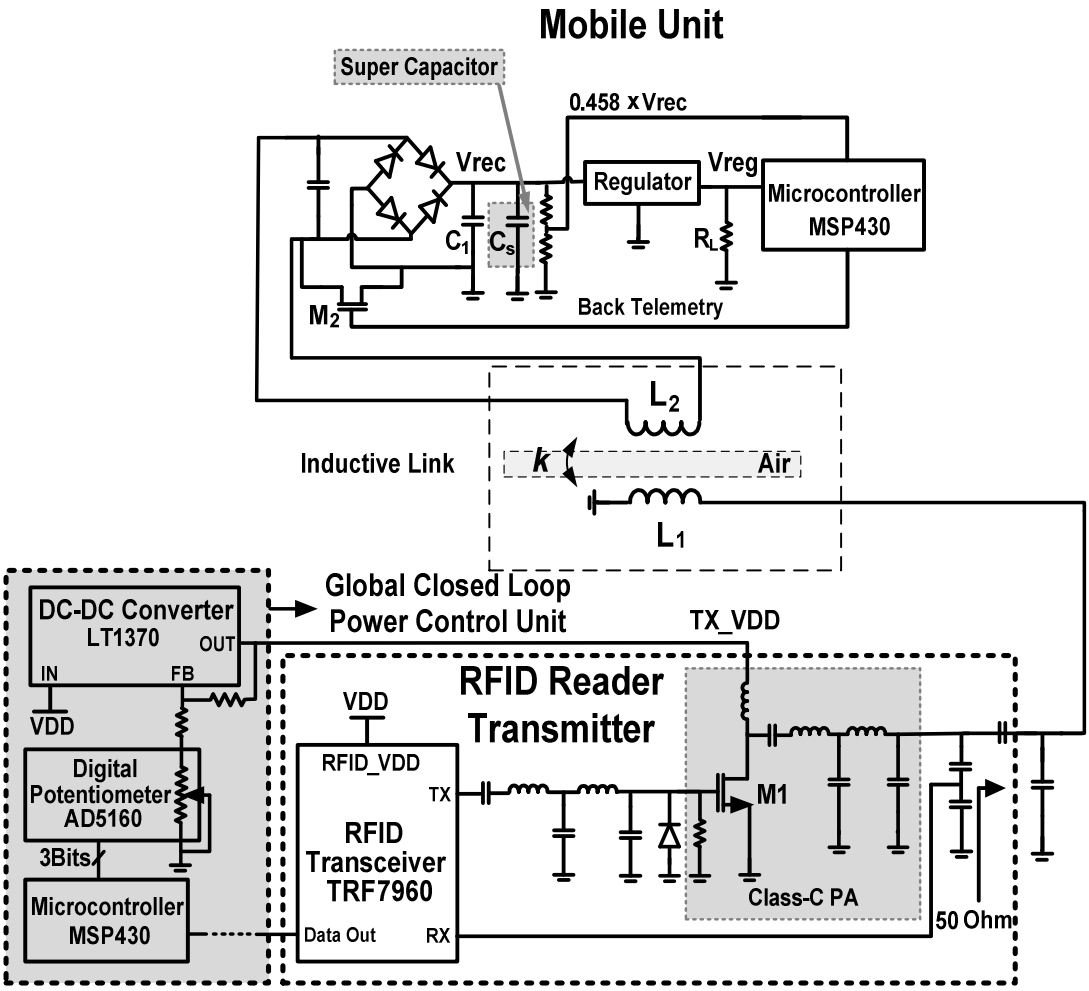

Figure 5.4: Schematic diagram of the RFID-based closed-loop power control mechanism [120].

5.1.3 Magnetic Sensor Array

The magnetic tracer in the mobile unit is a small, disk-shaped permanent magnet (∅5 mm × 1.5 mm) with residual surface flux density of Br_{max} = 14,500 Gauss (K&J, Jamison, PA). It has a mass of 0.6 g, and its main axis is aligned with the Rx coil. A three-axis anisotropic magnetoresistive (AMR) sensor, HMC1043 (Honeywell, Morristown, NJ), is mounted in the center of each hex-PSC to measure variations in the DC magnetic field resulting from animal movement. Sensor outputs are conditioned and digitized before being read by the local MCU through the serial peripheral interface (SPI)

and are delivered to the central PC station via the central MCU. The conditioned sensor outputs are sampled at 100 Hz, resulting in a 10 ms response time. Figure 5.5a shows the magnetic sensors' data flow diagram.

In the proof-of-concept prototype system, a simple algorithm calculates the magnitude of the flux density at the location of each 3-axis magnetic sensor, $|B| = (x^2 + y^2 + z^2)^{0.5}$. The sensor with the highest |B| is considered to be the closest to the magnetic tracer, and if its |B| is above an experimentally determined threshold, B_{th}, the associated hex-PSC is activated. When several sensors have $|B| > B_{th}$, the algorithm chooses the one with the highest |B|. If all sensors have $|B| < B_{th}$, the mobile unit is out of range, (as is the case when the rat is standing on its hind limbs, for example), and the most recently activated PSC is kept active at the highest power level. In this case, the storage capacitor supplies the mobile unit.

Under the threshold method, the boundaries determined by the sensors for the active area of each hex-PSC at 78 mm coupling distance, are shown in Figure 5.5b. This method results in a $0.08r_{o1}$ error between the sensor and PSC boundaries, as shown in Figure 5.5b. The nonlinearity of the magnetic field around the magnetic tracer also causes error in this simplified method when choosing which PSC to activate. In practice, the maximum error at D = 78 mm is ~1 cm, which indicates the need to implement an accurate real-time magnetic localization algorithm [18].

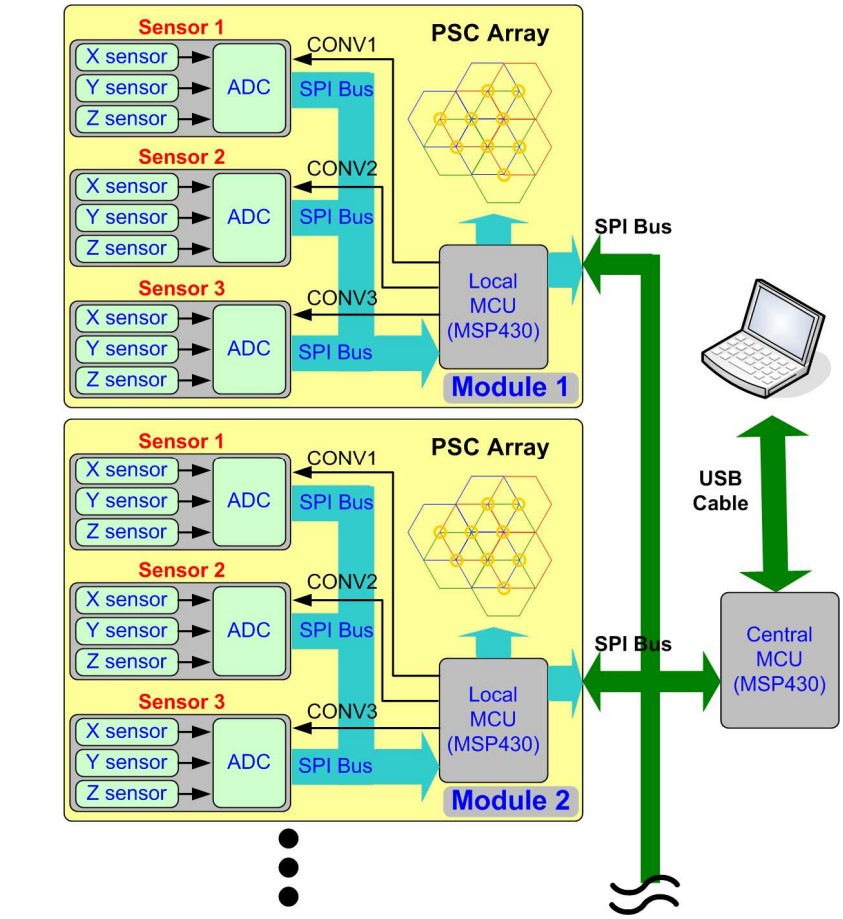

(a)

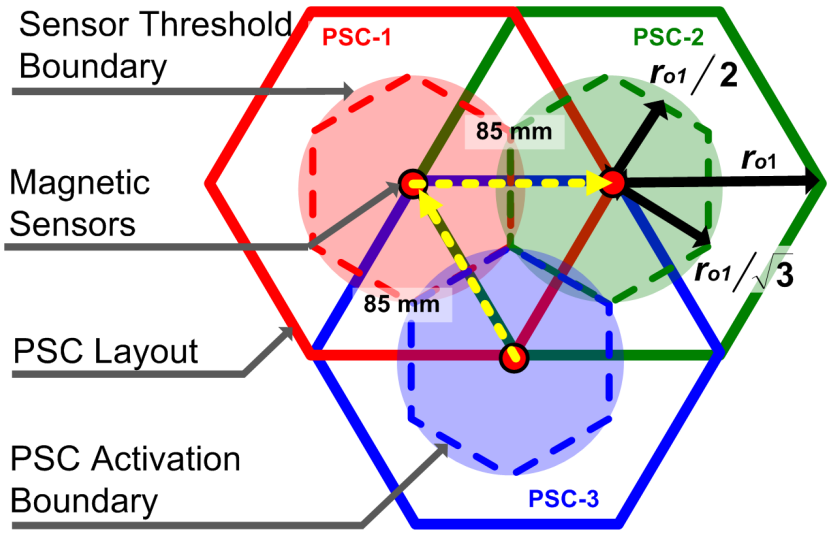

(b)

Figure 5.5: (a) Data flow diagram for the magnetic sensor array in the EnerCage system. (b) Hex-PSC activation boundaries around magnetic sensors, located in the center of each PSC, which were depended on their magnetic field thresholds. The center to center spacing between hex-PSCs/sensors was 85 mm.

5.2 Measurement Results

The measurement results presented in this section were derived from experiments using the proof-of-concept prototype EnerCage system with five controlled PSCs. These experiments are meant to evaluate the homogeneity of the magnetic field generated by the overlapping hex-PSC array and the system response to the mobile unit displacements, while powering it at a designated power level.

5.2.1 PSC Array

In order to demonstrate the homogeneity of the power transfer, four EnerCage unit tiles with 32 complete hexagonal PSCs were assembled, as shown in Figure 5.3. Copper tape with 88 μm thickness was used to connect hex-PSC traces that spanned adjacent unit tiles. In this measurement, a Cartesian-coordinate robotic arm was used to move the Rx coil back and forth across the PSC field at a height of D = 70 mm to generate a raster plot of the received power. The power was measured across a 500 Ω resistor, directly connected to the Rx LC-tank, which was tuned at 13.56 MHz. All PTE measurements were then combined with proper horizontal offset to form the overall PTE distribution across the PSC array, and variations were found to be within ±24% of the averaged PTE. The detailed results are discussed in Chapter 6. Figure 5.6 shows how the received power was maintained at 20 mW at D = 70 mm by the CLPC unit [21]. It is worth noting that the received power fluctuations in this graph are less than 2 mW. The 20 mW power level was chosen in this prototype as a level that was sufficient to power the majority of state-of-the-art neural recording and stimulation devices [127].

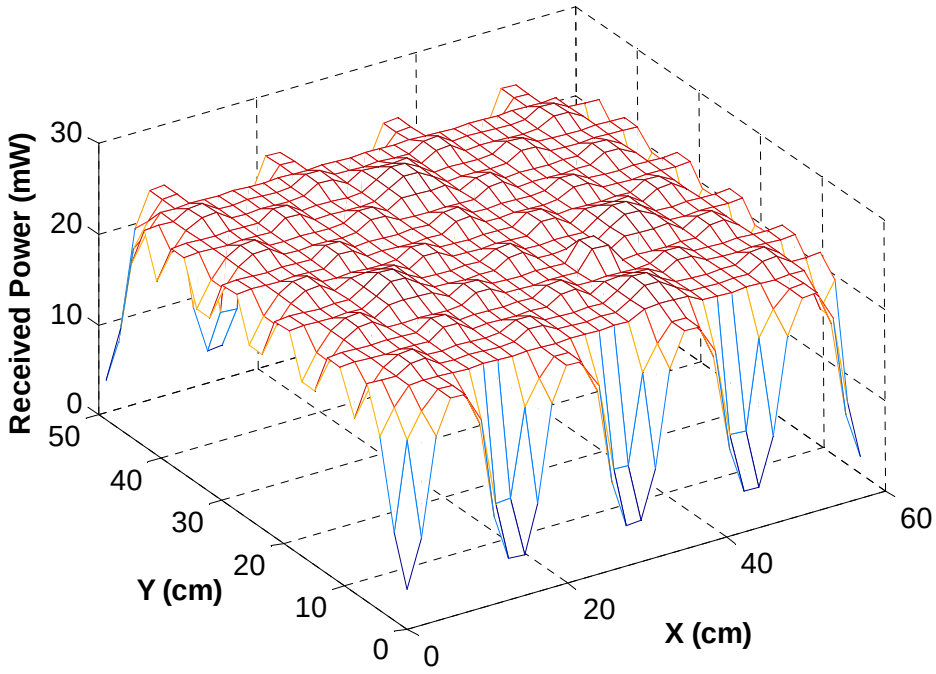

Figure 5.6: Received power of the mobile unit with the CLPC in the air. The distance, *D*, is at 70 mm, and P_{in} = 20 mW.

5.2.2 EnerCage Control Mechanism

A prototype hex-PSC array, shown in Figure 5.7, with five complete PSCs driven by two vertical controller modules, was used to evaluate the functionality of the EnerCage CLPC and magnetic tracking mechanisms. Five magnetic sensors were also placed under the PSC array in the center of each complete PSC. The Rx coil in the mobile unit was embedded in white plastic as part of the headstage shown in Figure 5.2a. Both V_{rec} and V_{reg} in Figure 5.4 were monitored in open-loop (fixed Tx output power) and closed-loop (variable Tx output power) operating conditions. A 500 g saline bag (9 mg/L) used to emulate the animal body was placed between the PSC array and the Rx coil, and the system performance with and without the bag was compared.

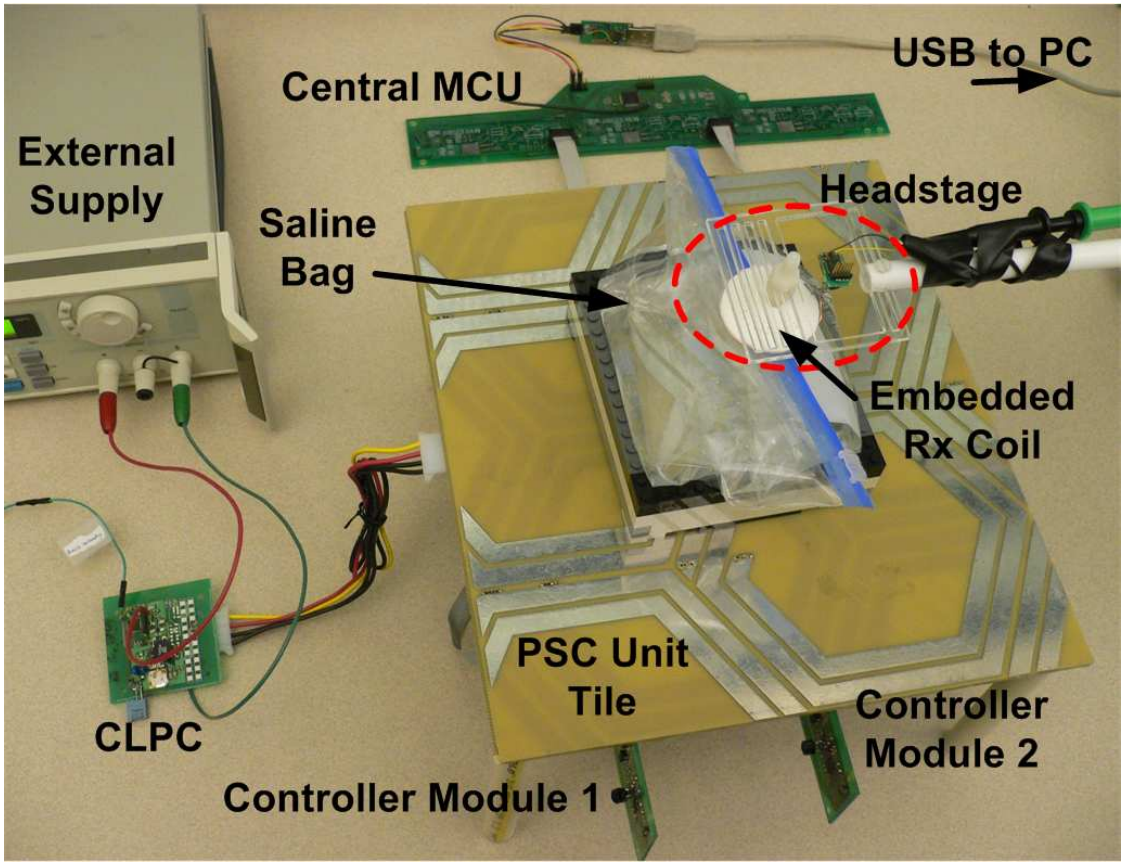

Figure 5.7: Experimental setup with five hex-PSCs controlled by two driver boards in Figure 5.2b. The mobile unit with its Rx coil embedded in plastic was held above a saline bag, representing the animal body, by a robotic arm.

Figure 5.8 compares the variations in the PA supply voltage (Tx_V_{DD} in Figure 5.4) as well as V_{rec} and V_{reg} on the mobile unit under open-loop (Figure 5.8a) and closed-loop (Figure 5.8b) conditions. These conditions are for emulating the animal subject's movements resulting in lateral misalignment. In this experiment, the mobile unit was moved in a horizontal plane at a nominal height of D = 78 mm from the center of PSC-3 to the center of PSC-1, and from there to the center of PSC-2, as shown by the dashed line in Figure 5.5b. Since the center to center spacing between hex-PSCs was 85 mm, Figure 5.8 shows the voltage variations caused by moving the headstage a total distance of 17 cm. In Figure 5.8a, Tx_V_{DD} was fixed at 8.5 V, which provided ~1 W of Tx output

power as well as the power consumed by the controller. The peaks of V_{rec}, where the Rx power is the highest, are obviously at the center of each PSC, where there is no horizontal misalignment. The valleys of V_{rec} are at the edges of the PSC active areas, shown in Figure 5.5b, where the magnetic tracking switches the active PSC (vertical dashed lines). In the open-loop measurement, since the Tx is set to constantly operate under the worst-case scenario, a large percentage of the Rx power was dissipated in the regulator, and the overall PTE was quite low. When the saline bag was moved under the mobile unit, V_{rec} dropped slightly by 9.6% because of the reduction in the Q of the active PSCs [5].

In Figure 5.8b, the CLPC unit automatically adjusted Tx_V_{DD} for V_{rec} to be slightly higher than V_{reg} regardless of the Rx coil horizontal misalignment. The peaks and valleys of Tx_V_{DD} in Figure 5.8b are the opposite of those of V_{rec} in Figure 5.8a. While using the closed-loop mechanism, considerably less power was transmitted in order to deliver the same amount of power to the mobile unit, leading to higher overall PTE. This is quite desirable because higher PTE means less heat dissipation on both Tx and Rx sides, less tissue exposure to the magnetic field, and less temperature elevation in the cage. Switching from one PSC to another at the PSC boundaries often creates sharp voltage transitions in the CLPC and sensors, which can be avoided by proper filtering and signal process of the control algorithm.

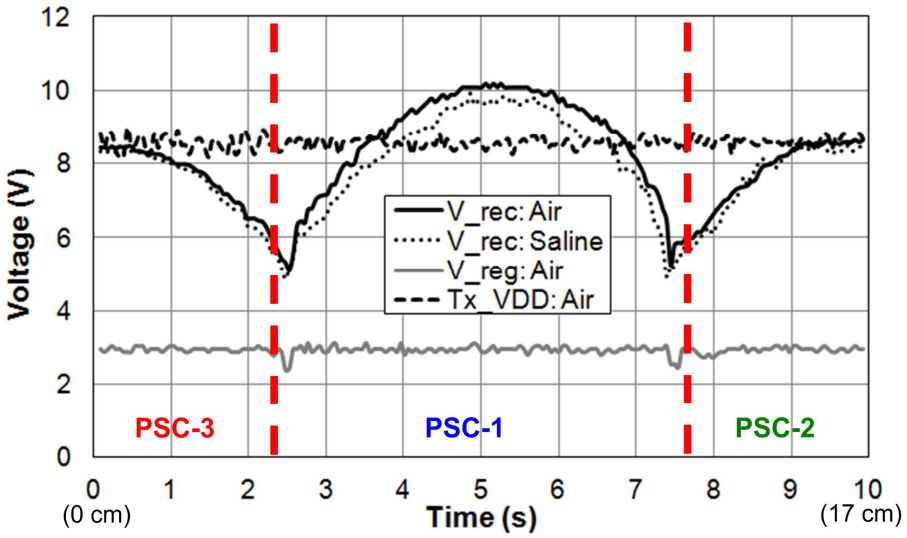

(a)

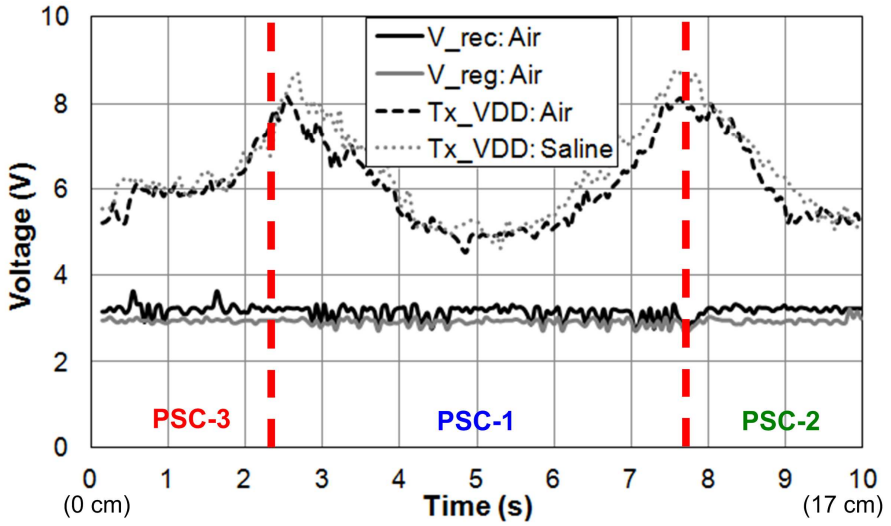

(b)

Figure 5.8: Moving the mobile unit by 17 cm over three hex-PSC in 10 s at a coupling distance of *D* = 78 mm: (a) Open-loop, (b) closed-loop. Vertical dashed lines indicate when the magnetic tracking mechanism automatically switches the active PSC.

A measurement of variations in D is performed to emulate the vertical displacements of the mobile unit. In Figure 5.9a and Figure 5.9b, D has been increased from 7.0 cm to 12.0 cm above PSC-2 under open- and closed-loop conditions, respectively. For the open-loop measurement, Tx_V_{DD} is again set to handle the worst-case condition (D = 12.0 cm), and V_{rec} was again much higher than needed at shorter

distances, resulting in considerable power dissipation in the CLPC and mobile unit. On the other hand, the closed-loop operation adjusted the Tx power to be just enough to achieve the desired V_{reg} = 3.0 V.

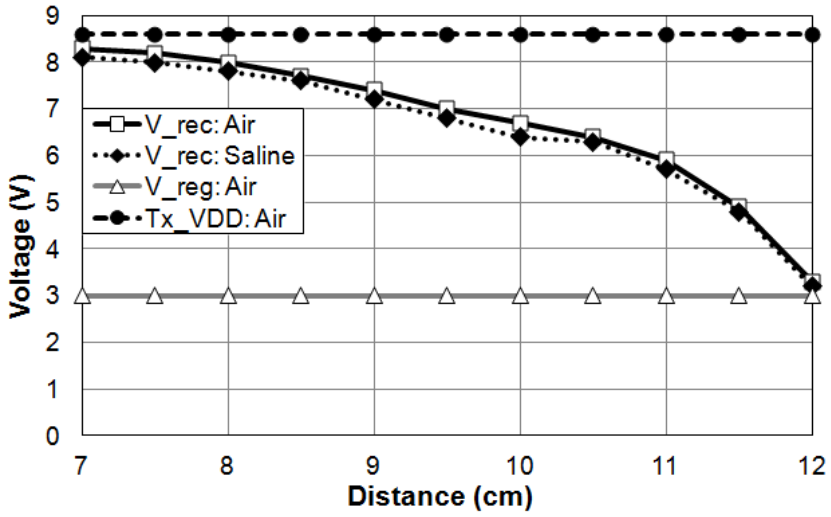

(a)

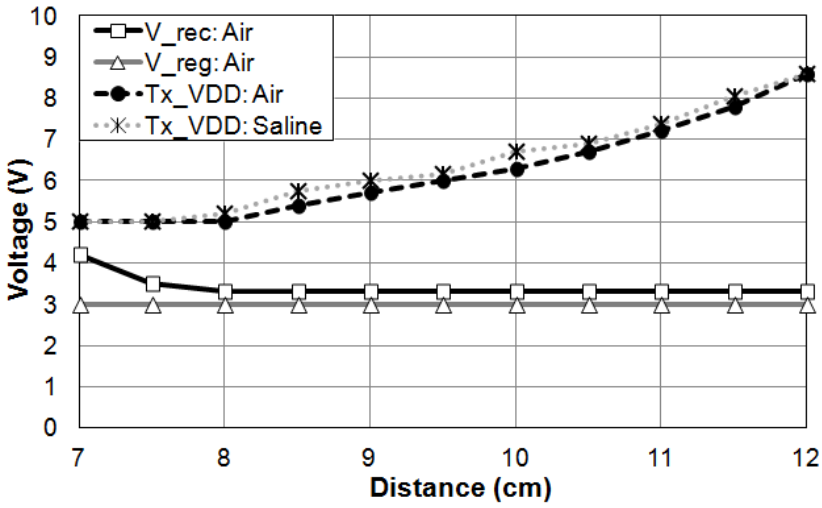

(b)

Figure 5.9: Changing the coupling distance, *D*, at the center of PSC-2 in Figure 5.5b from 7.0 cm to 12.0 cm in (a) open-loop, and (b) closed-loop conditions.

The animal subject may also tilt its head, and this tilt could be combined with a lateral misalignment. In the next experiment, the Rx coil was manually rotated above the center of PSC-2 in Figure 5.5b at D = 78 mm to emulate the tilting misalignment. The measurement results for open- and closed-loop operating conditions are shown in Figure

5.10a and Figure 5.10b, respectively. When the tilting angle is > 60°, the mobile unit cannot be powered up, because V_{reg} falls below 3.0 V. As with previous tests, the closed-loop mechanism keeps V_{rec} constant in Figure 5.10b despite coupling variations, as compared to the open-loop condition in Figure 5.10a.

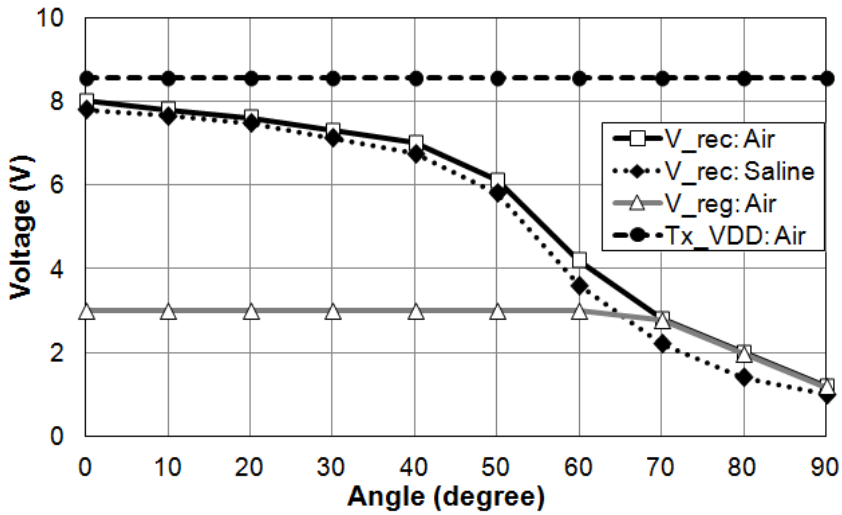

(a)

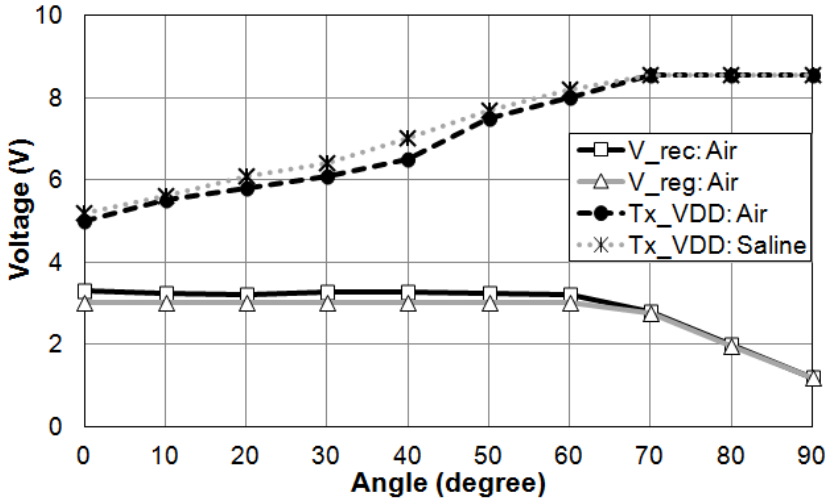

(b)

Figure 5.10: Rotating the mobile unit at *D* = 78 mm above the center of PSC-2 in Figure 5.5b: (a) Open-loop, (b) closed-loop.

5.2.3 Compensation of the Rx Coil Movement

It was shown in Figure 5.10 that one PSC cannot energize the mobile unit when the tilting angle of the Rx coil is > 60º. One possible solution is to simultaneously activate a

pair of adjacent PSCs with out-of-phase excitation signals to create a horizontal field between them in a way that sufficient flux passes through the Rx coil [22]. Two-PSC out-of-phase excitation, along with the storage super-capacitor C_s, shown in Figure 5.4, can solve the problems caused by sharp tilting misalignments as long as they last less than ~30 s, which is often the case. A similar situation may result from the animal rearing on its hind limbs, thereby increasing D beyond the designated 12.0 cm maximum height of the mobile unit. More detailed discussion about these conditions can be found in Chapter 6 [35].

5.2.4 Maximum Permissible Exposure to Magnetic Field

According to the IEEE standard, the maximum permissible exposure (MPE) to magnetic fields (H) is $16.3/f_c$ (A/m), where f_c is in MHz [59]. Hence, at 13.56 MHz, the MPE is 1.2 A/m. Power density in free space can be found from

$$P(\text{mW}/\text{cm}^2) = H^2 \times Z_0 / 10 , \quad (5.1)$$

where $Z_0 = E/H = (\mu_0/\varepsilon_0)^{0.5}$ is the impedance of free space, or approximately 377 Ω. Using (5.1), the equivalent maximum power density at 13.56 MHz would be 54.3 mW/cm^2 [59].

When the PA delivers 1 W to the active PSC on the Tx side, the level of magnetic field exposure at the center of the PSC passes the MPE level at a height of 3.2 cm above the surface, according to HFSS simulation results. Since the EnerCage system operates at a relatively low frequency via near-field interaction between the active Tx PSC and the Rx coil, the area in which the magnetic field strength is above the MPE level is confined to a small space above the active PSC with a peak at the 3.2 cm distance, as shown in Figure 5.11. Therefore, using the EnerCage system in the lab is unlikely to impose any

risk of exposure to the researchers. However, at least part of the animal body, particularly the legs, will be inevitably located within this space. At this time, it is not clear whether this condition will have any impact on the results of the electrophysiology experiments.

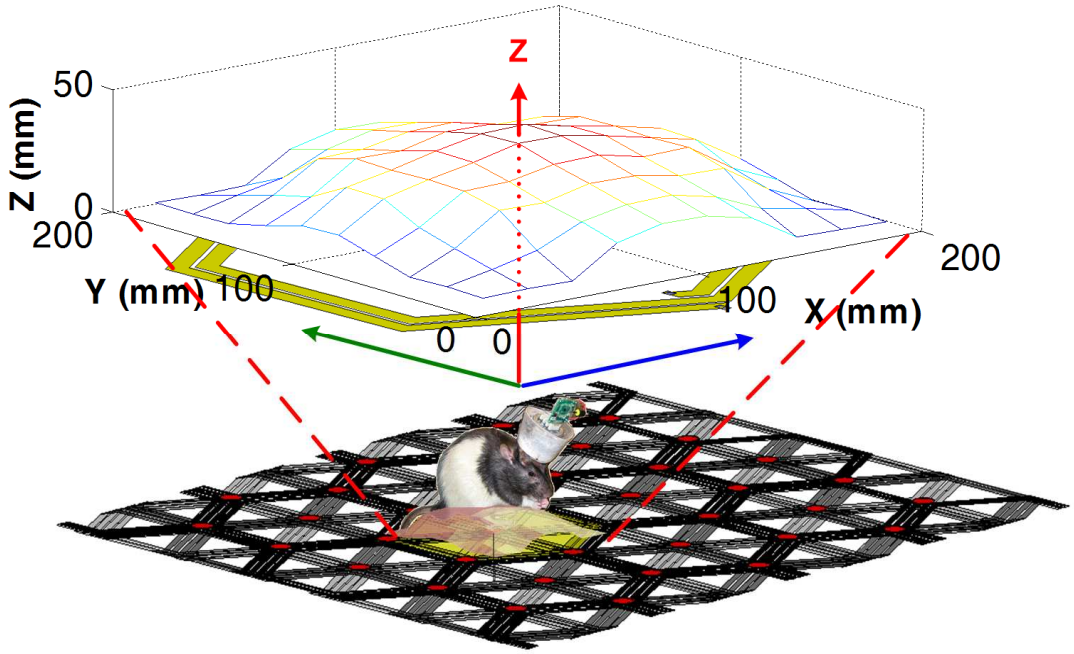

Figure 5.11: The simulated maximum permissible exposure (MPE) boundary of four PSC arrays operating at 13.56 MHz with 1W input power. The highest coupling distance that meets MPE is 3.2 cm at the center of each PSC.

5.3 Conclusions

The Enercage system is a smart experimental arena for long-term electrophysiology experiments. This system consists of a scalable array of overlapping hexagonal PSCs, arranged in such a way that they can cover any arbitrarily shaped experimental field. The EnerCage system allows researchers to create a natural environment for freely behaving small animal subjects for an unlimited amount of time. Three key features of the EnerCage system are: 1. Inductive powering through a scalable array of modular overlapping PSCs that are activated one or two at a time. Each individual hex-PSC has

been optimized to account for parasitics caused by overlapping and adjacent PSCs, based on worst-case misalignment conditions, to achieve a smooth coupling distribution across the arena. 2. Accurate non-line-of-sight 3D tracking of a mobile unit attached to or implanted in the animal body via an array of magnetic sensors. 3. Closed-loop power control, which significantly improves the overall PTE and limits heat dissipation and exposure to the magnetic field.

In this chapter, the EnerCage system design provides the initial concept for the long-term animal experiment. One of the key points of this system is the PSC array design, which affects the homogeneity of the PTE distribution. In the next chapter, this issue is addressed and the new models and optimization procedure for of the optimal PSC array are introduced.

CHAPTER VI

. OPTIMIZATION FOR OVERLAPPING PLANAR SPRIAL COIL ARRAY

The content of this chapter includes a geometrical design procedure and a modular architecture for a PSC array that can create a homogenous magnetic field across any large planar surface with an arbitrary size for efficient wireless power transmission to either stationary or mobile targets. In the design example for EnerCage, shown in Figure 6.1, a 3-layer modular array of hexagonal overlapping PSCs tiles an arbitrary-sized wireless powering arena to couple onto a circular wire-wound Rx coil that is embedded in the headstage of an awake freely behaving rat to indefinitely power a wireless neural recording system that was described in [127]. Parasitic effects of the overlapping PSCs and their impedance matching to the driving power amplifier are key aspects of a design that can maximize the power delivered to the Rx coil in the worst-case conditions.

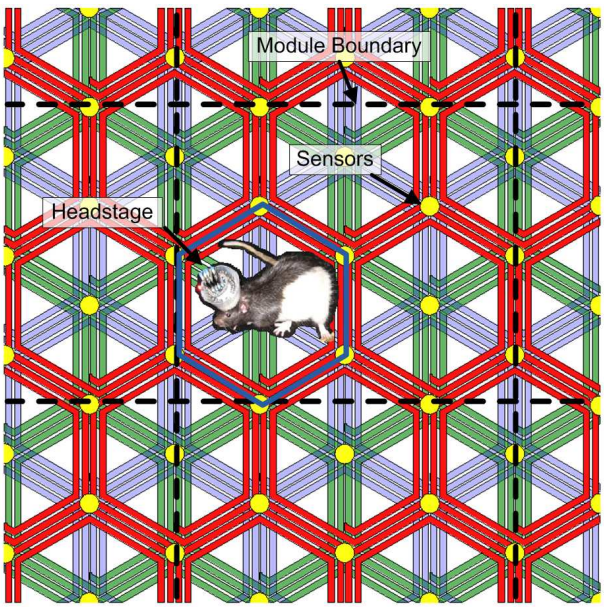

Figure 6.1: Top view rendering of an overlapping planar hexagonal PSC array to generate a homogeneous magnetic field for wireless power transmission to freely behaving animals .

In addition to the overlapping PSC, the EnerCage system is equipped with an array of 3-axial magnetic sensor modules (yellow dots at the center of each PSC in Figure1), which can track in real time the 3-D position and orientation of a small magnetic tracer embedded in the headstage [18]. The power carrier frequency, f_c, is fixed at 13.56 MHz in compliance with the industrial scientific medical (ISM) band [60]. In the next section, the basic theoretical PSC equations and design procedure will be reviewed, and the detailed equations can be referred to Chapter 3. Section 6.2 presents the measurement and analysis of the results of the coupling efficiency, followed by the concluding remarks.

6.1 Coil Design and Optimization

A key aspect of the optimization procedure is that instead of maximizing the PTE when the Tx and Rx coils are perfectly aligned, *i.e.* in the best-case scenario, the designer should try to maximize the PTE in the worst-case conditions when the Tx PSC has the lowest quality factor, Q, and the Rx coil is at maximum lateral misalignment. This will minimize the coupling variations and create a space with smooth coupling and homogeneous PTE distribution.

6.1.1 Unit tile Module for the Array of Overlapping PSCs

A number of factors should be considered in the design of the primary PSC array such as min-PTE with respect to the Rx coil misalignments, coil Q-factors, power carrier frequency (f_c = 13.56 MHz), manufacturability, and cost. The PSCs has to be designed for batch-fabrication in the form of modular units of multilayer PCB that tile the experimental arena, as shown in Figure 6.1. Size limitations in the commercially available PCB fabrication processes define the maximum size of the unit tiles (modules), which should be repeated to cover a designated area at the bottom of a charging mat, an

animal cage, or a maze. Hence, densely packed hexagonal PSC (hex-PSC) design has been adopted because of its superior area coverage over its square-shaped counterpart [107]. Moreover, the hex-PSC, shown in Figure 6.2, needs only three conductive layers as opposed to four layers needed in the square-shaped PSCs for the same level of coverage. The fourth layer can then be used for interconnects between the hex-PSCs and their driving circuits. When the Rx coil is laterally misaligned beyond a maximum level, γ_{max}, the active PSC turns off, and one of the overlapping PSCs that has a better coupling with the Rx coil will be activated.

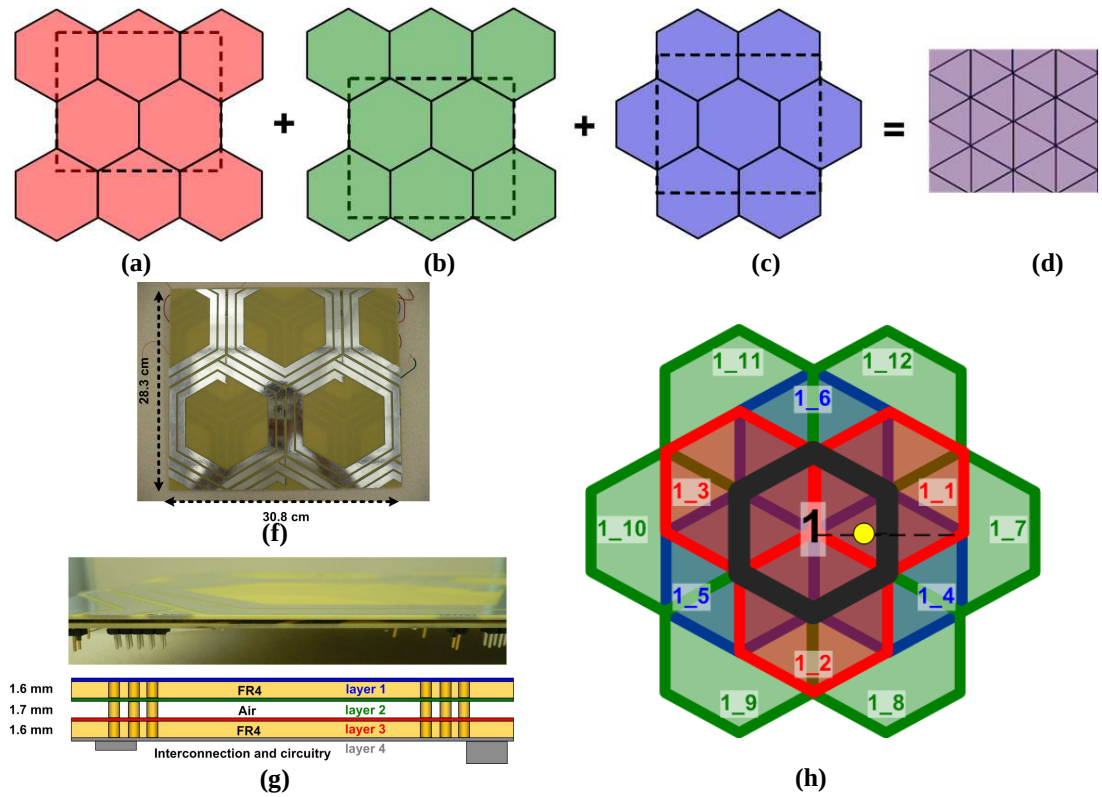

Figure 6.2: Overlapping hex-PSCs in (a) layer 1, (b) layer 2, and (c) layer 3, which create a (d) rectangular unit tile (module) when all three layers are properly aligned. (e) Implementation of the 30.8 × 28.3 cm^2 hex-PSC module on two 2-layer PCBs, made of 1-oz copper on 1.6 mm FR4 substrate, based on the optimal geometries given in Table II. (f) Cross section of the 2-layer PCBs forming the three overlapping PSC layers plus an additional layer for electronic components and interconnects. (g) A different view of the overlapping PSCs, which is color-coded to better demonstrate the relative positions of the PSCs in each layer. Every hex-PSC in this design, such as the gray one in the center, has been surrounded by six PSCs in the same layer (green-2) and overlapped by six other PSCs in the other two layers (red-1 and blue-3). Worst-case horizontal misalignment in this configuration occurs at $\gamma_{max} = r/\sqrt{3}$, which is indicated by a yellow dot.

The EnerCage unit tile has been designed for PCB manufacturing, which is often rectangular shaped. Figs. 6.2a (layer 1), 2b (layer 2), and 2c (layer 3) show how three hex-PSC layers are overlapped and carefully aligned to create a repeatable pattern for a rectangular module, shown in Figure 6.2d, which can cover any arbitrary arena. In the proof-of-concept module, shown in Figs. 6.2e and 6.2f, the hex-PSC patterns are fabricated on two 2-layer PCBs made of FR4 substrate with 1-oz copper (FR4 dielectric thickness: t_s = 1.6 mm, copper thickness: t_0 = 35 µm). The 2-layer PCBs were stacked with 1.7 mm spacing, t_{air}, (close to the thickness of each PCB substrate) to construct the unit tile. Therefore, as shown in Figure 6.2f, the dielectric material under layers 1 and 3 is FR4, while the one under layer-2 is the air.

Figure 6.2g depicts the relative positions of the overlapping hex-PSCs in different layers. Every hex-PSC in this design, *e.g.* the central gray PSC in layer 2 (L1), has overlapping with six other PSCs (L1_1 to L1_3 in layer 1 and L1_4 to L1_6 in layer 3), and surrounded by six other PSCs (L1_7 to L1_12) in the same layer. This pattern ensures the continuity and strength of the magnetic field regardless of the horizontal position of the Rx coil by limiting the horizontal misalignment in any direction to $1/\sqrt{3}$ = 0.577 of the hex-PSC radius (the yellow dot in Figure 6.2g).

6.1.2 Modeling of the Primary PSC Array

Modeling of an individual PSC in terms of self-inductance, parasitic capacitance, and parasitic resistance has been covered in Chapter 3 [4]-[7]. The model for the primary PSC array is different from the individual PSC, because each primary PSC is surrounded and overlapped by other PSCs. The driver circuitry should be designed such that when it activates the PSC closest to the Rx coil, all other PSCs are open circuit. Although the

opened hex-PSCs do not load the resonance circuit the way a coupled closed conductive loop does, the parasitic mutual inductance, capacitance, and resistance between the metal paths of the neighboring hex-PSCs affect the *Q* of the activated hex-PSC. Furthermore, different overlapping hex-PSC layers experience different parasitic effects because of their particular 3D arrangement, shown in Figure 6.2f. The optimal design of the PSC array should maximize the PTE in the worst-case conditions.

Figure 6.2g shows the worst-case condition for an active hex-PSC, which is on layer-2, sandwiched between six PSCs in layer-1 (L_{1_1} to L_{1_3}) and layer-3 (L_{1_4} to L_{1_6}), and surrounded by six adjacent PSCs in layer-2 (L_{1_7} to L_{1_12}). The equivalent circuit model for this PSC, including key parasitic effects, is shown in Figure 6.3. L_i and R_{Si} are the inductance and series parasitic resistance of each hex-PSC, respectively, and C_{Pi} and R_{Pi} are the parallel parasitic capacitance and resistance (due to dielectric material leakage) between metal traces within each PSC, respectively. C_{S1} is used for the resonant carrier frequency. Even though every two hex-PSCs on the array have some mutual coupling, for the sake of simplicity, the model is only considered for mutual couplings in two conditions: (1) overlapping hex-PSC pairs and (2) adjacent hex-PSC pairs, shown in Figs 6.4a and 6.4b, respectively. In Figure 6.3 equivalent circuit, the interactions between every hex-PSC pair that fit in one of these conditions with the central hex-PSC in Figure 6.2g has been expressed in terms of mutual inductance (M_{i,i_j}), mutual capacitance (C_{Mi,i_j}), and mutual resistance, (R_{Mi,i_j}). The mutual effects of the non-adjacent or overlapping PSCs such as L_{1_1} and L_{1_10} in Figure 6.2g can be neglected because both direct and indirect couplings for these PSCs are very small compared to the others [102].

All hex-PSC mutual inductances were calculated from (1) and (2) by considering the

PSC pairs' lateral misalignments, γ_{i_j}, in each of the two conditions in Figure 6.4, and the vertical separation between every two layers in Figure 6.2f. Using the spacing between every two adjacent metal traces, S_{adj}, and the hex-PSC radius, $r_{o1} = d_{o1}/2$, the mutual inductance of the overlapping PSC pairs in Figure 4a (M_{ov}) and adjacent PSC pairs in Figure 6.4b (M_{adj}) can be found by substituting $\gamma_{ov} = r_{o1} + S_{adj}/\sqrt{3}$ and $\gamma_{adj} = 2\sqrt{3}r_{o1} + S_{adj}$ in (2), respectively.

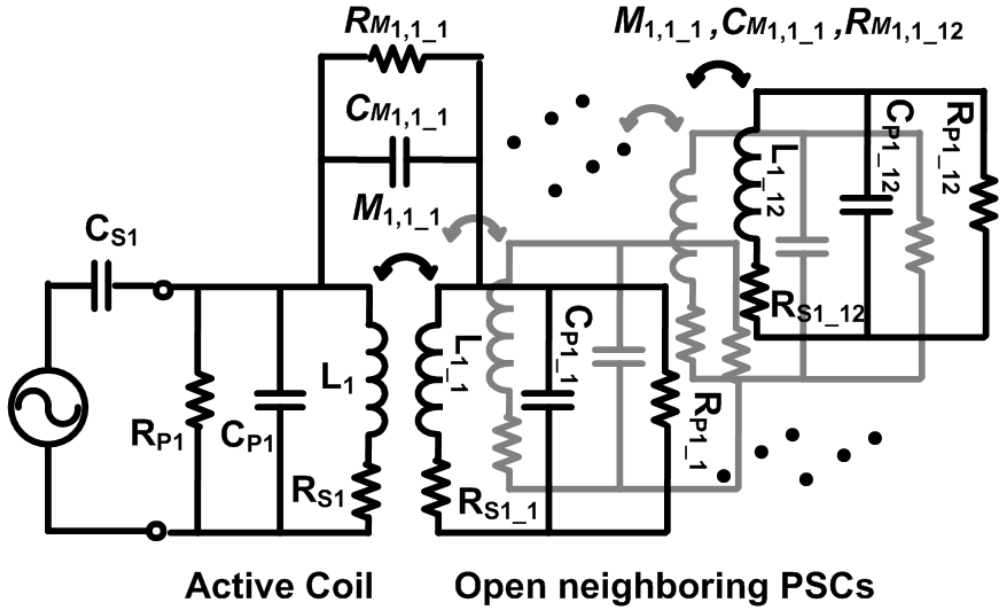

Figure 6.3: Equivalent circuit model of each hex-PSC in the primary coil array, including key mutual couplings and parasitic components.

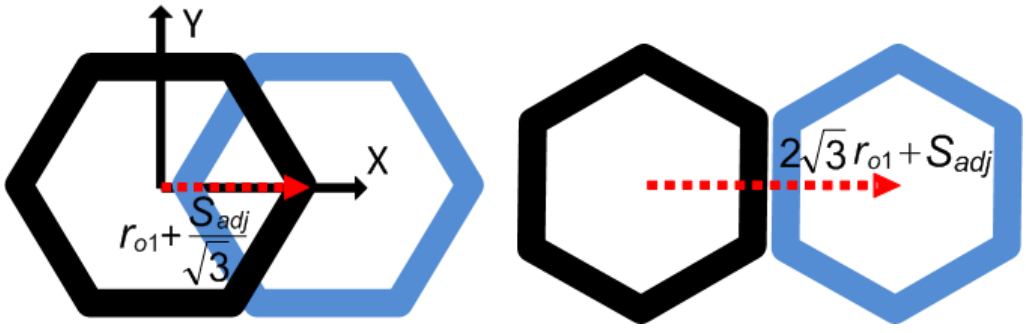

Figure 6.4: Two types of mutual interference between hex-PSCs: (a) overlapping hex-PSCs in different layers, (b) adjacent hex-PSCs in the same layer.

The mutual capacitance between overlapping PSC pairs can be found from parallel plate capacitance model,

$$C_{ov} = \varepsilon_0 \varepsilon_{r\_eff} \frac{A_{ov}}{2t_s} \ , \tag{6.1}$$

where ε_0 is the vacuum permittivity, t_s is the separation between two layers, A_{ov} is the PSC overlapping area, and ε_{r_eff} is the effective dielectric constant between the two conductive plates [112]. The mutual resistance between overlapping PSC pairs, R_{ov}, originates from the dielectric loss, which in turn relates to C_{ov} and the loss tangent, $tan(\delta)$, of the conducting and insulating materials [85]. C_{adj} and R_{adj}, the mutual capacitance and resistance between adjacent hex-PSC pairs, are calculated using models proposed in [85] and [109], with the hex-PSC side length of r_{o1} and spacing of S_{adj}. The complete hex-PSC model in Figure 6.3, including parasitic effects, leads to three 13 × 13 matrixes for M, C_M, and R_M, the details of which have been presented and calculated in the Appendix B. These effects can be used for the coil model.

It should be noted that the eddy current induced within overlapping hex-PSCs, adjacent hex-PSCs, and the overlapping circuitry on layer-4 is not been considered in this model. For the overlapping PSC array, the arrangement of the direct and indirect coupling metal traces from the same layer (layer-2) and different layers (layer-1 and -3) is very complicated, so eddy current effects were omitted for the sake of simplicity. Furthermore, the circuitry pattern of layer-4, which includes sensor circuits, power amplifiers, control circuits, power lines and the connectors, is difficult to be standardized in the calculation model. In order to have an accurate optimal geometry, a commercial electromagnetic field solver, which includes the eddy current effect, overlapping connection traces, will be involved in the design procedure.

6.1.3 Design Considerations for the Rx Coil

In the wireless powering design example, EnerCage, the Rx coil is a wire-wound circular (WWC) type, mounted on the animal headstage [70], [127]. Both diameter (d_{o2}) and weight ($W_{\max}$) of the Rx coil are limited in this application and should also be considered in the design. These two parameters are related as follows,

$$r_{wire} = \left(\frac{4W_{\max}}{\pi^2 \rho \cdot n_2 \cdot d_{o2}} \right)^{1/2}, \tag{6.2}$$

where ρ is the density of the conducting material (ρ = 8.96 g/cm^3 for copper), r_{wire} is the wire radius, n_2 is the number of turns, and d_{o2} is the Rx coil outer diameter. The weight of the insulating material around the wire strand is ignored. d_{o2} = 40 mm is considered from [105] and limited $W_{\max}$ to 0.7 g. Moreover, the Rx coil was embedded in a plastic molding material, Smooth-Cast 300 (Smooth-On, Easton, PA), as part of the headstage for mechanical stability, but this material lowered the Q of the Rx coil by 15% compared to air.

6.1.4 Design Considerations for the EnerCage System

The coupling distance between the overlapping hex-PSC array, which constitute the primary coil, and the secondary Rx coil was considered D = 78 mm on average based on the nominal height of mature Long-Evans rats [105], [128]. This distance should be changed if the cage is to be used for species with significantly different sizes, such as mice, or for other applications. The carrier frequency was chosen f_c = 13.56 MHz in the ISM-band to comply with the HF-RFID standard and achieve high Q from the coils, leading to higher PTE [7]. Moreover, higher f_c results in lower number of turns in the hex-PSCs, which in turn simplifies the geometrical design and modular assembly of the hex-

PSC array [129].

Table 6.1 summarizes the design constrains due to application and fabrication process that were considered in our example. The optimization procedure should consider not only the worst-case in regards to the hex-PSC model (see section II.B) but also the worst-case Tx-Rx coupling due to the lateral misalignment, which is $\gamma_{max} = (r_{o1} + S_{adj}/\sqrt{3})/\sqrt{3} \approx 0.58 r_{o1}$ according to the overlapping hex-PSC pattern in Figure 2g. When $\gamma_{max} > 0.58 r_{o1}$, the EnerCage control system switches the active PSC to one of the overlapping PSCs (L_{1_1} to L_{1_6}) that is in the best position to resume powering the Rx coil (*i.e.* L_{1_1} or L_{1_4} in this case). The goal is to minimize the coupling variations as the animal subject, with the Rx coil on its head or in its body, moves across the hex-PSC array. It should be noted that to avoid further complexity, angular misalignments were not considered in this optimization, but simulated, measured, and remedied in Sections 6.3.

Table 6.1. DESIGN CONSTRAINS DUE TO APPLICATION AND FABRICATION PROCESS

Parameter	Symbol	Design Value
Rx coil outer diameter (max)	d_{o2}	40 mm
Maximum weight of the Rx coil	$W_{\max}$	0.7 g
Coils' relative distance (nominal)	D	78 mm
Power carrier frequency	f	13.56 MHz
Rx coil nominal loading	R_L	500 Ω
Lateral misalignment (max)	γ_{max}	$(r_{o1} + S_{adj}/\sqrt{3})/\sqrt{3}$
PSC conductor thickness (Tx)	t_c	35 μm*
Conducting material properties (Cu)	ρ, μ_r	~17 nΩm, ~1
Spacing between peak-to-peak PSCs	S_{adj}	4 mm
PCB substrate thickness (FR4)	t_s	1.6 mm*
Separation between two PCBs	t_{air}	1.7 mm
Substrate dielectric constant (FR4)	ε_{rs}	4.4
Substrate dielectric loss tangent (FR4)	$tan(\delta)$	0.02
Plastic mold dielectric constant (Rx)	ε_{rp}	3.2

*1 oz copper on 2-layer FR4 printed circuit board.

The model for the overlapping active PSCs with parasitic effects, which was described in Section 6.2.2, was used for the primary coil, and the mutual coupling was simplified to only two coils, *i.e.* between the active PSC and the Rx coil. In other words,

the mutual coupling between the open-circuit PSCs and the Rx coil were ignored. The iterative design procedure in [5] was adopted to maximize the worst-case PTE, starting from the design constraints in Table 6.1 as the initial conditions, and ending with the optimal coil geometries. Although this equivalent circuit model gives the user quick design guide to save the design schedule, some of the parasitic effects are not included as discussed. Hence, a field solver, HFSS (Ansoft, Pittsburgh, PA), was then used to in the design procedure to verify and fine tune the values suggested by the theoretical models. The simulation model includes the all possible eddy current effects from the overlapping PSCs of layer 1 to 3 and adjacent PSCs of layer 2. However, the real pattern of layer 4 includes driving circuitries, sensor modules, central control units, and the connections [20], [21], which are not easy to be justified in the model. Hence, layer 4 metal plane is simulated using parallel conductive (copper) strips, 19.2 mm in width and 20.8 mm in spacing, covering 48% of the total tile area. This is the same percent coverage as the layer-4 circuitry in the actual fabricated PCB [21]. Table 6.2 summarizes the geometries of the resulting coils with 500 Ω Rx coil loading and γ_{max} = 49.1 mm. With these dimensions, the hex-PSC module, shown in Figure 2, was sized 30.8 × 28.3 cm^2, and implemented on a pair of carefully spaced 2-layer 1.6 mm-thick FR4 PCBs. The Rx coil, optimal wire radius, r_{wire} = 0.33 mm, lead to the choice of the closest standard magnet wire, AWG 22 (r_{wire} = 0.32 mm).

Table 6.2. SPECIFICATIONS OF THE ENERCAGE COILS OPTIMIZED AT 13.56 MHZ

Parameter	Tx PSC (primary)	Rx coil (seconary)
Shape	Hexagonal PSC	Wire-wound
Outer diameter (mm)	168	40
Edge length (mm)	84	20 (Radius)
Number of turns	2	2
Metal trace cross section	35 μm × 10 mm	r_{wire} = 0.32 mm
Metal trace spaicng (mm)	3	~0.2
PSC inductance (μH)	0.88	0.38
Weight of copper (g)	3.6	0.7
Quality factor with/without layer-4	122 / 107	138
Max/Ave/Min simulated coupling coefficient (k)*	0.022/0.021/0.018**	
Max/Ave/Min calculated PTE (%)	43.1/38.5/28.8	
Max/Ave/Min simulated PTE without layer-4 (%)	41.2/35.6/27.0	
Max/Ave/Min simulated PTE with layer-4 (%)	38.3/33.9/24.6	
Max/Ave/Min measured PTE (%)	31.6/27.5/19.6	

*Coupling distance, D = 78 mm

**Maximum misalignment for the worst-case PTE: γ_{max} = 49.1 mm

6.2 Measurement Results

In order to measure the 3D distribution of the PTE across the hex-PSC array, four hex-PSC modules in Figure 2e were joint together (2×2) by soldering the edges of the PSCs with an overlaying layer of copper tape (thickness = 88 μm) to cover a 61.6 × 56.6 cm^2 area, as shown in Figure 5a. Excluding the incomplete hex-PSCs across the edges, this arrangement results in an array with 32 complete overlapping hex-PSCs that can energize a 2003.7 cm^2 experimental arena.

Figure 6.5b shows the block diagram of the measurement setup. A Cartesian robotic system (Velmex, Bloomfield, NY), controlled by a PC, was responsible for moving the Rx module in the 3D space above the hex-PSC array. The Rx module is connected to a 500 Ω load. A digital oscilloscope (MSO4034B, Tektronix, Beaverton, OR) measured the peak-to-peak voltage across the LC-tank and delivered the results to the PC to calculate the received power. The PSC array was driven by custom made control modules that included a microcontroller (MCU), RFID reader, and power

amplifiers (PA). The details of the control modules have been described in Chapter 5. In one set of experiments, the Rx-module also included a back telemetry switch that could establish a closed-loop power control (CLPC) mechanism, as in [120].

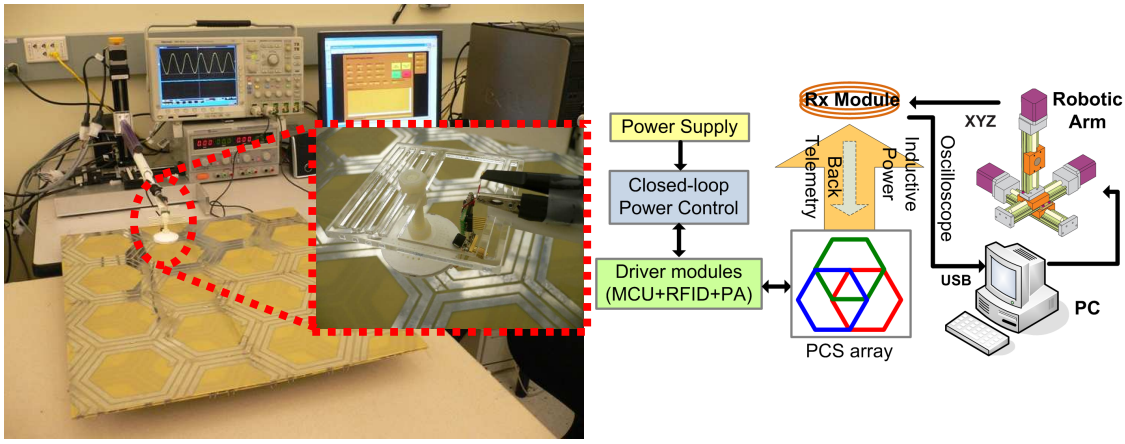

(a) **(b)**

Figure 6.5: (a) Measurement setup made up of 4 hex-PSC unit tiles of Figure 6.2e, a robotic arm to sweep the Rx module in 3D space, driver circuits, a digital scope, and a PC with LabVIEW. (b) Block diagram of the measurement setup.

6.2.1 Hex-PSC and Rx Coil Quality Factors

Figure 6.6 compares the calculation, simulation (with and without layer 4), and measurement results for worst-case Q_T of the overlapping and non-overlapping (*i.e.* individual) hex-PSCs on the Tx side. It can be seen that the optimization procedure in section II has maximized the Q_T of the hex-PSC slightly below the power carrier frequency of 13.56 MHz. This is because the PTE depends on Q_T, Q_R, and k, a combination of which needs to be maximized at f_c = 13.56 MHz. The 12 mutual coupling PSCs, shown in Figure 6.2g, have resulted in 33.7% reduction in Q_T from 184 to 122 (in simulation) compared to an individual hex-PSC with the same geometry. Although the simulation model with layer-4 includes the same coverage ratio as the fabricated circuit layout, the specific layout patterns include additional undesired parasitic effects, such as the eddy currents that further decrease Q_T, which have not been accounted for in the

model. Hence, the measured Q_T = 83.2 for the overlapping hex-PSCs are lower than both simulation and calculation results.

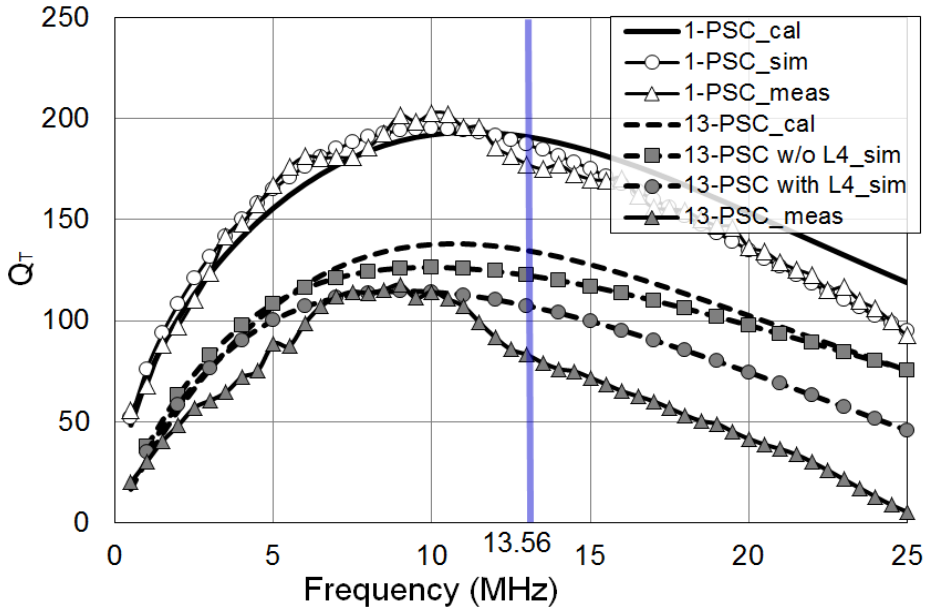

Figure 6.6: Comparison between calculation, simulation, and measurement results of the overlapping and non-overlapping hex-PSCs in terms of their worst-case quality factors in layer-2.

In order to better understand the effects of layer 4 metal plane, several metal strips that were 19.2 mm wide and changed the spacing between them to sweep the coverage ratio from 0% to 100% is used for simulation. Simulation results for Q_T of the overlapping hex-PSCs in different layers at 13.56 MHz *vs*. coverage ratios in Figure 6.7 show that when the coverage ratio increases, Q_T of the hex-PSCs drops because of the increased parasitic capacitance and resistance. Q_T of the hex-PSCs in layer 3, which is the closest to layer 4, drops to zero around 87% coverage, because the self-resonance frequency (SRF) of these PSCs falls even below 13.56 MHz. Q_T of the hex-PSC in a single PCB module without the second PCB is also measured for comparison. The resulting Q_T = 153 was close to the Q_T = 144 of layer 1 PSC with no layer 4 coverage as shown in Figure 6.7.

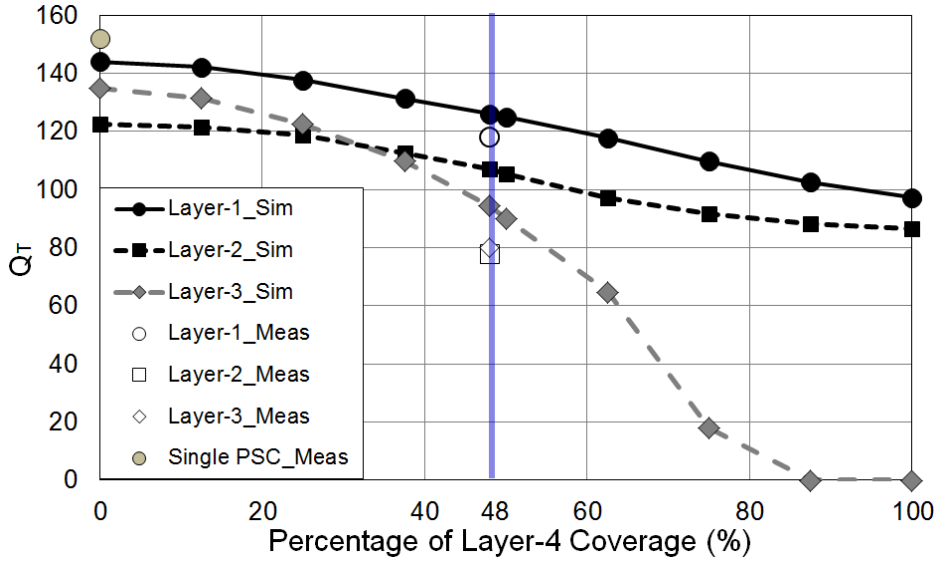

Figure 6.7: Q_T of the hex-PSCs in different layer *vs.* the coverage ratio of layer 4.

There are two issues of the deviation of measurement and simulation of Figure 6.6 and Figure 6.7. First, a more realistic pattern of layer 4 would include sensor circuits, power amplifiers, control circuits, power lines, and connectors as describe in Chapter 5. According [130] , the pattern of overlapping metal does affect the Q of the PSCs. Second, several overlapping PSCs for the worst case position in layer 2 are jointed. In other words, they are incomplete PSCs for single tile as shown in Figure 6.2d. Hence, the solder connections for the incomplete PSCs are not uniform. On the Rx side, as mentioned earlier, in order to protect the Rx coil against moisture and mechanical damage, it was embedded in plastic molding as part of the headstage [105]. The plastic material, however, adds to the Rx coil's parasitic resistance and capacitance because of the dielectric loss and dielectric constant, respectively. The dielectric loss mainly comes from the insulation material. Therefore, a considerable amount of energy will be dissipated across the parasitic resistance, and the Q_R will be decreased. Furthermore, when the dielectric constant of the insulator material increases, parasitic capacitance also

increases, and the SRF decreases. The lower SRF induces lower Q_R at high frequency. Figure 6.8 shows the effects of embedding the Rx coil in the plastic molding on the Q_R.

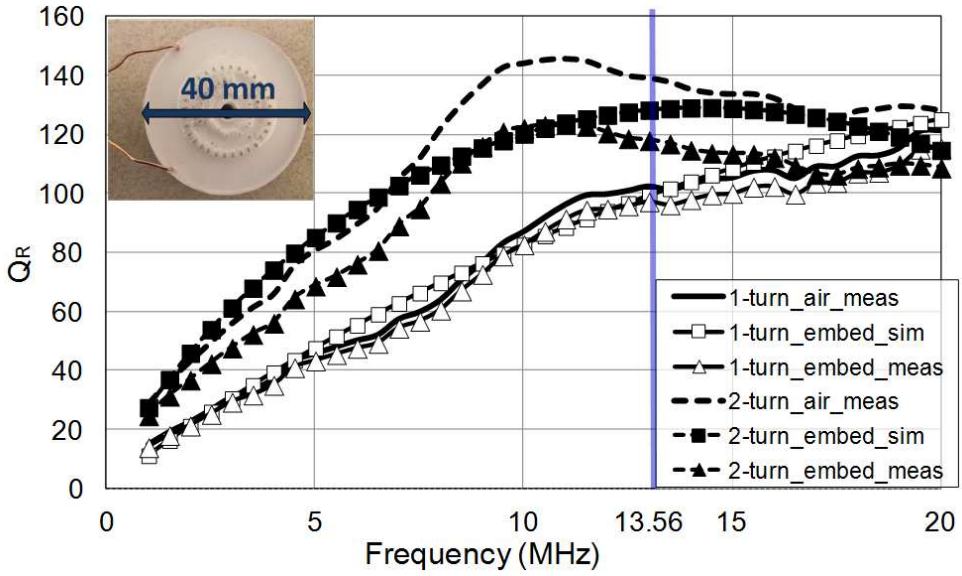

Figure 6.8: The effects of embedding the Rx coil in the plastic molding on Q_R.

6.2.2 Power Transfer Efficiency (PTE)

The PTE *vs*. coupling distance from the Rx coil of overlapping hex-PSCs for perfect alignment and the worst lateral misalignment (γ_{max} = 49.1 mm) are shown in Figure 6.9a and 6.9b, respectively. At D = 78 mm, lateral misalignment results in 10 to 15% drop in the PTE in calculations, simulations, and measurements. Any misalignment larger than γ_{max} will result in the switching of the active hex-PSC to the one that has a lower misalignment.

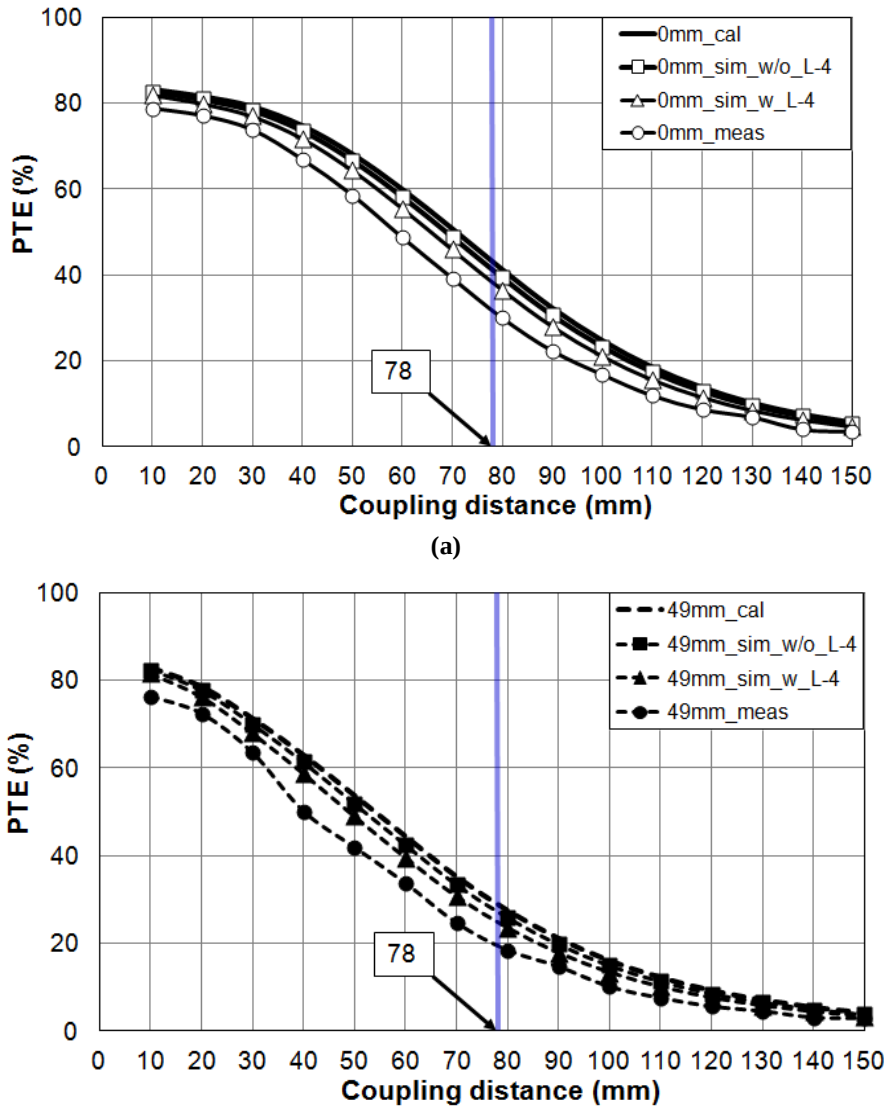

Figure 6.9: The resulting PTE *vs.* the coupling distance from the Rx coil. (a) perfect alignment. (b) Worst-case lateral misalignment (49 mm).

Figure 6.10a shows two adjacent overlapping PSCs with the gray areas indicating where they are activated if the center of the Rx coil is located within those regions. This region will be referred to as the active area of each hex-PSC. Figure 6.10a also shows two possible paths that the animal, carrying the Rx coil, might take from one hex-PSC to another. Along path-1, *i.e.* from point-a to point-b, the left PSC in 1ayer-2, which is centered at the origin, is activated for $0 \leq \gamma < 42.5$ mm, and then the right PSC in layer-1,

which is centered at X = 85 mm, is activated for 42.5 mm ≤ γ < 85 mm. Figure 6.10b shows the calculated, simulated, and measured PTE variations along path-1. It should be noted that the PTE of the right PSC overtakes that of the left PSC at X = 34.5 mm because according to Figure 6.7, Q_T of the hex-PSCs in layer-1 is higher than the hex-PSCs in layer-2. Nonetheless, in the location-based control scheme of the EnerCage system, the switching occurs at X = 42.5 mm. Figure 6.10c shows the PTE variations along path-2 (a to c). In this case, the left PSC is active for 0 ≤ γ < 49.1 mm, and layer-2 PSC is active for 49.1 ≤ γ < 75 mm. These curves clearly show the reason why γ_{max} = 49.1 mm is the worst-case lateral misalignment. Considering the hexagonal symmetry in Figure 6.2g, the red dots in Figure 6.10c shows the worst-case PTE variations as the Rx coil, on the animal body, moves from any random hex-PSC to another.

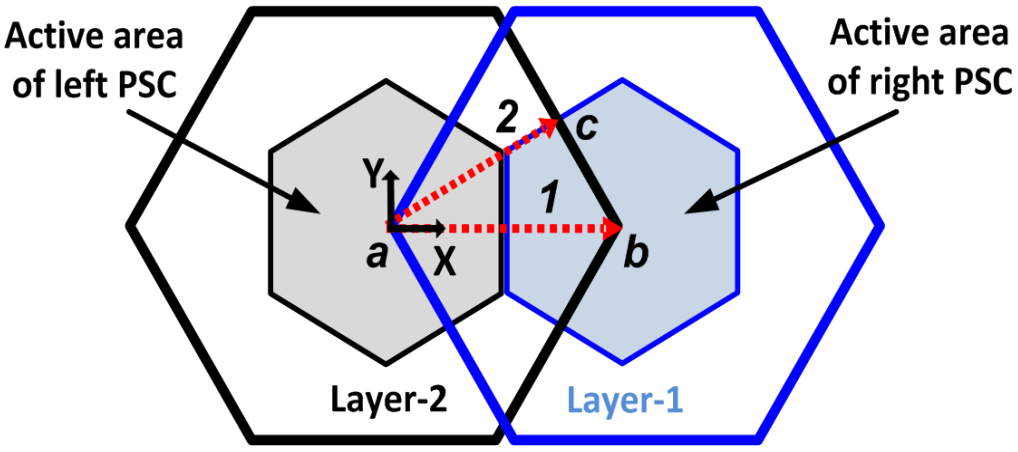

(a)

Figure 6.10. (a) Active areas of a pair of adjacent hex-PSCs in layer-1 and layer-2, where they are driven to energize the Rx coil. Also two possible lateral misalignment directions, path-1: from point a to b, and path-2: from point a to c. (b) PTE variations along path-1. (c) PTE variations along path-2.

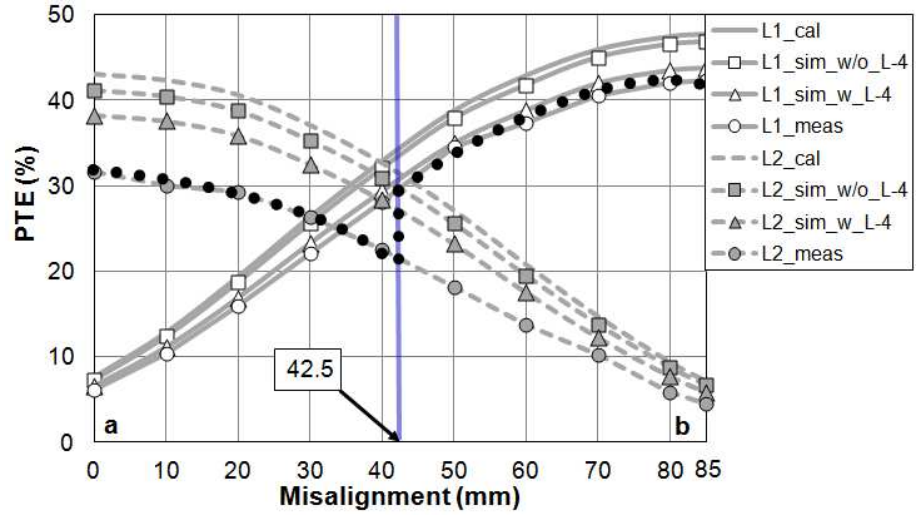

(b)

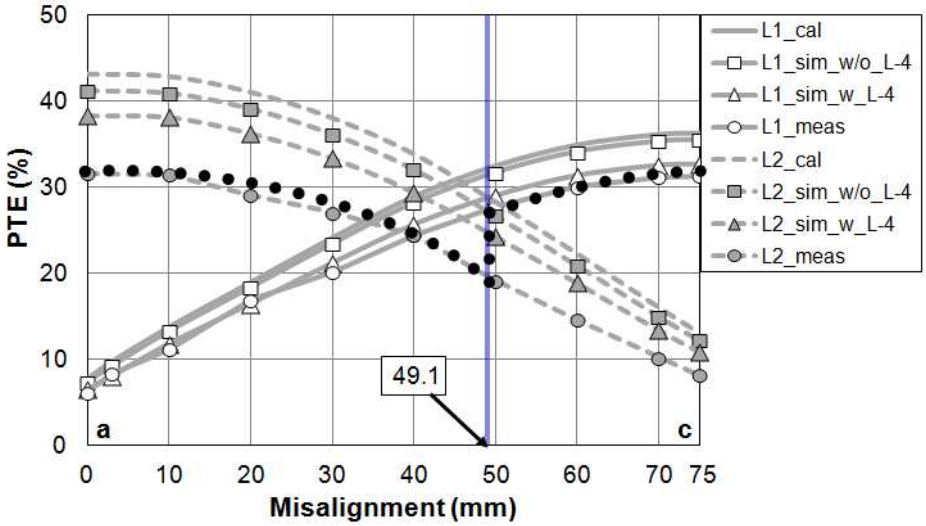

(c)

Figure 6.10: (b) PTE variations along path-1. (c) PTE variations along path-2.

6.2.3 Power Transfer Efficiency (PTE) Variations

Figure 6.11a shows a color-coded top view of the hex-PSC array, which matches the colors used in Figs. 6.1 and 6.2 for different PCB layers. The active area for each hex-PSC has also been identified, which covers one third of each hex-PSC area. Since the range of robotic arm motion in the XY plane was limited to 17×17 cm^2, the Rx coil was swept over each individual hex-PSC after adjusting the Z axis at a designated *D*. These

individual measurements were then combined to construct 3D maps of the PTE over the entire overlapping PSC array, as shown in Figs. 6.11b and 6.11c for D = 70 mm and 120 mm, respectively. Because of the specific design of the hex-PSC geometry, described in Section 6.2, the PTE variations at D = 70 mm were limited to 16.6% to 39.1% around an average PTE of 27.95%. PTE variations at D = 120 mm were even more homogenous, from 6.5% to 10.9% around an average of 9.02%. This is considerably better than the previous attempts in generating a homogeneous magnetic field in a large experimental arena for similar applications [97] and [106]. The hex-PSCs on layer 1 generated the highest peaks because of their shorter coupling distance to the Rx coil and less overlap with the other three layers.

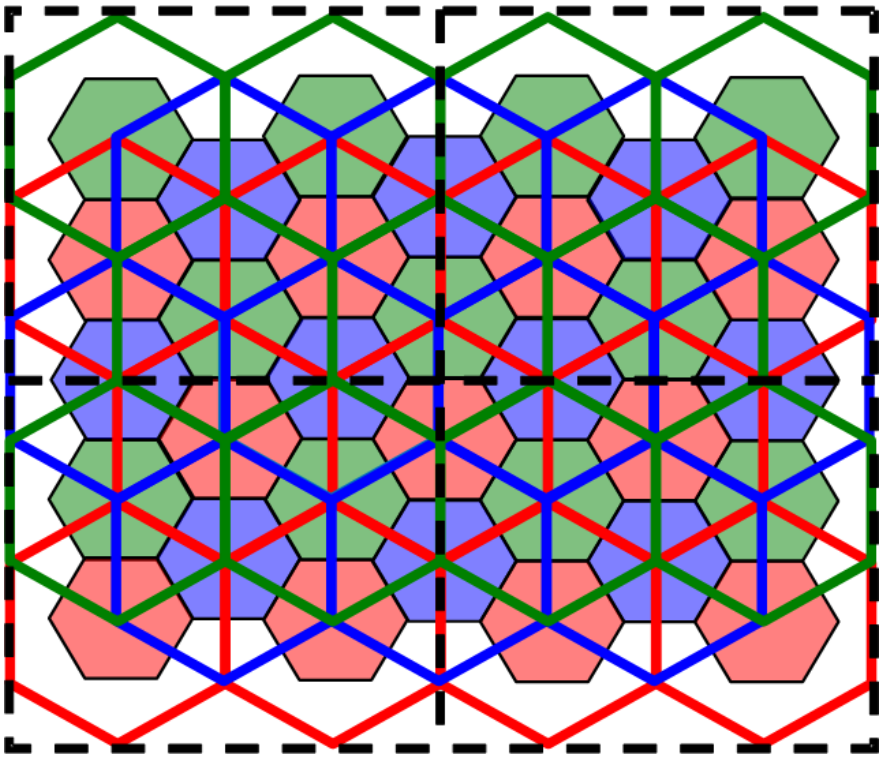

(a)

Figure 6.11: The PTE mapping of four hex-PSC units (2×2) at different coupling distances: (a) Active areas of each hex-PSC. (b) D = 70 mm; (c) D = 120 mm.

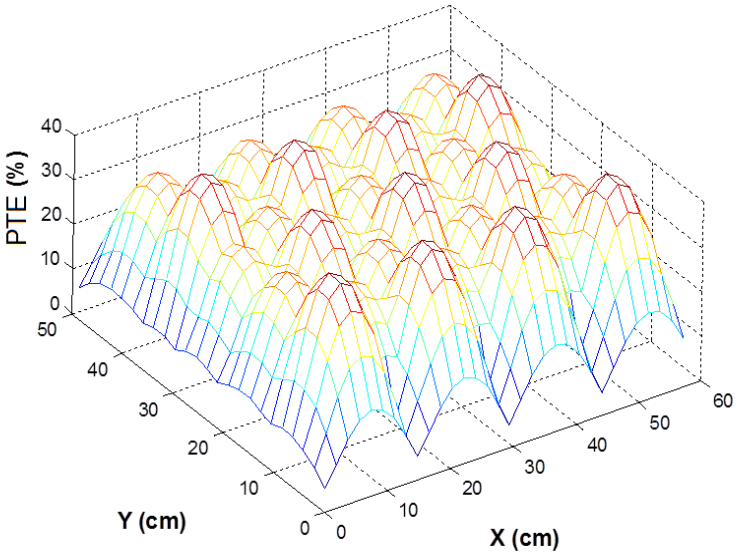

(b)

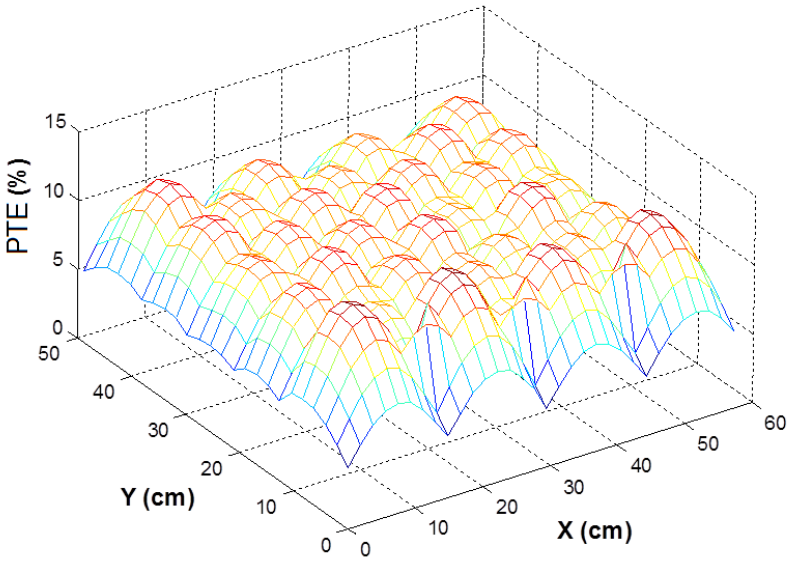

(c)

Figure 6.11: The PTE mapping of four hex-PSC units (2×2) at different coupling distances: (b) *D* = 70 mm; (c) *D* = 120 mm.

6.2.4 Angular Coil Misalignments (Tilting the Rx Coil)

Considering the awake animal subjects' behavior, the Rx coil is likely to be tilted on top of horizontal displacements. Therefore, it is important to understand the effects of the Rx coil angular misalignments. For a circular Rx coil, angular misalignments can

occur along the θ and φ axes in a spherical coordinate system, as shown in Figure 6.12. In order to create accurate and consistent angular misalignments along θ, the Rx coil was connected to an extension of the X-axis stepper motor in the robotic setup, shown in Figure 6.5, as it was held at the nominal height of D = 78 mm above the hex-PSC array. The stepper motor had 40 steps in a 360° rotation and, therefore, could change θ in 9° steps. The hex-PSC array itself was placed on a turn table to be manually rotated with similar step size to generate the φ misalignments. Figs. 12a and 12b show a good agreement between the simulation and measurement results of the Rx coil rotation when it was perfectly aligned above one of the hex-PSCs (γ = 0 mm), respectively. It can be seen that in this configuration, the φ misalignment does not affect the PTE because both the Tx PSC and Rx coil are almost circular. The PTE, however, is quite sensitive to θ misalignments due to $k \propto cos(\theta)$, and becomes very small when $\theta \approx 90^{o}$ [131]. Figs. 12c and 12d show similar results when the Rx coil is half way between the centers of two overlapping hex-PSCs (γ = 42.5 mm). In this case, the valley of the PTE occurs much earlier when $\theta > 60^{o}$ because of the small effective coupling area between the active hex-PSC and the Rx coil.

The PTE valleys in Figure 6.11 create temporary dead-zones across the experimental arena for the headstage electronics, which depend of the Rx-coil orientation. These are difficult to eliminate by modifying the overlapping hex-PSC geometry alone. Two solutions are considered to address this issue in the EnerCage system. 1. Activating two adjacent hex-PSCs simultaneously with out-of-phase signals to create a horizontal magnetic field, which is discussed in Section 6.3.5. 2. Adding a small auxiliary rechargeable battery or a super-cap to the headstage to work as a buffer and

store energy when the coils' coupling is good and temporarily supply the electronics when the Rx coil is in a PTE valley, or when the animal stands on its hind limbs, elevating the Rx coil above D_{max} = 120 mm.

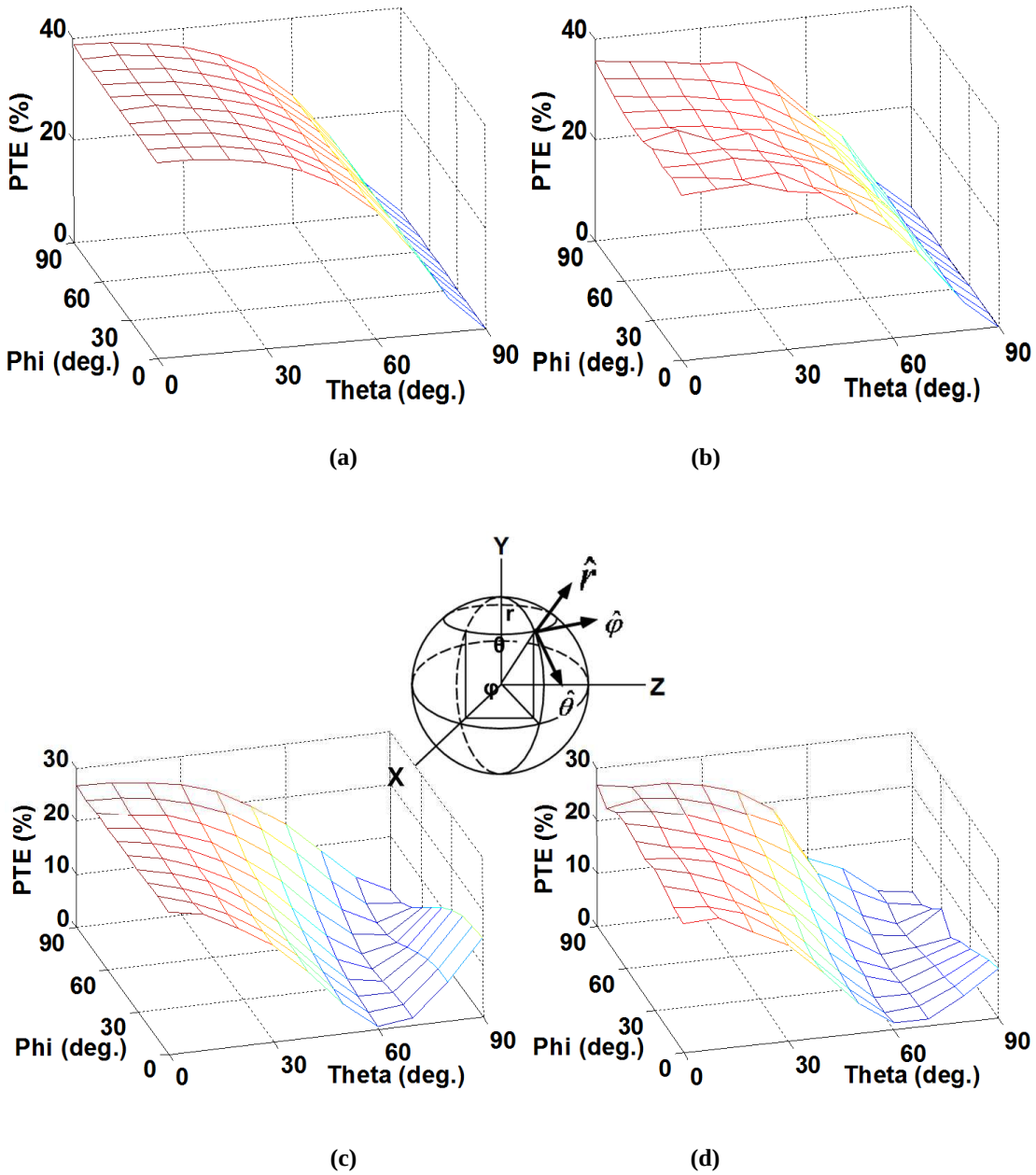

Figure 6.12: PTE *vs*. tilting angles for a layer-2 hex-PSC powering the Rx coil at the nominal D = 78 mm: (a) Simulation at X = 0 mm; (b) Measurement at X = 0 mm. (c) Simulation at X = 42.5 mm; (d) Measurement at X = 42.5 mm.

6.2.5 Horizontal Magnetic Field with Out-of-Phase PSCs

To address the problem of small PTE for a combination of severe angular ($\theta > 60^o$) and lateral misalignments, shown in Figure 6.11, the system activates a pair of overlapping hex-PSCs simultaneously with out-of-phase drive signals to create a horizontal flux between the two PSCs in a way that more flux is bent towards the Rx coil and pass through it. Figure 6.13 demonstrates a worst-case scenario, in which the Rx coil is held vertically ($\theta = 90^o$) in between the two PSCs at D = 78 mm and γ = 42.5 mm. The graphs compare the received power when the Rx coil is swept along path-1 in Figure 6.10a from the center of one hex-PSC (a) to the other (b) when they are either activated individually or simultaneously with 180º phase difference. The Tx power delivered to each hex-PSC in this experiment was set to 0.5 W [21]. It can be seen that by using the simultaneous activation method, the received power around γ = 42.5 mm has been almost tripled.

In fact with proper driver circuitry and choice of hex-PSCs it is possible to steer the magnetic flux in different orientations by controlling the phase difference and amplitude between power carrier signals applied to the hex-PSCs. Nonetheless, the received power above the center of the a PSC (γ = 0 mm or 85 mm) is still smaller than the desired 20 mW level, and therefore, the use of auxiliary means for energy storage in the headstage might be necessary for uninterrupted operation of the electronics attached to or implanted in the freely behaving animal body.

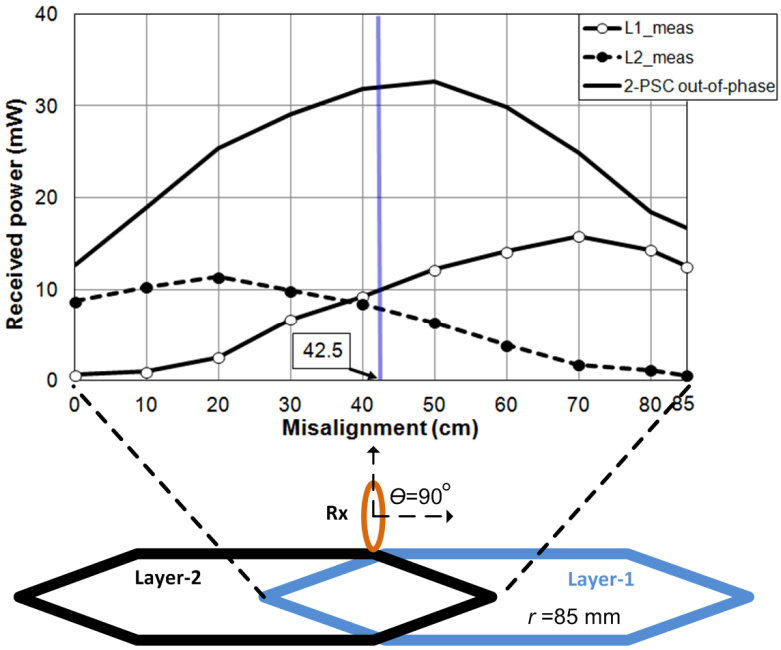

Figure 6.13: Comparison of misalignment (X) for different Tx PSCs with a tilting Rx coil (θ = 90° and φ = 0) at coupling distance = 78 mm.

6.3 Conclusions

This chapter includes an optimal design methodology for a scalable array of overlapping hex-PSCs with a modular architecture, arranged in a way that it can cover any wireless powering area by creating a homogenous magnetic field. Thr exemplar application for such a coil arrangement is continuous powering of the randomly moving electronics that are attached to or implanted in the freely behaving small animal subjects' body for long term behavioral electrophysiology experiments. The specific design of the hex-PSC module and implemented it on a pair of double-sided PCBs has provided. The PTE variations have been minimized by optimizing the hex-PSC geometries on the Tx side along with the Rx coil, while considering key parasitic components and practical constrains imposed by the application or fabrication process, to maximize the PTE in the worst-case scenarios, which are critical in maintaining operation over the entire

experimental arena. The idea is that in better conditions, when there is excess power available on the Rx side, a closed-loop power control mechanism can reduce the Tx power, as demonstrated in [120].

The worst-case in terms of parasitics that reduce the Q-factor was related to the hex-PSCs in the 2nd layer, each of which was surrounded by 12 other hex-PSCs. The worst lateral misalignment of the Rx coil was $\gamma_{max} \approx r_{o1}/\sqrt{3}$, and the worst angular misalignments were $\theta > 60^{o}$. Such angular misalignments, however, can be addressed to a large extent by the flux steering technique, which involves adjusting the amplitude and phase difference between two simultaneously activated PSCs. Nonetheless, embedding a small energy storage component in the Rx module seems to be inevitable for uninterrupted operation.

All theoretical models were verified by finite element analysis models that were constructed in a commercial field solver (HFSS), and further validated using a high precision robotic measurement setup. However, the complexity of the metal pattern of layer 4 degrades the optimization result.

In this chapter, a design methodology for an overlapping hex-PSC array has proposed to create a homogenous magnetic field for wireless power transmission for the preliminary EnerCage system. However, this preliminary system has several issues. In the next chapter, these issues are addressed and the new PSC design and improved system is introduced. Moreover, the preliminary *in vivo* animal experiment with the EnerCage system is performed.

CHAPTER VII

. THE NEW ENERCAGE SYSTEM WITH ANIMAL EXPERIMENT RESULTS

In Chapters 5 and 6, the preliminary EnerCage system and coil design methodology were introduced. In this system, each overlapping hexagonal planar spiral coil (hex-PSC) has its own sensor module and driver circuitry, which includes a radio frequency identification (RFID) reader and a power amplifier (PA). However, this design is not efficient in terms of power consumption and complexity because each PA only drives one PSC. Therefore, there is a need to reduce the number of drivers and sensors. Moreover, the communication between each control module and the personal computer (PC) is based on a central microcontroller (MCU), which is not easy to be modularized. Therefore, a new version of the EnerCage system called the “EnerCage-1” is presented in this chapter. The EnerCage-1 reduces the amount of driving circuitry and the number of sensors for the same amount of area by taking advantage of multi-coil coupling [56]. The EnerCage-1 is also equipped with “Xport” Ethernet modules, (Lantronix, Irvine, CA) each with its own internet protocol address (IP address) for communication with the PC. An Ethernet hub connects multiple control modules together into a single network, which the PC can then communicate with.

Figure 7.1 is a rendering of the most recent version of the system, the EnerCage-1. A wireless mobile unit in the form of a headstage or implant embedded with receiver (Rx) coils is inductively powered by an array of overlapping hex-PSCs that tile the floor of the cage [23]. The cross sectional view of overlapping PSCs is the same as in figure

6.2g. The power transfer efficiency (PTE) has been improved by using a combination of 3- and 4-coil coupling mechanisms [56]. On the transmitter (Tx) side, there are two kinds of PSCs: the driver PSC (Coil-1, L_1) and the primary PSC (Coil-2, L_2). On the Rx side, the secondary coil (Coil-3, L_3) and the load coil (Coil-4, L_4) are used to achieve maximum PTE while providing the optimal load condition. Driver PSCs, (red hexagons) driven by class-C PAs, are on layer 3, and primary PSCs are on layers 1 (blue) and 2 (green), as shown in Fig. 7.1. Each driver PSC is associated with two of the six primary PSCs that overlap it. This design reduces the number of drivers and control modules to one third the number used in the preliminary EnerCage system [21], while maintaining a high PTE. Each control module, mounted vertically under the PSC array at the locations of the yellow triangles in Figure 7.1., houses the control circuitry and three PAs that are connected to the three driver PSCs.

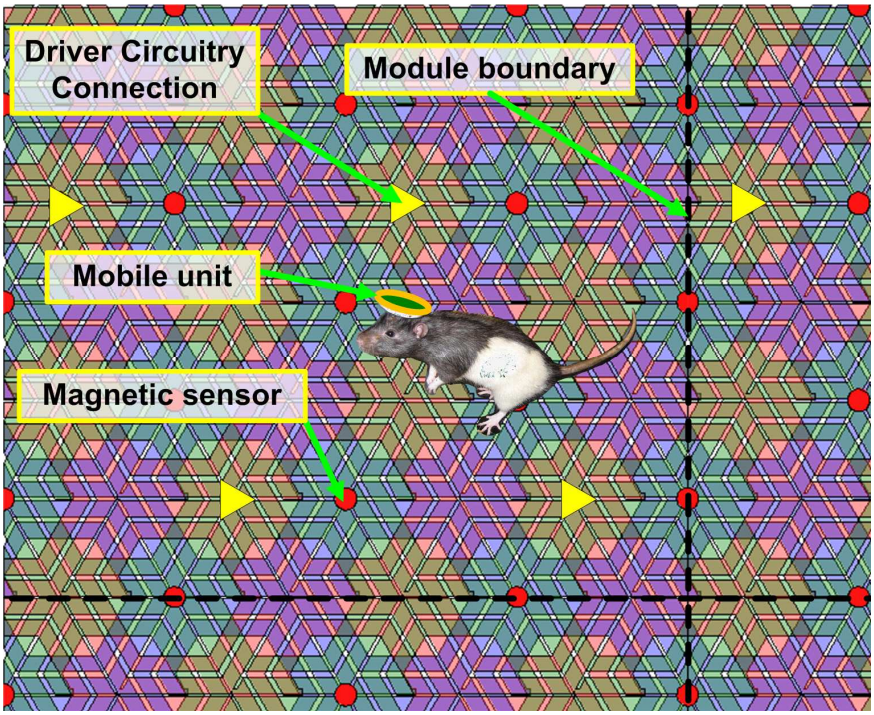

Figure 7.1: Top view of the array of overlapping hex-PSCs and magnetic sensors that tile the floor of a large experimental arena for EnerCage-1.

An array of 3-axis magnetic sensors (red dots), evenly distributed under the hex-PSC array, determine the location of a small magnet embedded in the center of the Rx coil. The number of sensors has been reduced by 2/3 compared to the previous design in [21], while maintaining the system tracking accuracy. In this chapter, the new system architecture, the multi-coil coupling mechanism introduced in Section 7.1, and the system tracking mechanism are briefly described in Section 7.2 [19]. The measurement results of the system characteristics and the animal experiment are shown in Section 7.3.

7.1 System Architecture and Coil Design of EnerCage-1

In this section, the system architecture of the EnerCage-1 is introduced. The PTE of the EnerCage-1 is improved by multi-coil coupling [56], and the concept of the multi-coil design and optimization is also discussed in this section.

7.1.1 System Architecture

The EnerCage-1 system block diagram, shown in Figure 7.2, consists of five key components: the stationary unit (PSC board), the control boards with driver circuitry that connect vertically under the PSC board via three SMA connectors, the closed-loop power control (CLPC) module [120], the mobile unit, and the central PC. As shown in Figure 7.3, each control board has an MCU (TI, MSP430), which is responsible for delivering control signals to three RFID readers (TI, TRF7960). Each of the RIFD readers then controls a 68% efficient class-C PA, which in turn drives a driver hex-PSC. The carrier frequency, f_c, is also set to 13.56 MHz to comply with the industrial, scientific, and medical (ISM) band, and the hex-PSC geometries have been optimized accordingly.

The MCU has several control pins that it uses to open the Tx PSCs that are not active. Each driver PSC then couples onto the Rx coil either directly or through one of its

two primary PSCs, depending on the position of the Rx coil. If the Rx coil is located above a driver PSC (L_1), the coupling mechanism is 3-coil coupling (L_1 to L_3 to L_4), but if it is located above a primary PSC (L_2), the driver PSC delivers power through that primary PSC via a 4-coil coupling (L_1 to L_2 to L_3 to L_4) mechanism [10]. Hence, each control module controls nine PSCs, three drivers and six primaries, and the active area of each is 1/3 of the PSC layout area, as shown in Figure 7.4. Since the effect of phase control on multi-coil coupling has not been studied yet, the 2:1 multiplexers (MUX) for 180° out-of-phase input signals that are used to address the tilting problem in the preliminary EnerCage system (Chapter 6) are removed.

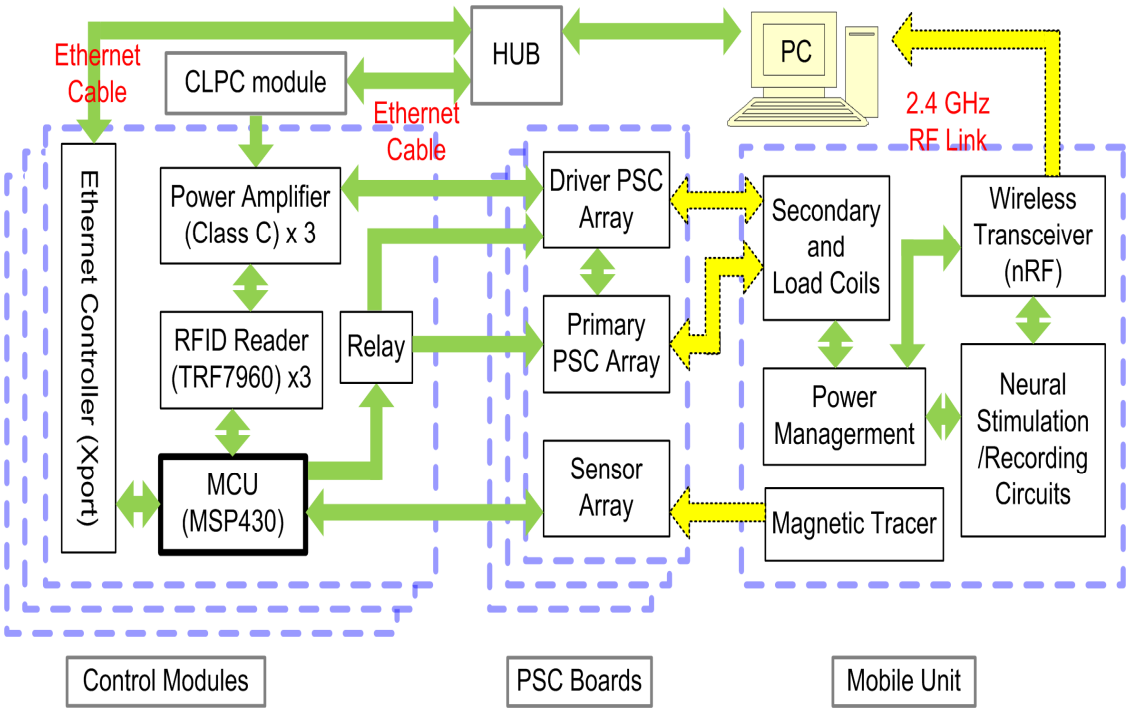

Figure 7.2: Block diagram of the EnerCage-1 system including drivers, PSCs and the mobile unit.

Each control module is also connected via flat cables to three magnetic sensor modules, AMI 360 (Aichi Steel, Aichi, Japan). Each sensor is mounted in the center of a

driver PSC, as shown in Figure 7.4 and collects 3D magnetic field data that it passes on to the MCU. The EnerCage-1 system runs with two different supply levels; a 5 V for all RFID readers, control circuits, and magnetic sensor modules, and a variable voltage provided from the CLPC module for the PAs.

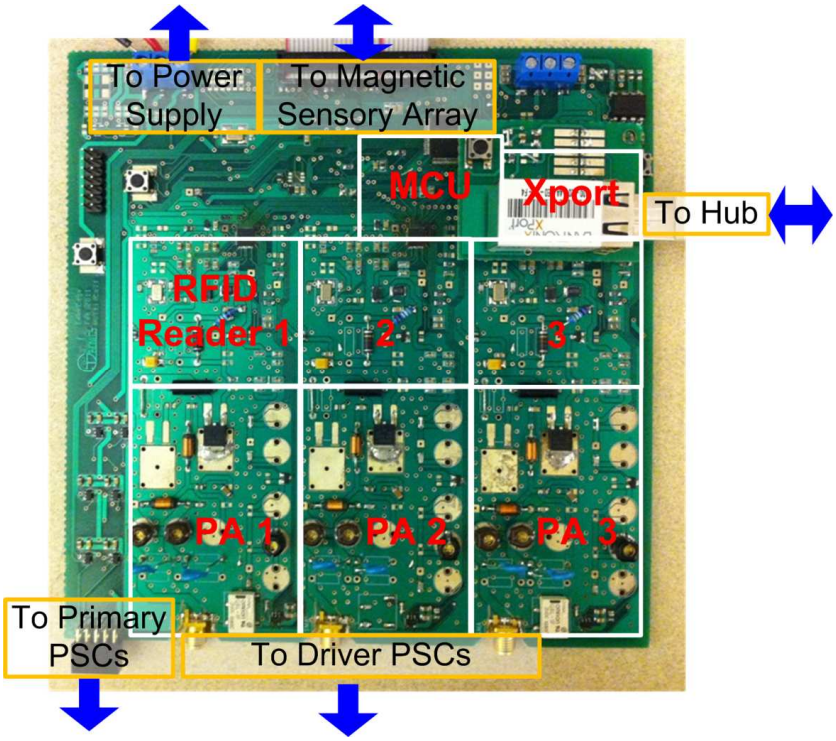

Figure 7.3: PCB layout of the EnerCage driver module, which can drive nine independent PCSs.

On the Rx side, the mobile unit shown in Figure 7.2 includes secondary and load coils which improve the PTE by transforming the load impedance [56]. The 13.56-MHz AC carrier on the Rx coil is first rectified by a rectifier (V_{rec}) and then digitized by an MCU (NRF24LE1). The mobile unit also includes a wireless transceiver (NRF24LE1) that operates at 2.4 GHz. This transceiver can be used to transfer biological data and power information when the LSK back-telemetry link is weak due to a large separation between Tx and Rx coils. The MCU generates short pulses (~10us) if V_{rec} > 4V and sends these pulses as back-telemetry data to the Tx using load shift keying (LSK), which is then

read by the RFID reader, and relayed back to the MCU of the control board. The MCU then bundles the magnetic sensor data with the back-telemetry data and sends it to the central PC via the Xport Ethernet communication module, which has been assigned a unique IP address. Any number of control modules can be used in order to extend the experimental area to have any desired size and shape. The PC collects data from all of the modules, records the tracking and biological data, and uses the algorithm discussed in Section 7.2 to determine which coil to activate. The PC then sends control commands to the MCUs of the control modules and the CLPC module, which has its own Xport and IP address. The CLPC is also connected to the hub and adjusts the PA supply voltage based on the PC command to regulate the Rx power [120].

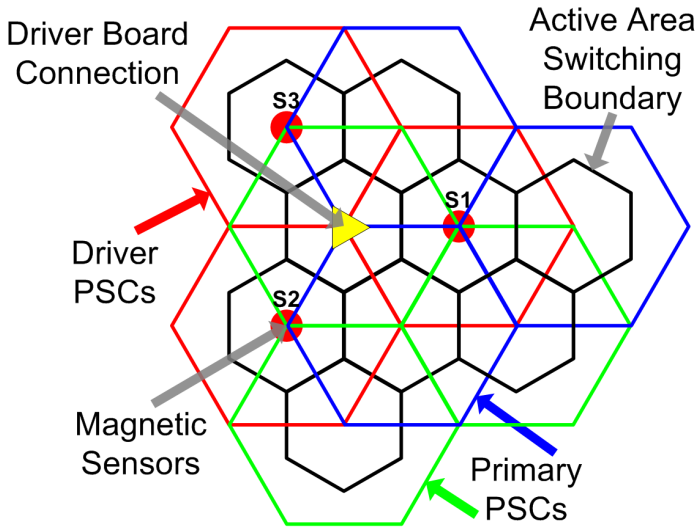

Figure 7.4: One module of the EnerCage-1: nine overlapped PSCs and their domains.

The main purpose of the mobile unit is to replace the batteries in the electronic or mechanical (*e.g.* pumps) devices that are attached to, or are implanted in, the animal body, and the design of its physical shape can be modified according to the needs of the application. For instance, in the current prototype, the mobile unit is designed to be part of a headstage with 32 movable tetrodes that will pick up single unit neural activity for a

wireless integrated neural recording (WINeR) data acquisition system [127]. The WINeR system wirelessly sends the neural signals to an independent receiver at 915 MHz after conditioning.

7.1.2 Multi-coil Coupling *

A popular technique for wireless power transfer is inductive coupling, which uses two coils referred to as the primary (L_2) coil and the secondary (L_3) coil, as shown in Figure 7.5a, and as discussed in Chapter 3. The PTE of the 2-coil link shown in Figure 7.5a can be found from [68].

$$\eta_{2-coil} = \frac{k_{23}^2 Q_2 Q_{3L}}{1 + k_{23}^2 Q_2 Q_{3L}} \cdot \frac{Q_{3L}}{Q_L} , \tag{7.1}$$

where $Q_L = \omega L_3 / R_L$, known as the secondary load quality factor, determines the efficiency from the secondary coil to the load *i.e.* Q_{3L} / Q_L, as discussed in Chapter 3. Based on (7.1), the efficiency profile of the 2-coil inductive link is a monotonically decreasing function of the coils' coupling distance. But for a given Q_2, Q_3 and k_{23}, there is an optimum load, $R_{L,PTE} = \omega L_3 / Q_{L,\,PTE}$, which can result in maximum PTE [132] at each coupling distance, and that can be found from

$$\frac{Q_3}{Q_{L,PTE}} = \sqrt{1 + k_{23}^2 Q_2 Q_3} . \tag{7.2}$$

In order to improve the PTE, a multi-coil coupling technique is introduced, in which two coils (secondary and load coils) are used on the Rx side to provide optimal load matching. 3-coil coupling occurs when just one Tx coil is used (driver coil). The mechanism of the 3-coil power transfer inductive link is shown in Figure 7.5b, and consists of one driver coil (L_1) on the Tx side, and secondary (L_3) and load (L_4) coils on the Rx side. The PTE of this system can be found from

* The equations of this section are mainly derived by Mehdi Kiani of GT-Bionics Lab, and the detailed works can be referred to [56].

$$\eta_{3-coil} = \frac{k_{13}^2 k_{34}^2 Q_1 Q_3 Q_3 Q_{4L} + k_{14}^2 Q_1 Q_{4L}}{\cos(\theta)\left(1 + k_{34}^2 Q_3 Q_{4L}\right)\sqrt{A^2 + B^2}} \cdot \frac{Q_{4L}}{Q_L} \tag{7.3}$$

where A, B and θ are written as

$$A = 1 + k_{13}^2 Q_1 Q_3 + k_{34}^2 Q_3 Q_{4L} + k_{14}^2 Q_1 Q_{4L}$$

$$B = 2 Q_1 Q_3 Q_{4L} k_{13} k_{14} k_{34}$$

$$\theta = \tan^{-1}\left(\frac{B}{A}\right). \tag{7.4}$$

For large coupling distances between driver and secondary coils, the effect of k_{14} is small and the PTE formula can be simplified to

$$\eta_{3-coil} = \frac{k_{23}^2 Q_1 Q_3}{1 + k_{13}^2 Q_1 Q_3 + k_{34}^2 Q_3 Q_{4L}} \cdot \frac{k_{34}^2 Q_3 Q_{4L}}{1 + k_{34}^2 Q_3 Q_{4L}} \frac{Q_{4L}}{Q_L}. \tag{7.5}$$

The 3-coil PTE given in (7.5) consists of two terms, the second of which is the PTE from L_3 to L_4, if they are considered to be a 2-coil inductive link. It can be shown that the first term is the PTE from L_1 to L_3 when L_3 is loaded by L_4.

4-coil coupling occurs when a primary coil is added between the driver and secondary coils (results in coupling from L_1 to L_2 to L_3 when L_3 is (?) loaded by L_4). The idea of the 4-coil inductive link (Figure 7.5c) is to have high PTE between the loosely coupled, high Q primary and secondary coils which are not loaded directly by the source or load impedances, respectively. The PTE in the 4-coil coupling link shown in Figure 7.2a can be found from [56]

$$\eta_{4-coil} = \frac{k_{12}^2 k_{23}^2 k_{34}^2 Q_1 Q_2 Q_2 Q_3 Q_3 Q_{4L}}{[(1 + k_{12}^2 Q_1 Q_2).(1 + k_{34}^2 Q_3 Q_{4L}) + k_{23}^2 Q_2 Q_3].[1 + k_{23}^2 Q_2 Q_3 + k_{34}^2 Q_3 Q_{4L}]} \cdot \frac{Q_{4L}}{Q_L}. \tag{7.6}$$

It should be noted that when the PA resistance is large, the additional driver coil in 4-coil links increases the PTE but reduces the power delivered to the load due to the large

impedance reflected into the driver coil. Furthermore, the worst position for the PSCs where PTE is concerned is the metal 2 layer because of the overlapping by the top and bottom PSCs.

The design of the inductive link for the EnerCage-1 system is based on 4-coil coupling. The three overlapping PSCs are in three metal layers of two 2-layer PCBs. If the animal subject moves to the driver PSC or to a primary PSC, the coupling mechanism is 3-coil or 4-coil coupling, respectively [10]. This mechanism reduces the number of driver PAs and maintains a high PTE [10].

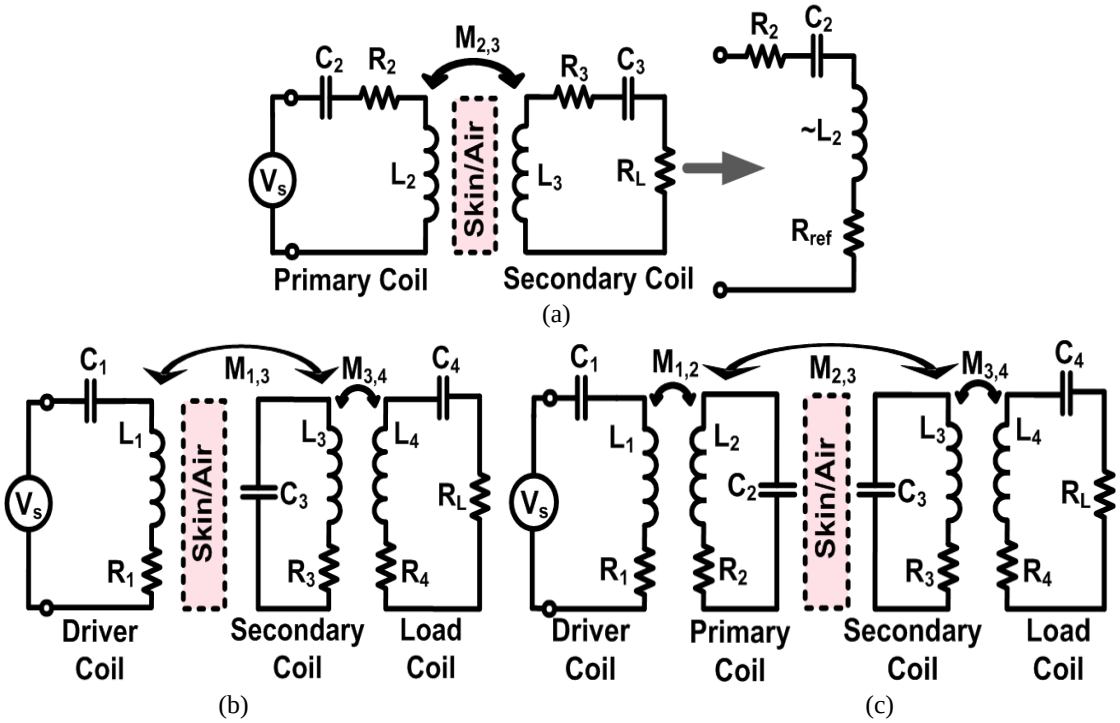

Figure 7.5: (a) Conventional 2-coil power transfer inductive link with reflected load equivalent [92]. (b) 3-coil power transfer inductive link. (c) 4-coil power transfer inductive link [56].

7.1.3 Design Procedure and Optimal Results

The design of the EnerCage PSC array is based on multi-coil coupling to achieve the highest possible PTE. Here, a summary of the optimization procedure is explained for 3-coil links. The details of 3- and 4-coil link optimization can be found in [56].

7.1.3.1 Design Procedure

For 3-coil link optimization that includes all parameters of L_1, L_3 and L_4, (7.3) can be used. However, this equation is overly complicated because it considers all coils' parameters at the same time. Hence, (7.5), the simplified version of (7.3), is used. Since the first term of (7.5) is dominated by L_1 and L_3, it can be simplified to:

$$\eta_{1,3} \cong \frac{k_{13}^2 Q_1 Q_3}{1+k_{13}^2 Q_1 Q_3}. \tag{7.7}$$

The second term of (7.5) is dominated by L_3, L_4 and the load (R_L). Hence, the optimization includes two parts. The first part is done for L_1 and L_3 based on (7.7) where Q_1, Q_3, and k_{13} should be maximized while considering the application and fabrication constraints. Depending on the application, the size of L_3 may be limited. The optimization procedure for the L_1-L_3 link is quite similar to the one found in [7]. The second part of the optimization shown in Figure 7.6, which is based on (7.5) for L_3 and L_4, starts with a preliminary value of L_1 and L_3 with a fixed load impedance. After finishing the iterations of the second part, the approximated maximum PTE can be estimated. Then, the new geometry of L_3 should be compared with the previous geometry of L_3 from the first part. If the geometry of L_3 has changed, the procedure returns back to the first part with the new L_3 geometry to optimize the geometries of L_1 and L_3. If the geometry of L_3 does not change, the procedure is finished, revealing the optimal coils' geometries.

For 4-coil inductive link, the optimization procedure is also separated into two parts, the first of which is the same as that of the 3-coil link. In the second part, L_1, L_3 and L_4 are optimized with a fixed load based on (7.2). Then the interim geometry of L_3 is used to determine if the geometries obtained in the second part are optimal. The

optimization procedure for 4-coil links is included in Figure 7.6. Here, L_3 is used to determine the optimal link rather than L_1 because L_3 is in strong coupling with L_4 which is connected to the load. Moreover, PTE is almost fixed if k_{12} is above a certain value. Therefore, the L_1 geometry variation is less than the L_3 geometry variation.

In the PSC array design, the model of overlapping PSCs with parasitic effects discussed in Chapter 6 is used for 4-coil coupling optimization. In order to create a homogenous magnetic field, the geometries of the overlapping hex-PSCs, which act as driver and primary PSCs in the 4-coil link, are identical. In order to have a conventional design example, the PCB process discussed in Chapter 6 is used for the PSC array, and the constraints are similar to those shown in Table 6.1. In addition, some of the parasitic effects are ignored here, as they were in Chapter 6.

As for the Rx coils, two designs are studied, referred to as Set-1 and Set-2. Set-1 is used in preliminary tests, and has wire-wound coils for L_3 and L_4 that provide high PTE. The diameter of the coils is limited to 40 mm, a value chosen based on the parameters of the WINeR system [127]. For Set-2, a wire-wound coil is again used for L_3 to improve Q, but a PCB multi-layer coil is used for L_4 to reduce the size of the mobile unit. The layout of L_4 is shown in Figure 7.7. The diameter of L_3 is 40 mm [105], and the diameter of L_4 is 25 mm, or roughly the size of a quarter coil size. After the geometry is decided, the iterative design procedure is executed using the optimization shown in Figure 7.6. Furthermore, a field solver, HFSS (Ansoft, Pittsburgh, PA), is used in the design procedure to verify and fine tune the values suggested by the theoretical models. The simulation model includes all possible eddy current effects from the overlapping PSCs in layers 1 to 3. The optimization results from simulation are shown in Table 7.1.

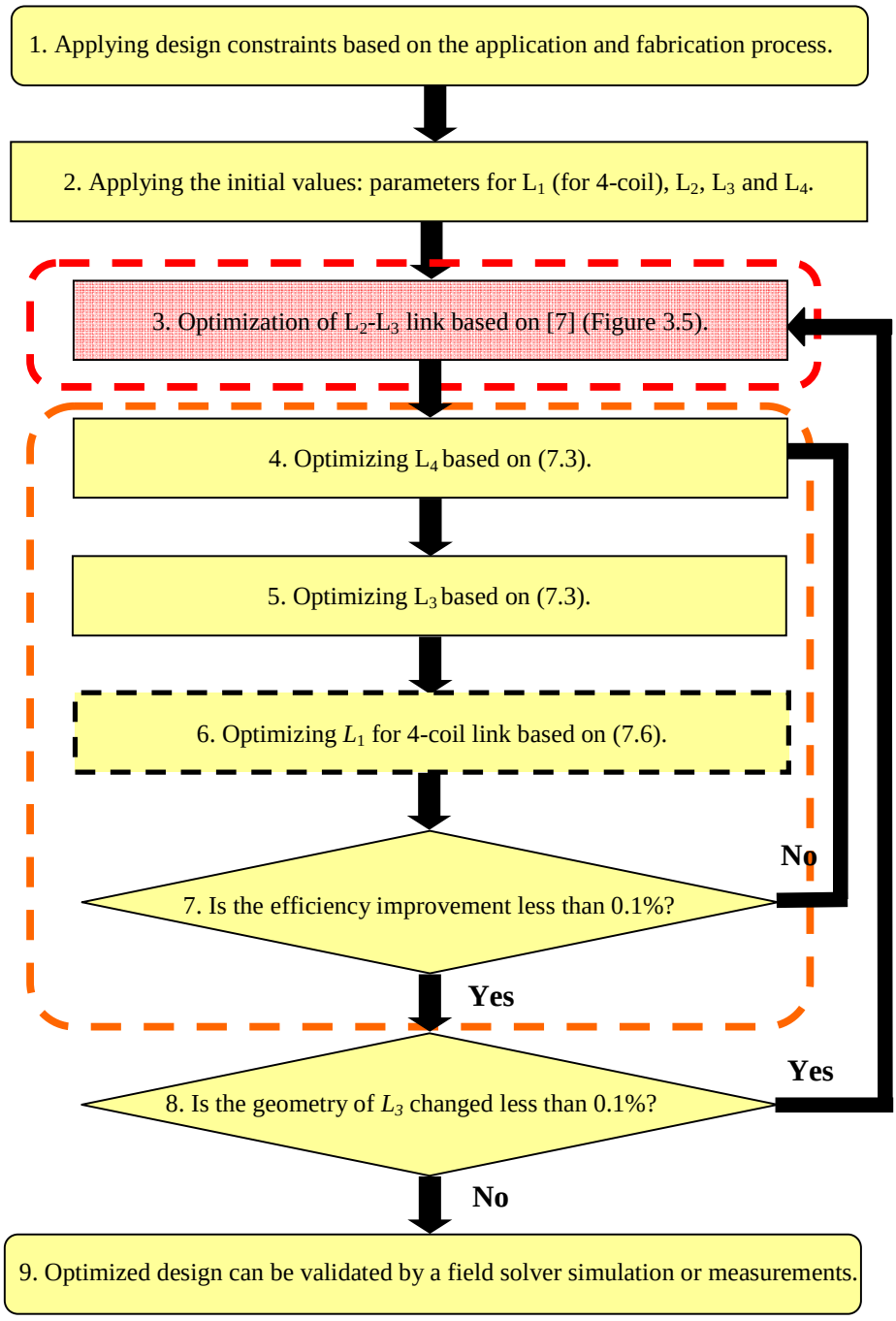

Figure 7.6: Iterative multi-coil inductive link design flowchart.

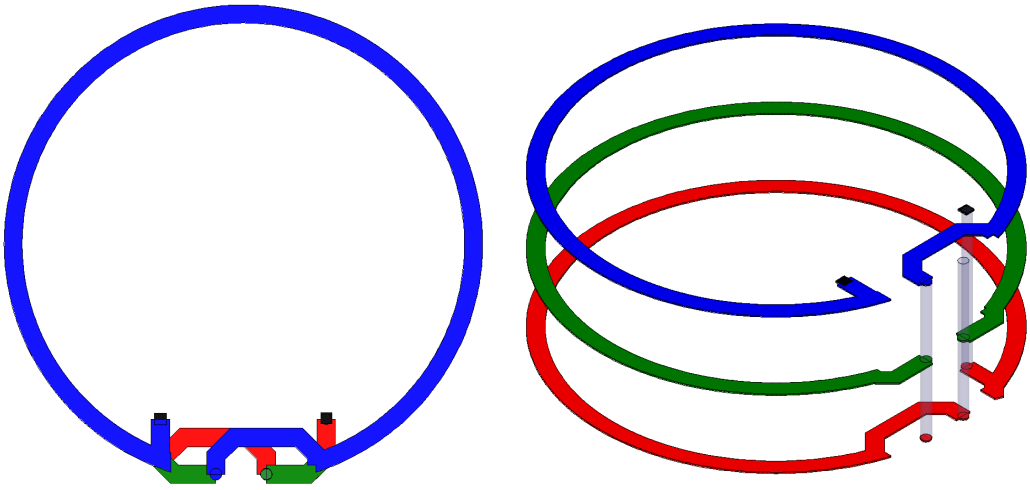

(a) **(b)**

Figure 7.7: Three-turn multi-layer PCB coil. (a) Top view. (b) 3D view.

7.1.3.2 Optimal Results

Table 7.1 shows the geometries and specifications of coils that have been optimized for 4-coil inductive links. The driver coil (L_1) and the primary coil (L_2) are hexagonal PSCs fabricated with 1-oz copper (thickness = 35 µm) on 1.6 mm thick-FR4 substrates. For the Set-1 design, the Rx coils are fabricated with AWG-22 magnet wire (diameter = 0.64 mm). For the Set-2 design, the secondary coil (L_3) is fabricated using AWG-22 wire (diameter = 0.64 mm) in order to achieve maximum *Q*, and the load coil (L_4) is designed on multiple layers of the Rx PCB with a line width of 1 mm. Disregarding situations in which the Rx coil is tilted, the maximum misalignment (and therefore the minimum PTE) between the Tx and Rx coils occurs when the center of the Rx coil is displaced from the center of the Tx coil by $\sqrt{3}$ of the PSC radius (48 mm). In these results, the PTE of Set-1 is still higher than that of Set-2 because L_4 in Set-1 has larger diameter, which results larger the coupling of L_1 or L_2.

Table 7.1. OPTIMIZED GEOMETRIES AND INDUCTIVE LINK CHARACTERISTICS FROM SIMULATION RESULTS

Parameters	Design Value	
PSC driver coil (L_1) and primary coil (L_2)	Inductance = 0.68 μH Outer diameter = 16.6 cm Number of turns = 2 Line width = 8.66 mm Line spacing = 2.60 mm Quality factor = 163 for driver PSC on layer 1 Quality factor = 127 for primary PSC on layer 2 Quality factor = 155 for primary PSC on layer 3 Weight = 3.3 g	
Wire-wound secondary coil (L_3): **Set-1**	Inductance = 1.25 μH Coil Diameter = 40 mm Wire diameter = 0.64 mm Number of turns = 3 Quality factor = 188 Weight = 1.0 g	
Wire-wound secondary coil (L_4): **Set-1**	Inductance = 0.72 μH Coil Diameter = 40 mm Wire diameter = 0.64 mm Number of turns = 2 Quality factor = 155 Weight = 0.7 g	
Wire-wound secondary coil (L_3): **Set-2**	Inductance = 1.25 μH Coil Diameter = 40 mm Wire diameter = 0.64 mm Number of turns = 4 Quality factor = 196 Weight = 1.4 g	
PCB multi-layer coils (L_4): **Set-2**	Inductance = 0.37 μH Coil Diameter = 25 mm Line width = 1 mm Number of turns = 3 Quality factor = 177 Weight = 0.3 g	
L_2 and L_3 nominal relative distance (d_{23})	120 mm (k_{23} = 0.033)	120 mm (k_{23} = 0.035)
L_3 and L_4 relative distance (d_{34})	30 mm (k_{34} = 0.33): **Set-1**	18 mm (k_{34} = 0.28): **Set-2**
Overall efficiency (%) at d_{23} = 120 mm Max / Min*	12.8 / 6.2 (3-coil): **Set-1**	12.2 / 5.8 (3-coil): **Set-2**
	12.6 /5.8 (4-coil): **Set-1**	12.4 /5.6 (4-coil): **Set-2**
Nominal Loading (R_L) (ohm)	500	

*Maximum misalignment (γ_{max}) = $83/\sqrt{3}$ = 48 (mm)

7.1.3.3 Link Budget for Multi-coil Coupling

The link budget of a typical communication system indicates how the transmitted signal is 'spent' as it travels through the link and is received by the receiver. It is therefore a balance sheet of energy gain and consumption along the communication path. In this chapter, the energy gain and consumption of the multi-coil coupling is analyzed to

understand the power consumption of each stage. Since the worst case coupling is 4-coil coupling in maximum misalignment with Set-2 coils, only this case is analyzed for the link budget. Table 7.2 shows the efficiency at each step of the inductive link in multi-coil coupling for Set-2 coils, and the load is 500 ohms in this design. In Table 7.2, the maximum loss occurs between L_2 and L_3, which is expected.

7.2. LINK BUDGET FOR THE 4-COIL COUPLING FOR SET-2 RX COILS IN MAX MISALIGNMENT

Parameters	4-coil Coupling
PA (%)	68
Matching of Tx circuit (%)	98
Connection (%)	99
L_1 to L_2 (%)	78
L_2 to L_3 (%)	11
L_3 to L_4 (%)	66
Matching of Rx circuit (%)	98
Total (%) Max / Min*	3.6

7.1.4 Design of the PSC Array

The PSC manufacturing process limits the shape of a unit tile to a rectangular form, as shown by the black boundary in Figure 7.8. Each unit tile includes 23 complete PSCs (eight PSCs in layer 1, eight PSCs in layer 2, and seven PSCs in layer 3), and 30 incomplete PSCs. The driver circuitry controls three driver PSCs and six primary PSCs as shown in Figure 7.3, so each tile has a total of 12 driver PSCs that are divided into 4 controller modules. Figure 7.8 also shows the layout of the 43 partial hex-PSCs associated with each tile when completed by the eight adjacent PSC tiles. This figure clearly shows how the EnerCage modular architecture can be scaled to support any arbitrarily-sized experimental arena. Each module also has 12 3-axis magnetic sensors, represented by the red dots in Figs. 7.1 and 7.8. Figs. 7.9a and 7.9b show the layouts of the two 2-layer PCBs that are designed based on the specifications in Table 6.2. The fourth layer of this design is used to connect the control modules to the PSC array tiles.

The matching capacitors and relays of the primary PSCs are also on the fourth layer.

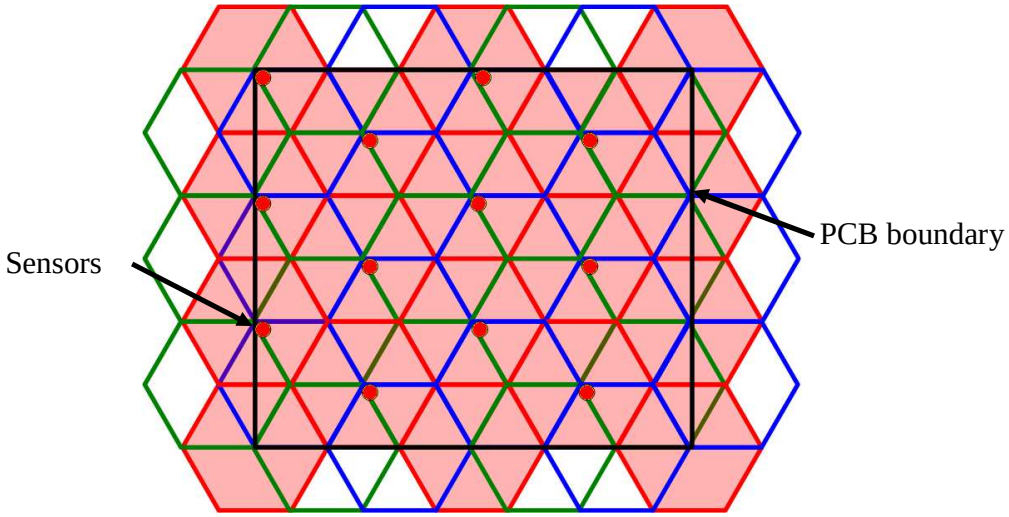

Figure 7.8: Each stationary unit tile has 12 drivers for 12 driver PSCs and 36 primary PSCs. Each driver PSC has one magnetic sensor in the center.

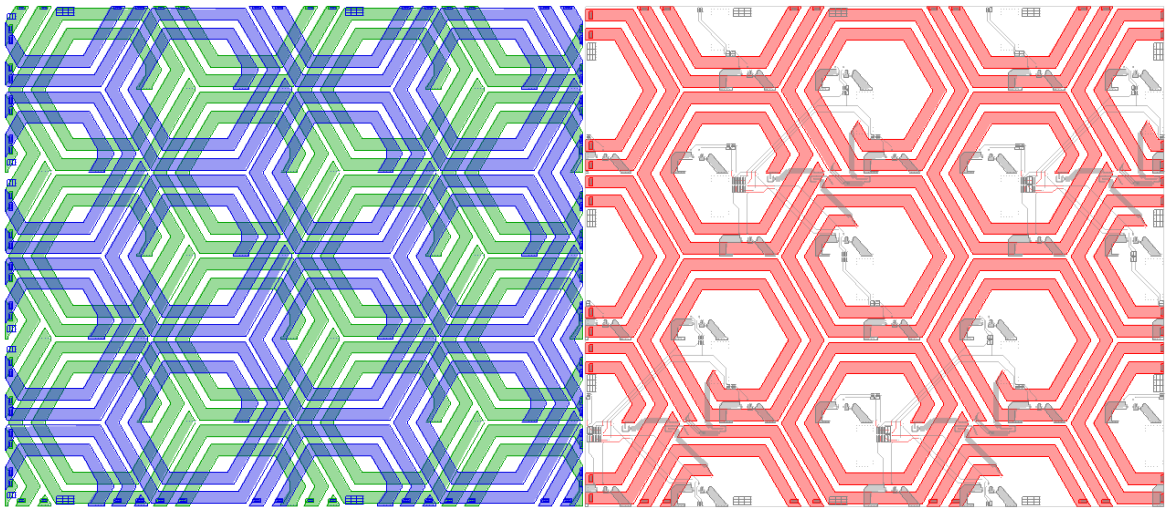

(a) **(b)**

Figure 7.9: PCB design for unit tile of the EnerCage-1 3-layer overlapping hex-PSCs (51.2 × 44.4 cm^2). (a) PCB1 for layers 1 and 2. (b) PCB2 for layers 3 and 4.

7.2 Sensor Tracking Algorithm*

In order to minimize power consumption, only one driver is activated at any given time. The system continually monitors the animal's movement and turns on only the PSC closest to the mobile unit. Ideally, it switches the active PSC when the magnet reaches the halfway point between two adjacent coils. Due to the fact that each hex-PSC has six

neighbors, the ideal switching points form a hexagonal boundary, represented by the black outlines in Figure 7.3. Red hexagons in this figure are the driver PSCs, and the adjacent blue and green hexagons at the 3 and 5 o'clock positions are the primary PSCs that are associated with them. Red dots represent the magnetic sensors, and the yellow triangle indicates the driver board entry port, as in Figure 7.1. The black hexagons are referred to as the active domains of the underlying hex-PSCs.

The sensors' raw data is first converted into a scalar value by performing a vector sum of the three axis magnetic field components. Since each sensor is located directly below the center of a driver PSC, the system is programmed to activate that PSC when its sensor value surpasses an experimentally determined high threshold, *Th_H*. When three adjacent sensors report values greater than a low threshold, *Th_L*, the system activates the primary PSC that is between those three sensors. For example, if the sensors under the red PSCs in Figure 7.3 read values >*Th_L*, then the green PSC between them is activated by the red driver PSC on the upper left side of the module. The red circles in Figure 7.10 represent the domains of the driver PSCs. Since the location of the magnet is determined by a simple threshold scheme, a circular boundary around each sensor represents the area in which the magnet generates a value above *Th_H* for that sensor. The larger, yellow circles surrounding each sensor represent the area within which the magnet generates a value above *Th_L*. The primary PSCs' theoretical domains, as defined by the intersection of three adjacent yellow circles, are intrinsically Reuleaux triangles, as indicated by the blue dashed outline. However, since the program checks for values above *Th_H* first, priority is given to the high threshold circles, and the resulting domain around the primary PSCs is the 6-sided green area shown in Figure 7.9.

* The graphic user interface (GUI) and control software of this section are developed by Peter McMenamin of the GT-Bionics Lab, and the detailed works can be referred to in [19].

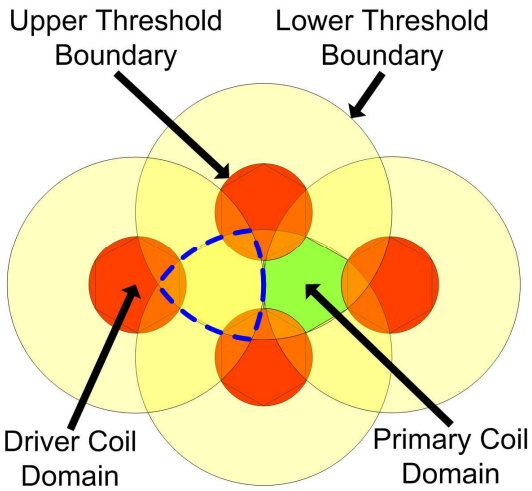

Figure 7.10: Domains for the upper (red) and lower (yellow) thresholds in the localization.

In the central PC each sensor value is first compared to *Th_H* and then *Th_L*. If a value is greater than *Th_H*, the PC turns on the driver PSC associated with that sensor. If the value is between *Th_H* and *Th_L*, the program checks the values of the adjacent sensors, and if those sensors also surpass *Th_L*, the system turns on the appropriate primary PSC. If the value is lower than both thresholds, the program moves on to the next sensor value. If the last sensor fails to surpass either threshold, the last chosen PSC remains activate.

This last feature is important for situations in which the magnetic tracer moves out of the range of all sensors. Occasionally, the animal subject stands up on its hind legs or explores the perimeter of the arena by partially climbing the walls. In such cases, the mobile unit may still be within the range of the Tx even if the magnet is not within the range of the sensors. Therefore, by continuing to power the previously activated PSC, the system can deal with an unknown state. While the magnet is out of range, the PC continues to monitor the sensors, so that when the tracer is detected again, the active PSC jumps instantly to the new location.

7.3 Measurement Results

In order to demonstrate the efficacy of the multi-coil links in improving PTE as compared to conventional 2-coil links, several measurement results are presented. The control of the overall system and the magnetic tracking are also demonstrated in this section, as well as the *in-vivo* experimental results for the EnerCage-1. A setup consisting of four PSC PCBs is shown in Fig. 7.11.

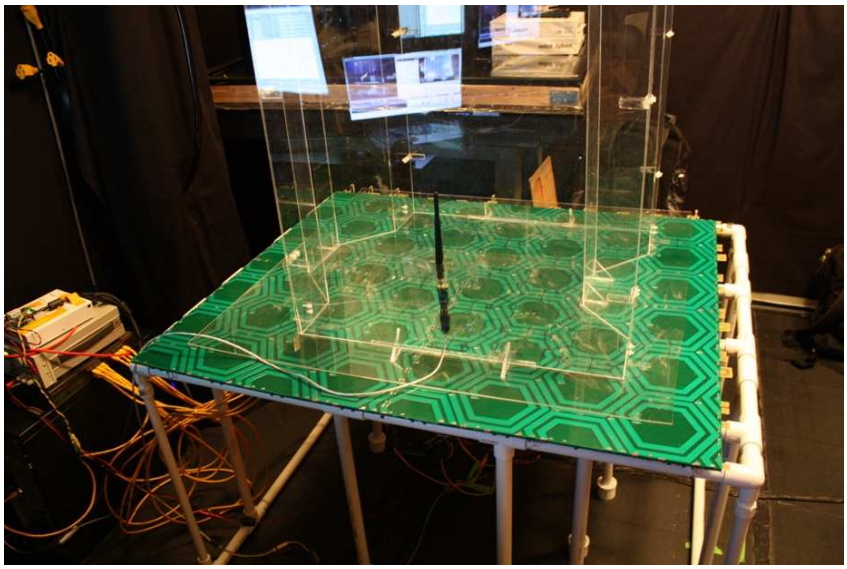

Figure 7.11: Measurement setup made up of 4 hex-PSC unit tiles of Figure 7.9.

7.3.1 Power Transfer Efficiency

For the EnerCage-1, the inductive coupling mechanism is based on multi-coil coupling, and Figure 7.12 shows the calculated, simulated, and measured PTE results for different coupling paths while the Tx and Rx coils are perfectly aligned. The load on the Set-1 mobile unit is 500 Ohms. In order to provide a comparison, the measurement results for 2-coil coupling are also provided. The 2-coil link consists of primary and secondary coils while in the 3-coil coupling, the receiver is on the driver PSC of layer 3. For 4-coil coupling, the receiver is on the primary PSC of layer-2. In Figure 7.12, the

multi-coil coupling provides higher PTE at long distance (> 6 cm). The PTE of 3-coil is lower than PTE of 4-coil because the driver PSC is on layer-3, which is the lowest PCB layer.

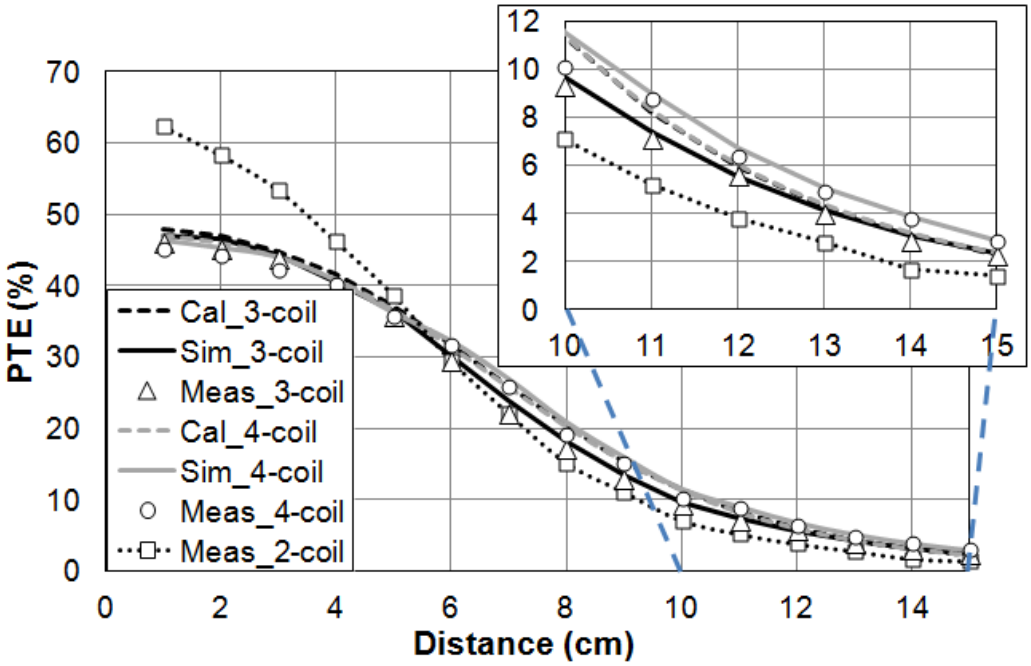

Figure 7.12: The resulting PTE *vs.* the coupling distance from the receiver for different coupling mechanism.

7.3.2 System Functionality

In order to demonstrate the overall functionality of the system, six modules including 54 complete PSCs were tested in a 2×3 array, as shown in Figure 7.13. The diameter of each hex-PSC was 17 cm, and each active area was 62.57 cm^2, for a total area of 3378 cm^2. The mobile unit had a pair of wire-wound coils with 3 turns and 2 turns for L_3 and L_4, respectively, as shown in Table 7.1 for Set-1 [19]. In the center of the secondary coil, two disk shaped rare-earth magnets (∅9.5 mm, 1.5 mm thick, B_{rmax} = 14,800 G, 0.85 g) were mounted as the tracer. The localization thresholds were set at *Th_H* = 120 and *Th_L* = 60, based on the sensor values observed at the edges of the red

and yellow circles in Figure 7.4, at a height of 12 cm. These values correspond to field magnitudes of 0.114 and 0.037 G, respectively, after accounting for sensor scale and offset.

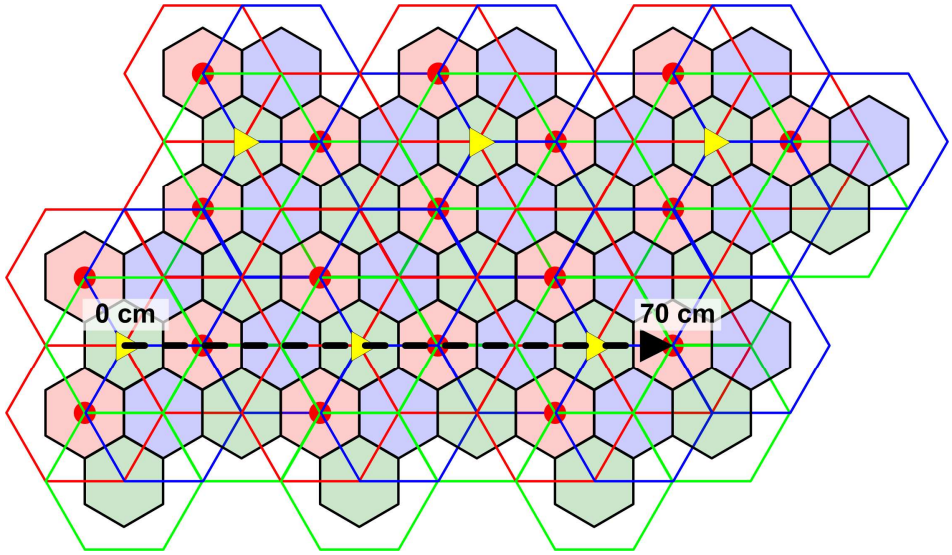

Figure 7.13: An exemplar mobile unit path for 2×3 control modules array.

In Figure 7.10, the red and green domains indicate the locations and the black outlines indicate the system should theoretically switch. These positions can be determined by the geometry of the coils, but vary from the actual switching locations. To demonstrate the error in the switching points of the activated PSCs, the mobile unit was moved along the 70 cm path that is indicated by the dotted arrow in Figure 7.13 at a height of 12 cm above the PSC array. As the magnetic tracer moved from the center of the green primary PSC at the beginning to the center of the red driver PSC at the end of the arrow, the mobile unit voltage varied by $V_{p\text{-}p,OL}$ = 6.15 V and $V_{p\text{-}p,CL}$ = 0.4 V in the open- and closed-loop conditions, respectively, as shown in Figure 7.14. During open-loop operation, the PA supply was fixed at 15 V, but during closed-loop operation, it varied from 5 V to 20 V to maintain a mobile unit rectifier output of 5 V.

The dotted vertical lines mark the location of the theoretical switching points, while the solid vertical lines mark the location of the actual switching points. The horizontal separation between these lines can be considered as a measure of the localization accuracy of the system using the simple thresholding control method in Section 7.2.

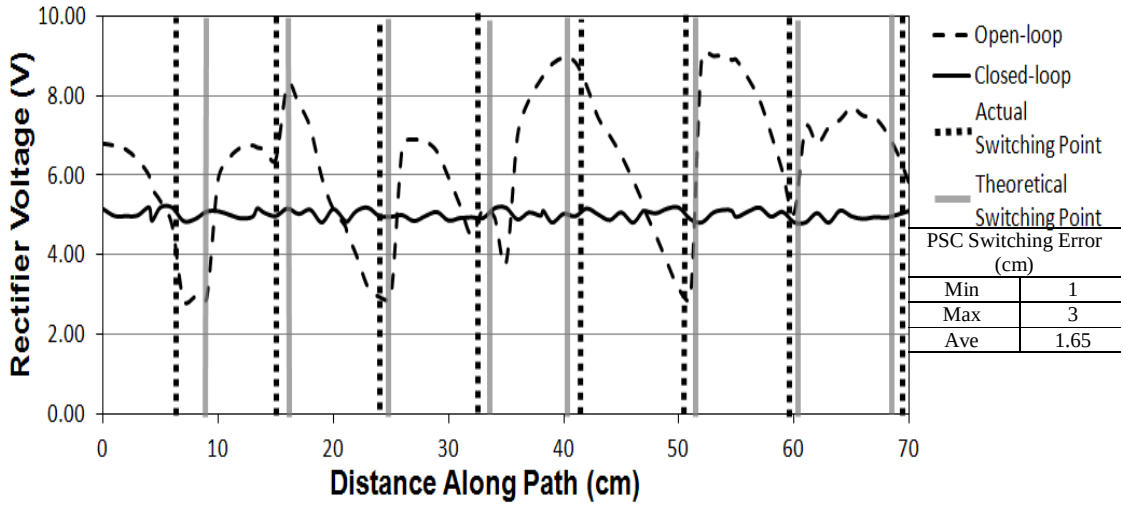

Figure 7.14: Theoretical and actual switching points between active PSCs and the resulting voltage at the output of the mobile unit rectifier when it is moved horizontally along the path shown in Figure 7.13 at the nominal height of 12 cm.

7.3.3 Animal Experiment

In order to demonstrate the functionality of the system, nine control modules (81 complete PSCs) were tested *in-vivo* in a 3 × 3 array, covering a total area of 5068 cm^2, as shown in Figure 7.11. Since the PSC arrangement is based on the PCB layout of Figure 7.8, the combined active area of the complete coils for the nine control modules is not rectangular. Hence, an approximate shape is used for the actual animal experiment as shown by the black boundary in Figure 7.15, and the size is 3538 cm^2 based on this boundary. In this cage, 66 PSCs are used, and some PSCs are cut off by the approximation.

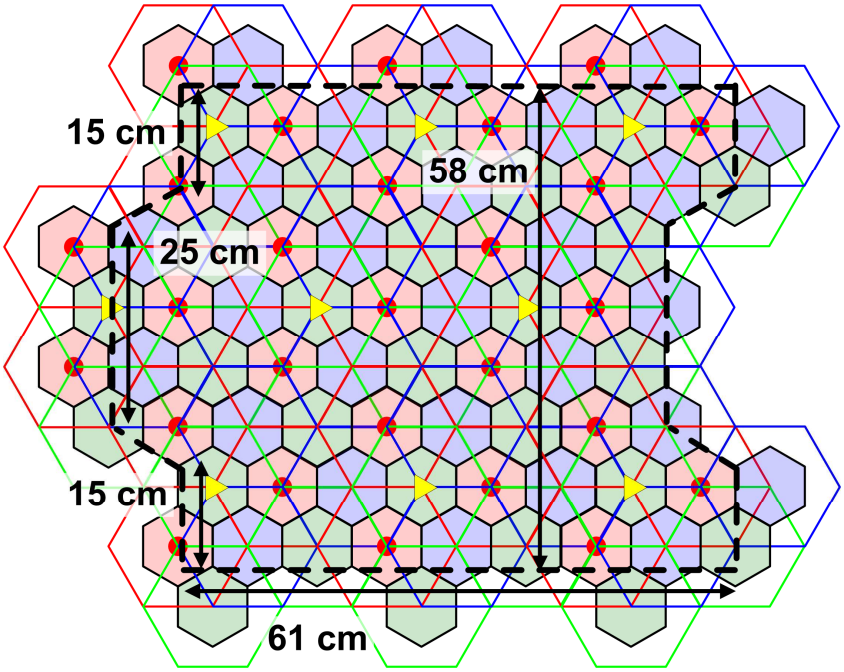

Figure 7.15: The boundary of the animal experiment for 3×3 control modules array.

In order to reduce the weight of the mobile unit for the animal experiment, Set-2 Rx coils are used. The specifications of the mobile unit coils are shown in Table 7.1. The animal subject is a 15-month-old Long-Evans Rat weighing 500g as shown in Fig. 7.16a. The fabricated mobile unit, the headstage, is shown in Figure 7.16b. The *in-vivo* experimental setup is shown in Figure 7.16c. The boundary of the experiment was maintained by the plastic glass cage, and the PSC array was covered with another sheet of plastic glass, which had a thickness of 1.5 mm. The maximum supply voltage for the PAs, VDD_Tx, was 18 V to provide a maximum of 3.5 W while the minimum VDD_Tx was 5 V to provide 0.5 W. The animal experiment was conducted for one hour without interruption, and the results are shown in Figure 7.17. In Figure 7.17a, the mobile unit voltage, V_{rec}, was almost constantly maintained at 4 V, a value set by the closed-loop power module.The PA supply voltage varied from 5 V to 18 V depending on the position,

coupling distance, and tilting angle variations of the headstage caused by the rat's movements

In Fig. 7.17a, some periods of interest are indicated, and the results of these time sections are expanded in Figs. 7.17b to 7.17d. In Fig. 7.17b (t= 5.5 min to t= 7.5 min), V_{rec} was decreasing while VDD_Tx could not reach 18 V due to back telemetry noise that was misguiding the power control algorithm. In Fig. 7.17c (t= 31.0 min to t= 33.5 min), V_{rec} increased above 4 V while VDD_Tx stayed at its minimum level of 5V because the coupling was strong. In Fig. 7.17d (t= 47.0 min to t= 55 min), although the VDD_Tx was at its highest value of 18V, V_{rec} started decreasing. There are two reasons for this phenomenon. First, the PTE was low due to misalignment between the Tx and Rx coils. Second, the PTE of the Tx PSCs was insufficient to produce the necessary power because of Tx PSC mismatch.

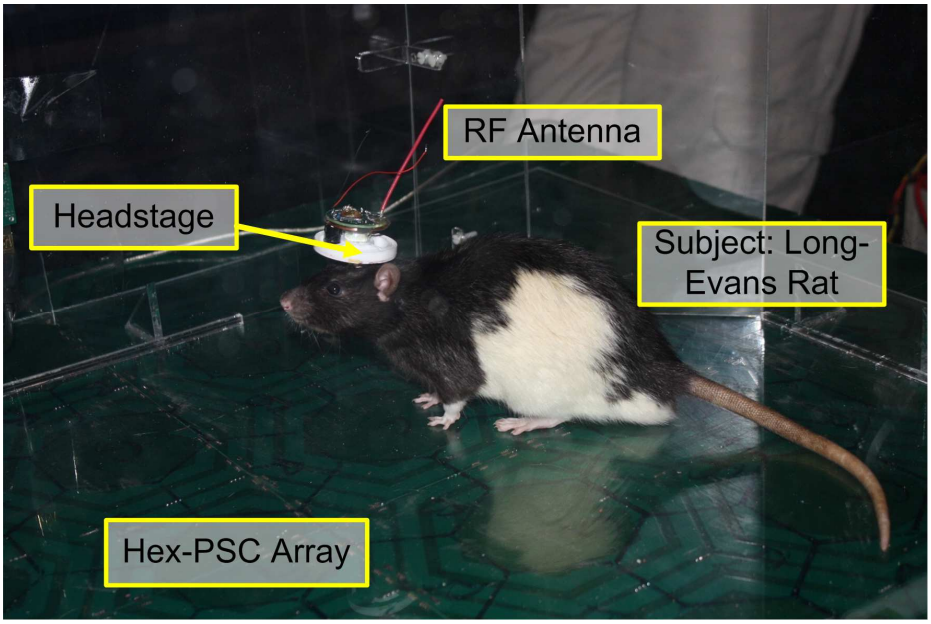

Figure 7.16. (a) The subject, Long-Evens rat, 15 month old. (b) The headstage for the animal experiment. (c) The setup for the animal experiment.

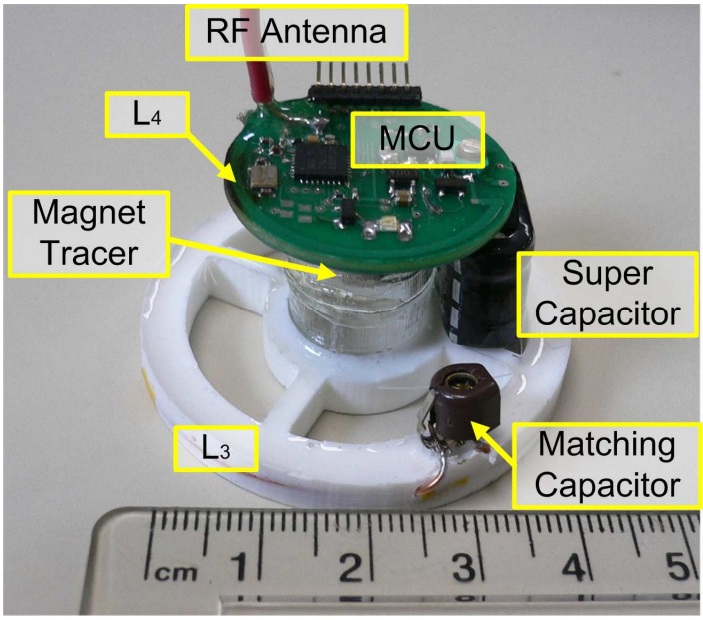

(b)

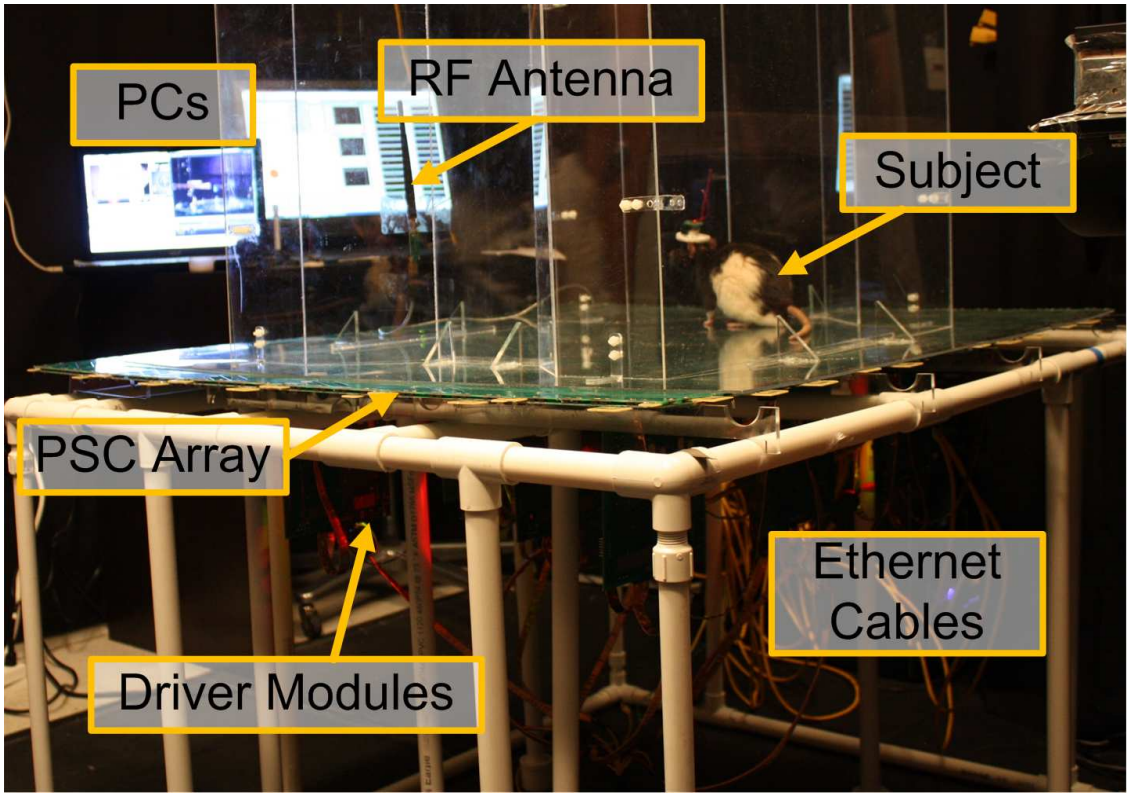

(c)

Figure 7.16: (b) The headstage for the animal experiment. (c) The setup for the animal experiment.

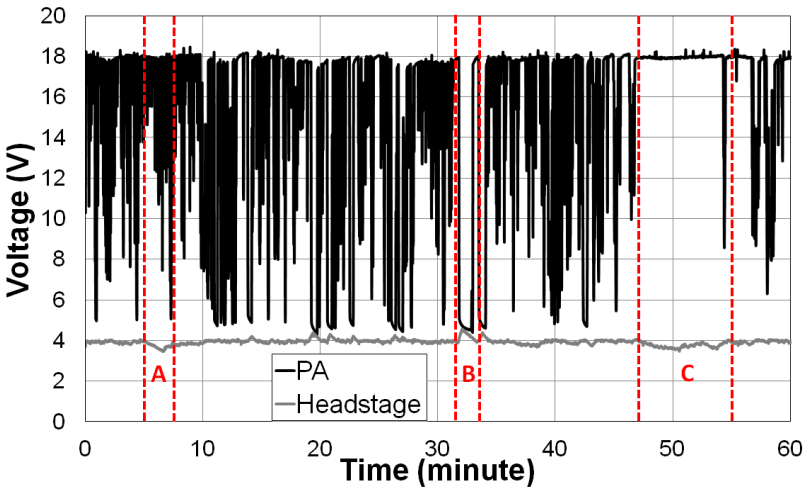

(a)

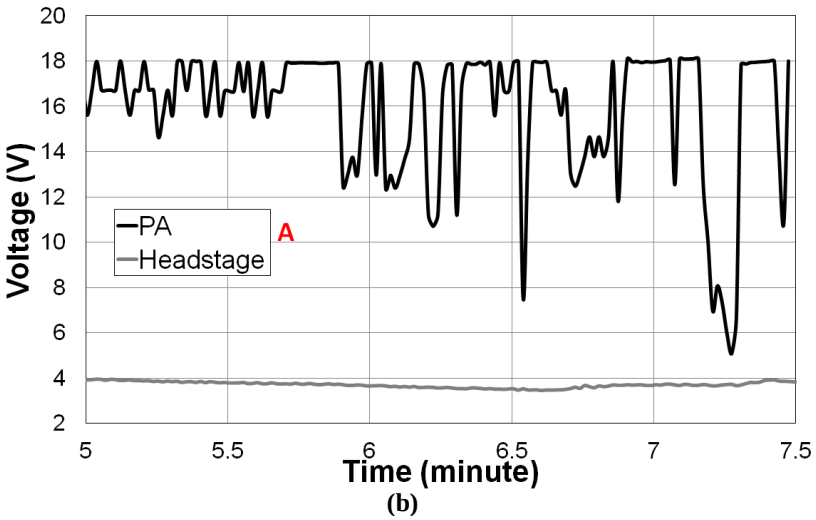

(b)

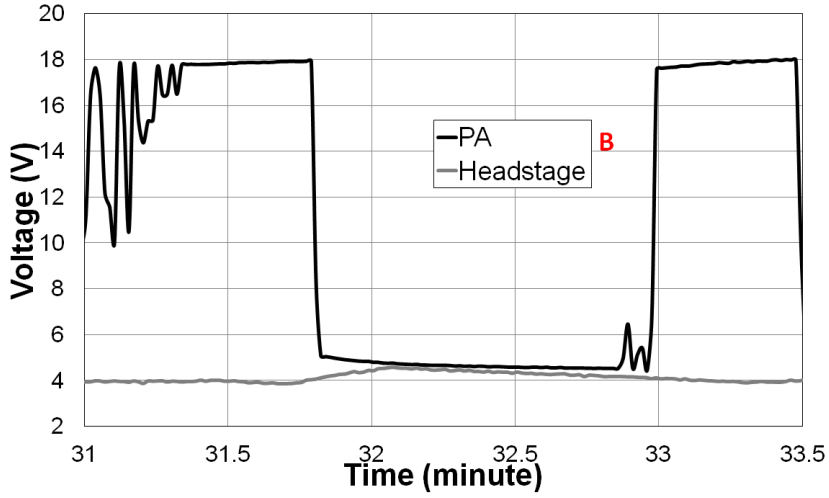

(c)

Figure 7.17: (a) *In-vivo* experimental results for headstage rectifier voltage and PA supply voltage during one hour. (b) Time period B: the noise of the Tx PSC affects CLPC control. (c) Time period B: The minimum output power of 0.5 W still provides the power for the headstage. d) Time period C: The PTE of the Tx PSCs is not enough to provide the sufficient power because of the mismatching problem of the Tx PSCs or the mobile unit is far from the Tx PSCs.

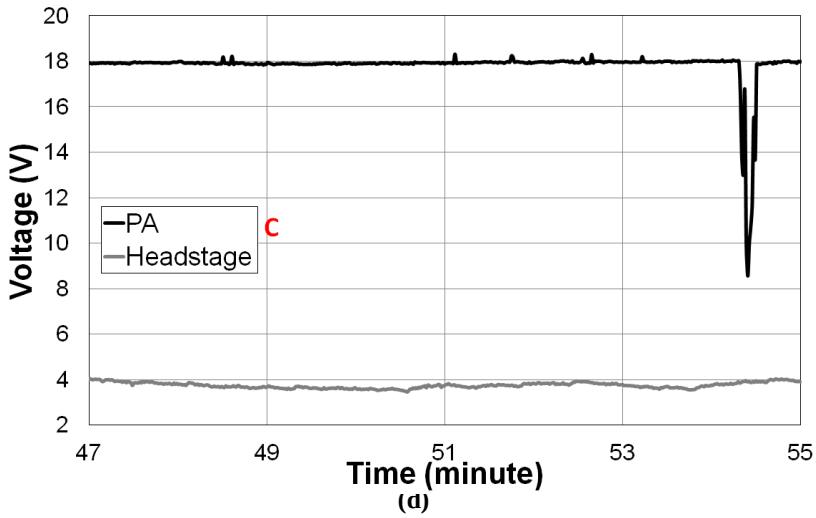

Figure 7.17: (d) Time period C: The PTE of the Tx PSCs is not enough to provide the sufficient power because of the mismatching problem of the Tx PSCs or the mobile unit is far from the Tx PSCs.

7.4 Conclusions

The EnerCage-1 system has demonstrated robust real time tracking as well as closed-loop power and back telemetry data transmission in bench top experiments. The use of multi-coil links and a threshold-based tracking algorithm have led to higher power transfer efficiency, and a reduction in the number of magnetic sensors and the amount of driver circuitry. *In vivo* experiments with small, freely behaving animal subjects show the capability of the system in an actual electrophysiology lab environment. However, there are still some issues that must be resolved, such as the relatively low accuracy of the magnetic sensor tracking and the poor impedance-matching of the PSC resonant frequency because of the parasitic effects from rat's body and the material of the cage.

CHAPTER VIII

CONCLUSIONS AND FUTURE WORKS

This dissertation focuses on developing the inductive coupling model and the optimization methodology used to achieve maximum power transfer efficiency (PTE) in a multi-carrier wireless link. Based on the models, the new multiband coil geometry obtains maximum PTE for the power carrier while minimizing interference in the data link. The second component of this dissertation is the development of a novel wireless biological data acquisition system called the EnerCage. This system can track the subject's location, provide localized wireless power, and transfer bidirectional data for unlimited time periods in experimental arenas of any size. The recent progress towards these projects is summarized in the first part of this chapter, followed by a discussion of future works.

8.1 Conclusions

This section summarizes the results and scientific contributions of the EnerCage and multiband wireless transmission systems.

8.1.1 Multiband Transmission for Implantable Devices

This project presents a novel, multiband wireless link with three major functions, namely power transfer, forward data transmission, and back telemetry, with a dedicated carrier signal and coil/antenna pair for each. The planar geometry of the coils and antennas is area efficient and enables subdermal implantation. Planar spiral coils (PSCs) are very effective for delivering wireless power via near-field transmission under the extreme size constraints imposed by next-generation neuroprosthetic devices. However,

these devices need to be hermetically sealed in biocompatible materials and placed in a conductive environment with high permittivity (tissue), and in the process, the PSC characteristics may be affected. To account for these changes, a detailed PSC model was constructed that incorporated the effects of the surrounding environment on the PSC parasitic components and the power transfer efficiency (PTE). This model was combined with an iterative design method that starts with a set of realistic design constraints and ends with the optimal PSC geometries. The PSC design procedure was validated by applying it to an exemplar 10×10 mm^2 visual prosthesis receiver coil, operating at 13.56 MHz. The finite element analysis models in HFSS were constructed for several fabricated PSC pairs on FR4. All calculation, simulation, and measurement results were in close agreement for each of the design parameters, and demonstrated the validity of the models and proposed iterative PSC design procedure as shown in Chapter 3. From the measurement results, the PSC which was optimized for transmission through air could only achieve 21.8% efficiency through muscle, demonstrating that accounting for environment in the design process can result in almost a 10% improvement in PTE.

The concept of the data link is addressed in Chapter 4, as well as the methodology for coil optimization and the detailed simulation and measurement results. Two different forward data coil designs were evaluated. The first consisted of a pair of vertical coils wound across the diameter of the power PSCs, which then produced magnetic fields that were orthogonal to those of the power carrier, and therefore less susceptible to noise. The second consisted of a pair of planar figure-8 coils, in which the electromotive force (EMF) induced by the power carrier in one loop, opposed that induced by the other loop. Therefore, the total EMF resulting from the power carrier interference when the coils are

perfectly aligned can theoretically be very small. The comparison of these designs is shown with respect to their robustness against the worst case horizontal misalignments. Finally, simulations and measurements of the performance of the data coils on a miniature spiral antenna receiver are conducted. This antenna was designed to operate with impulse-radio ultra wideband (IR-UWB) circuitry for back telemetry. The UWB antenna does not provide as wide a bandwidth as the commercial chip antenna, partly due to its implementation on a FR4 PCB. Therefore, more work is needed to develop IR-UWB antennas.

8.1.2 EnerCage

Wireless power and data transmission have opened up promising research opportunities by enabling perpetual data acquisition and stimulation systems. This project presents progress towards such a system, called the EnerCage, equipped with scalable arrays of overlapping planar spiral coils (PSC) and 3-axis magnetic sensors for focused wireless power transmission to freely behaving animal subjects. The EnerCage system includes a stationary unit for 3D non-line-of-sight localization and inductive power transmission through a geometrically optimized PSC array. The localization algorithm compares the magnetic sensor outputs with a threshold to determine which PSC to activate. The geometry of the coils is optimized for the scenario in which the mobile unit has achieved worst-case misalignment with a PSC, and considers parasitics from the overlapping and adjacent PSCs. The mobile unit is attached to or implanted in the subject's body, and includes a permanent magnetic tracer for localization, as well as a back telemetry circuit for efficient closed-loop inductive power regulation. The EnerCage system is designed to enable long-term electrophysiology experiments on small animal

subjects without requiring them to carry heavy and bulky batteries. For the preliminary EnerCage system, the closed-loop power management mechanism maintains the mobile unit received power at 20 mW despite misalignments, tilting, and distance variations up to a maximum operating height of 120 mm (PTE = 5%).

A design methodology is introduced for an overlapping hexagonal planar spiral coil (hex-PSC) array, optimized for the creation of a homogenous magnetic field. The modular hex-PSC array has been implemented with three parallel conductive layers, for which an iterative optimization procedure defines the PSC geometries. Since the overlapping hex-PSCs in different layers have different characteristics, the worst-case coil-coupling condition should be designed to provide the maximum PTE in order to minimize received power fluctuations.

However, there are some drawbacks of this design: the complexity of the metal pattern on layer 4 degrades the optimization result, the 2-coil coupling does not provide an optimal load for maximum PTE, and the central MCU cannot be used for multiple control modules. In the new revision, EnerCage-1, the layer 4 design was improved by moving some circuitry to the driver PCBs to reduce the overlapping area. The connection mechanism between the unit tiles is improved by standard headers that allow easy assembly of any desired experimental area as well as uniform performance of the connected PSCs. Each driver PCB is equipped with an Ethernet module for communication with the central PC, and the Rx is designed with multi-coil coupling to achieve maximum PTE. Moreover, the number of drivers and magnetic sensors is reduced in this version. The EnerCage-1 system has been tested in a one-hour *in vivo* experiment. The effectiveness of the closed-loop inductive power transmission and 3-D

non-line-of-sight magnetic tracking is apparent in the results, and the experiment demonstrates the feasibility of long-term uninterrupted electrophysiology experiments on small, freely behaving animal subjects in large experimental arenas.

8.2 Future Works

This dissertation has described a multiband coil and antenna design for implantable devices as well as a wireless power and data system for long-term animal experiments in large arenas. However, there are several issues that still need to be addressed, and the relevant future works are summarized in this section.

8.2.1 Multiband Wireless Link for Implantable Devices

For the multiband wireless link, only the power coil design incorporated the parasitic effects that exist as a result of implantation in the tissue, as shown in [7]. Most of the calculations, simulations, and measurement results were in close agreement within the range of parameters needed for neuroprosthetic applications. On the other hand, the data link was only modeled in air, and the deviation occurred when using tissue as the surrounding medium around the coils. Tissue increases the coils' parasitic capacitance and decreases their SRF and quality factors. Therefore, the optimal data coils' geometry for the tissue environment should be studied in the future.

For the UWB antennas, the design is only for air, and the measurement environment is also the air. It should be noted that at high frequencies, electromagnetic power absorption in the tissue can increase the antenna losses [125], and one should consider evaluating such antenna designs in saline and other tissue simulants [25]. Therefore, more work is needed to develop IR-UWB antennas not only the interference of the data and power coils but also the parasitics of the surrounding environment.

The coil design will be combined with real circuits (an integrated circuit) to have a complete system. GT-Bionics were introducing a new modulation technique, called Pulse Harmonic Modulation (PHM), for wideband, low power data transmission across inductive telemetry links that operate in the near-field domain. Using sharp and narrow pulses, similar to impulse-radio ultra wideband (IR-UWB) in the far-field, leads to significant reduction in the transmitter power consumption. GT-Bionics are now working on an integrated PHM-based transceiver, which is expected to push the uplink bandwidth and power consumption limits in IMD applications.

Furthermore, in order to miniaturize the module for implantable devices, the micromachining (MEMS) technology with smaller feature size will be used to further shrink the volume of the implantable multiband coil/antenna complex from the present work and conduct measurements in the real tissue environment. The MEMS also provide a flexible substrate, which provides the ability to conform to the body curvature. Moreover, the multiband coils with actual transceiver chip will be designed and tested to demonstrate the feasibility.

8.2.2 EnerCage

The project is for developing the necessary electronics, control algorithms, and graphical user interface software to drive the hex-PSC array in the form of a network under the control of a central PC base station. In the future, the EnerCage system can track animal's body, provide wireless power, and communicate with the electronics which will be combined with the neural recording circuits [127], stimulation circuits, and bio-sensors to provide *in vivo* electrophysiological data.

Furthermore, when the animal's body is close to the Tx-PSC, the tissues will

induce the parasitic capacitance of Tx PSCs and detune the resonant frequency [7] of the Tx coils. Hence, the next revision of the system can actively compensate for frequency variations of the carrier frequency, f_c. The closed-loop frequency control (CLFC) can also ensure a smooth power transfer to the headstage or implant. In short, by significantly improving the quality and quantity of medical interventions and monitoring of small feely behaving animal subjects while reducing alterations to their natural habitat, the EnerCage system is expected to enable new electrophysiology experiments that are not possible with today's technology.

For the animal tracking, the simple threshold-based algorithm [21] cannot show the animal behavior and accurate position. The magnetic sensor tracking should be improved to track accurate 3D position/orientation of a magnetic tracer [18] in the receiver (Rx) module. In the future, an accurate animal tracking mechanism using a combination of optical and magnetic sensors can provide researchers with real time information about not only the subjects' positions within the experimental arena but also their body gesture and head orientations, and this information can be used in behavioral analysis. Optical sensors such as a camera [24] require the subject to remain in the sensor's line-of-sight, and their resolution degrades when the coverage area increases, so an array of 3-axial magnetic sensors [25] that covers the bottom of the EnerCage tracks the magnetic tracer embedded in the IDPM unit. This sensing mechanism can operate in both open and covered spaces, which is a more natural environment for burrowing species, such as rodents. The data from a real time animal tracking algorithm will also be used to activate the hex-PSC that is in the best position to power the mobile unit.

There are many experiments that require collecting real-time biological information, such as neural signals, body temperature, blood pressure, physical activities,

blood chemical concentrations such as SpO2, NO, and neurotransmitters. Even more challenging is experiments that require applying uninterrupted electrical, chemical, or mechanical stimulation, which are more power consuming, over long periods of time. In order to solve the existing problems, EnerCage offers these functions: wireless power induction, data acquisition, command transmission, and precise tracking. This combination provides a comprehensive solution for broad fields of research from behavioral neuroscience on rats to genetic engineering and phenotyping of knockout mice in environmental enrichment.

APPENDIX A

MODEL OF THE VERTICAL COIL

Rectangular coils' self inductance, L, is calculated from the following equation by substituting data coil geometries, and the unit of the length is centimeter.

$$L = 0.008 N_d^2 \frac{l_d h_d}{w_d}\left\{\frac{1}{2}\frac{w_d}{h_d}\sinh^{-1}\frac{l_d}{w_d}+\frac{1}{2}\frac{w_d}{l_d}\sinh^{-1}\frac{h_d}{w_d}\right. \tag{9.1}$$

$$-\frac{1}{2}\left(1-\frac{h_d^2}{w_d^2}\right)\frac{w_d}{l_d}\sinh^{-1}\frac{l_d}{w_d\sqrt{1+h_d^2/{w_d}^2}}$$

$$-\frac{1}{2}\left(1-\frac{l_d^2}{w_d^2}\right)\frac{w_d}{l_d}\sinh^{-1}\frac{h_d}{w_d\sqrt{1+l_d^2/w_d^2}}-\frac{1}{2}\frac{h_d}{w_d}\sinh^{-1}\frac{l_d}{h_d}$$

$$-\frac{1}{2}\frac{l_d}{w_d}\sinh^{-1}\frac{h_d}{l_d}+\left(\frac{\pi}{2}-\tan^{-1}\frac{l_d h_d}{w_d^2\sqrt{1+g^2/w_d^2}}\right)$$

$$+\frac{1}{3}\frac{w_d^2}{l_d h_d}\left[\sqrt{1+\frac{g^2}{w_d^2}}\left(1-\frac{1}{2}\frac{g^2}{w_d^2}\right)+1-\sqrt{1+\frac{l_d^2}{w_d^2}}\left(1-\frac{1}{2}\frac{l_d^2}{w_d^2}\right)\right.$$

$$\left.\left.-\sqrt{1+\frac{h_d^2}{w_d^2}}\left(1-\frac{1}{2}\frac{h_d^2}{w_d^2}\right)\right]+\frac{1}{6}\frac{w_d}{l_d h_d}\frac{g^3-l_d^3-h_d^3}{w_d^2}\right\}$$

in μH, where $g^2 = l_d^2 + w_d^2$.

Mutual inductance between a pair of rectangular solenoids is calculated by making adjustments in the circular solenoid equations from [121],

$$M = 0.001(A_3)(A_4)\frac{N_3}{W_{d3}}\cdot\frac{N_4}{W_{d4}}\cdot\left[\frac{Z_1}{r_1}-\frac{Z_2}{r_2}-\frac{Z_3}{r_3}+\frac{Z_4}{r_4}\right] \tag{9.2}$$

where

$A_3 = (l_{d3}\cdot h_{d3})$, $A_4 = (l_{d4}\cdot h_{d4})$, and

$$Z_m = T_2 t_2 - \frac{1}{4}\frac{h_{d3}^2}{r_m^2}\left(T_4 t_2 + \frac{h_{d4}^2}{h_{d3}^2} T_2 t_4\right) P_2(\mu_m)$$

$$+ \frac{1}{8}\frac{h_{d3}^4}{r_m^4}\left(T_6 t_2 + 3\frac{h_{d4}^2}{h_{d3}^2} T_4 t_4 + \frac{h_{d4}^4}{h_{d3}^4} T_2 t_6\right) P_4(\mu_m)$$

$$- \frac{5}{64}\frac{h_{d3}^6}{r_m^6}\begin{pmatrix} T_8 t_2 + 6\frac{h_{d4}^2}{h_{d3}^2} T_6 t_4 \\ + 6\frac{h_{d4}^4}{h_{d3}^4} T_4 t_6 + \frac{h_{d4}^6}{h_{d3}^6} T_2 t_8 \end{pmatrix} P_6(\mu_m)$$

$$+ \frac{7}{128}\frac{h_{d3}^8}{r_m^8}\begin{pmatrix} T_{10} t_2 + 10\frac{h_{d4}^2}{h_{d3}^2} T_8 t_4 + 20\frac{h_{d4}^4}{h_{d3}^4} T_6 t_6 \\ + 10\frac{h_{d4}^6}{h_{d3}^6} T_4 t_8 + \frac{h_{d4}^8}{h_{d3}^8} T_2 t_{10} \end{pmatrix} P_8(\mu_m) + \ldots$$

in μH. The four radii vectors, r_m (m = 1 to 4), are dependent on the four distances, d_m, given by

$$r_m = \sqrt{d_m^2 + (D + h_{d3}/2 + h_{d4}/2)^2},$$

$$d_1 = \Delta X - \left(\frac{W_{d4} + W_{d3}}{2}\right),\ d_2 = \Delta X + \left(\frac{W_{d4} - W_{d3}}{2}\right),$$

$$d_3 = \Delta X + \left(\frac{W_{d3} - W_{d4}}{2}\right),\ d_4 = \Delta X + \left(\frac{W_{d3} + W_{d4}}{2}\right).$$

$\mu_m = d_m / r_m$, and $P_{2n}(\mu_m)$ (n is positive integer) are known as zonal harmonics, given by [121],

$$P_{2n}(\mu_m) = \frac{(2\cdot 2n-1)(2\cdot 2n-3)\ldots 1}{(2n)!}\left[\mu_m^{2n} - \frac{2n(2n-1)}{2(2\cdot 2n-1)}\mu_m^{2n-2} + \frac{2n(2n-1)(2n-2)(2n-3)}{2\cdot 4(2\cdot 2n-1)(2\cdot 2n-3)}\mu_m^{2n-4} - \ldots\right] \quad (9.3)$$

T_2 and t_2 are function of $Dia_3^2/(h_{d3}/2)^2$ and $Dia_4^2/(h_{d4}/2)^2$, respectively, and the same is true for T_4 and t_4, T_6 and t_6, so on and so forth. The coefficients t_2, t_4, t_6, … or T_2, T_4, T_6, … are functions of the ratio, τ, of the height of the coil (h_d) and its mean wire diameter (Dia);

For the external coil, L_3 (T_n), $\tau_{ex}^{\ 2} = \dfrac{Dia_3^{\ 2}}{(h_{d3}/2)^2}$

For internal coil, L_4 (t_n), $\tau_{in}^{\ 2} = \dfrac{Dia_4^{\ 2}}{(h_{d4}/2)^2}$

$$T_n \text{ or } t_n = 1 + \frac{n(n-1)}{3!}\frac{\tau^2}{2^2} + \frac{n(n-1)(n-3)}{5!}\frac{\tau^4}{2^4} + \ldots + \frac{n(n-1)(n-3)\ldots[n-(n-1)]}{(n+1)!}\frac{\tau^n}{2^n}$$

Finally, by substituting L and M from the above equations in (4.1), k_{34} can be found.

APPENDIX B

MODEL OF OVERLAPPING COIL

The circuit model for the hex-PSCs should include the key parasitic effects of mutual inductance (M), mutual capacitance (C_M, which includes both C_{ov} and C_{adj}), and mutual resistance, (R_M, which includes both R_{ov} and R_{adj}) among overlapping coils. Figure 6.2g shows the worst-case condition in terms of parasitic effects: the black central PSC in layer 2 is overlapped by six PSCs in layers 1 and 3 and surrounded by six other adjacent PSCs in layer-2. Since considering the parasitic effects among all 13 PSCs renders the model too complicated, only the mutual parasitic effects between every two PSCs are considered. In this simplified model, every two PSCs are either overlapping or adjacent, as shown in Figs. 4a and 4b, respectively.

Considering that the hex-PSCs are implemented in three different layers, shown in Figure 6.2f, their mutual parasitics can be divided into 4 categories that are summarized in Table 10.1. M_{ov12}, C_{ov12}, and R_{ov12} represent parasitics between PSCs in 1ayers 1 and 2; M_{ov23}, C_{ov23}, and R_{ov23} represent parasitics between 1ayers 2 and 3; M_{ov13}, C_{ov13}, and R_{ov13} represent parasitics between 1ayers 1 and 3; and finally M_{adj}, C_{adj}, and R_{adj} represent parasitics between adjacent PSCs in each layer.

Parasitic mutual capacitances can be calculated from,

$$C_{ov11} = \frac{A_{ov}\varepsilon_0}{2}\frac{\varepsilon_{rs\_eff}}{t_s}, \tag{10.1}$$

$$C_{ov23} = \frac{A_{ov}\varepsilon_0}{2}\frac{1}{t_{air}}, \tag{10.2}$$

$$C_{ov13} = \frac{A_{ov}\varepsilon_0}{2}\frac{\varepsilon_{rs\_eff}}{\varepsilon_{rs\_eff}\cdot t_{air} + t_s}, \tag{10.3}$$

where ε_{rs_eff} is the effective dielectric constant for FR4, including the fringing effects [112]. The overlapping area can be found from

$$A_{ov} = 2\times\left(\frac{2w}{\sqrt{3}}w\right)\times n_1^2, \tag{10.4}$$

where w is the width of the hex-PSC metal trace and n_1 is the number of turns.

Table 8.1. MUTUAL PARASITIC COMPONENTS

Type	Value	k	D	γ	Area*
M_{ov12} C_{ov12} R_{ov12}	131 nH 8.99 pF 78.2 kΩ	0.1147	t_{sub} = 1.6 mm (1ayer-1 and 2)	$r_{01}+\frac{s_{adj}}{\sqrt{3}}$	A_{ov}
M_{ov23} C_{ov23} R_{ov23}	131 nH 8.43 pF 1 GΩ**	0.1146	t_{air} = 1.7 mm (1ayer-2 and 3)	$r + s_{adj}$	A_{ov}
M_{ov13} C_{ov13} R_{ov13}	128 nH 0.95 pF 1 GΩ	0.1125	t_{air}+t_{sub} = 3.3 mm (1ayer-1 and 3)	$r + s_{adj}$	A_{ov}
M_{adj} C_{adj} R_{adj}	99 nH 0.03 pF 245 kΩ	0.0868	0 (same layer)	$\frac{2\sqrt{3}}{r_{o1}+S_{adj}}$	$r_{o1}\times t_0$

*Overlapping areas between two conductors
**Air dielectric loss is close to zero. Thus parasitic resistance was set to 1 GΩ.

Regarding C_{adj}, the two adjacent hex-PSC traces as a coplanar stripline between FR4 and air can be considered. Then the unit length parasitic capacitance can be expressed as [112],

$$C_{adj\_unit} = \varepsilon_0\frac{K(k_0')}{K(k_0)}\cdot\varepsilon_{r\_eff}, \tag{10.5}$$

where $K(k_0)$ is the complete elliptic integral of the first kind, ε_{rs} is the relative dielectric constant of the substrate (FR4), and

$$k_0 = \frac{S_{adj}}{S_{adj}+2w},\ k_0' = \sqrt{1-k_0^2}, \tag{10.6}$$

$$\varepsilon_{r\_eff} = 1 + \frac{1}{2}(\varepsilon_{rs} - 1)\frac{K(k_0)K(k_1')}{K(k_0')K(k_1)}, \tag{10.7}$$

$$k_1 = \frac{\tanh(\pi s_{adj} / 4t_s)}{\tanh[\pi(s_{adj} + 2w)/4t_s]}, \; k_1' = \sqrt{1 - k_1^2}\,. \tag{10.8}$$

Therefore, $C_{adj} = C_{adj\_unit} \times r_{o1}$.

The mutual resistance, R_M, which includes R_{ov} and R_{adj}, results from the material loss, which is related to the capacitance and the material dielectric loss [6]. Hence, R_{ov} and R_{adj}, can be found from,

$$R_{ov}(\text{or } R_{adj}) = \frac{1}{2\pi f \cdot \tan(\delta) \cdot C_{ov}(\text{or } C_{ajdv})}. \tag{10.9}$$

Note that R_{ov3} is set to 1 GΩ (effectively infinite) since one of the dielectric materials between layers 1 and 3 is air, which has an extremely low dielectric loss.

From these equations, three 13×13 matrixes for M, C_M, and, R_M can be derived. Tables 10.2 and 10.3 show the matrixes for M and C_M, respectively. The matrix for R_M can be derived from the C_M matrix using (10.9). These matrixes were then entered in Simulink (Mathwork, Natick, MA) to construct an equivalent circuit model with lumped parasitic components, shown in Figure 6.3, for the layer 2 hex-PSC in Figure 6.2g that shows the worst-case parasitic effects.

Table 8.2. MUTUAL COUPLING INDUCTANCE

Name of PSC	**L-1**	**L-1_1**	**L-1_2**	**L-1_3**	**L-1_4**	**L-1_5**	**L-1_6**	**L-1_7**	**L-1_8**	**L-1_9**	**L-1_10**	**L-1_11**	**L-1_12**
L-1	1	M_{ov1}	M_{ov1}	M_{ov1}	M_{ov2}	M_{ov2}	M_{ov2}	M_{adj}	M_{adj}	M_{adj}	M_{adj}	M_{adj}	M_{adj}
L-1_1	M_{ov1}	1	M_{adj}	M_{adj}	M_{ov3}	M_{ov3}	0	M_{ov1}	M_{ov1}	0	0	0	0
L-1_2	M_{ov1}	M_{adj}	1	M_{adj}	0	M_{ov3}	M_{ov3}	0	0	M_{ov1}	M_{ov1}	0	0
L-1_3	M_{ov1}	M_{adj}	M_{adj}	1	M_{ov3}	0	M_{ov3}	0	0	0	0	M_{ov1}	M_{ov1}
L-1_4	M_{ov2}	M_{ov3}	0	M_{ov3}	1	M_{adj}	M_{adj}	M_{ov2}	0	0	0	0	M_{ov2}
L-1_5	M_{ov2}	M_{ov3}	M_{ov3}	0	M_{adj}	1	M_{adj}	0	M_{ov2}	M_{ov2}	0	0	0
L-1_6	M_{ov2}	0	M_{ov3}	M_{ov3}	M_{adj}	M_{adj}	1	0	0	0	M_{ov2}	M_{ov2}	0
L-1_7	M_{adj}	M_{ov1}	0	0	M_{ov2}	0	0	1	M_{adj}	0	0	0	M_{adj}
L-1_8	M_{adj}	M_{ov1}	0	0	0	M_{ov2}	0	M_{adj}	1	M_{adj}	0	0	0
L-1_9	M_{adj}	0	M_{ov1}	0	0	M_{ov2}	0	0	M_{adj}	1	M_{adj}	0	0
L-1_10	M_{adj}	0	M_{ov1}	0	0	0	M_{ov2}	0	0	M_{adj}	1	M_{adj}	0
L-1_11	M_{adj}	0	0	M_{ov1}	0	0	M_{ov2}	0	0	0	M_{adj}	1	M_{adj}
L-1_12	M_{adj}	0	0	M_{ov1}	M_{ov2}	0	0	M_{adj}	0	0	0	M_{adj}	1

Table 8.3. MUTUAL COUPLING CAPACITANCE

Name of PSC	**L-1**	**L-1_1**	**L-1_2**	**L-1_3**	**L-1_4**	**L-1_5**	**L-1_6**	**L-1_7**	**L-1_8**	**L-1_9**	**L-1_10**	**L-1_11**	**L-1_12**
L-1	1	C_{ov1}	C_{ov1}	C_{ov1}	C_{ov2}	C_{ov2}	C_{ov2}	C_{adj}	C_{adj}	C_{adj}	C_{adj}	C_{adj}	C_{adj}
L-1_1	C_{ov1}	1	C_{adj}	C_{adj}	C_{ov3}	C_{ov3}	0	C_{ov1}	C_{ov1}	0	0	0	0
L-1_2	C_{ov1}	C_{adj}	1	C_{adj}	0	C_{ov3}	C_{ov3}	0	0	C_{ov1}	C_{ov1}	0	0
L-1_3	C_{ov1}	C_{adj}	C_{adj}	1	C_{ov3}	0	C_{ov3}	0	0	0	0	C_{ov1}	C_{ov1}
L-1_4	C_{ov2}	C_{ov3}	0	C_{ov3}	1	C_{adj}	C_{adj}	C_{ov2}	0	0	0	0	C_{ov2}
L-1_5	C_{ov2}	C_{ov3}	C_{ov3}	0	C_{adj}	1	C_{adj}	0	C_{ov2}	C_{ov2}	0	0	0
L-1_6	C_{ov2}	0	C_{ov3}	C_{ov3}	C_{adj}	C_{adj}	1	0	0	0	C_{ov2}	C_{ov2}	0
L-1_7	C_{adj}	C_{ov1}	0	0	C_{ov2}	0	0	1	C_{adj}	0	0	0	C_{adj}
L-1_8	C_{adj}	C_{ov1}	0	0	0	C_{ov2}	0	C_{adj}	1	C_{adj}	0	0	0
L-1_9	C_{adj}	0	C_{ov1}	0	0	C_{ov2}	0	0	C_{adj}	1	C_{adj}	0	0
L-1_10	C_{adj}	0	C_{ov1}	0	0	0	C_{ov2}	0	0	C_{adj}	1	C_{adj}	0
L-1_11	C_{adj}	0	0	C_{ov1}	0	0	C_{ov2}	0	0	0	C_{adj}	1	C_{adj}
L-1_12	C_{adj}	0	0	C_{ov1}	C_{ov2}	0	0	C_{adj}	0	0	0	C_{adj}	1

REFERENCES

[1] G. M. Clark, *Cochlear Implants: Fundamentals and Applications*, New York, NY: Springer, 2003.

[2] U. Jow and M. Ghovanloo, "Optimization of a multiband wireless link for neuroprosthetic implantable devices," *Proc. IEEE Biomed. Circuits and Systems*, pp. 97-100, Nov. 2008.

[3] U. Jow and M. Ghovanloo, "Optimization of data coils in a multiband wireless link for neuroprosthetic implantable devices," *IEEE Trans. on Biomed. Circuits and Systems*, vol.4, no.5, pp. 301-310, Oct. 2010.

[4] U. Jow and M. Ghovanloo, "Design and optimization of printed spiral coils for efficient inductive power transmission," *Proc. IEEE Intl. Conf. Elec., Circuits and Systems*, pp. 70-73, Dec. 2007.

[5] U. Jow and M. Ghovanloo, "Design and optimization of printed spiral coils for efficient transcutaneous inductive power transmission," *IEEE Trans. on Biomed. Circuits and Systems*, vol. 1, no. 3, pp. 193-202, Sept. 2007.

[6] U. Jow and M. Ghovanloo, "Modeling and optimization of printed spiral coils in air, saline, and muscle tissue environments," *IEEE Trans. on Biomed. Circuits and Systems*, vol. 3, no. 5, pp. 339-347, Oct. 2009.

[7] U. Jow and M. Ghovanloo, 'Modeling and optimization of printed spiral coils in air and muscle tissue environments," *Proc. IEEE 31sth Eng. in Med. and Biol. Conf.*, pp. 6387-6390, Sept. 2009.

[8] F. T. Abu-Nimeh, A. Kamboh, M. Aghagolzadeh, U. Jow, A. Mason, M. Ghovanloo, and L. Oweiss, “A highly modular, wireless, implantable interface to the cortex,” *Proc. IEEE 31sth Eng. in Med. and Biol. Conf.*, pp. 375-378, Sept. 2009.

[9] M. Ghovanloo and S. Atluri, “A wide-band power-efficient inductive wireless link for implantable microelectronic devices using multiple carriers,” *IEEE Trans. Circuits and Systems I*, vol. 54, no. 10, pp. 2211-2221, Oct. 2007.

[10] T. Takura, T. Somekawa, F. Sato, H. Matsuki, and T. Sato, “Improvement of communication area for implantable signal transmission system with ferrite chip core,” *J. Appl. Phys.*, vol. 99, pp. 08R909, Apr. 2006.

[11] T. Dissanayake, M. R. Yuce, and C. K. Ho, “Design and evaluation of a compact antenna for implant-to-air UWB communication,” *IEEE Antennas Wireless Propag. Lett*., vol. 8, pp. 153–156, Apr. 2009.

[12] M. Yin and M. Ghovanloo, “Using pulse width modulation for wireless transmission of neural signals in multichannel neural recording systems,” *IEEE Trans. on Neural Sys. Rehab. Eng.*, vol. 17, no. 4, pp. 354-363, Aug. 2009.

[13] J. P. Donoghue, “Bridging the brain to the world: a perspective on neural interface systems,” *Neuron*, vol. 60, no.3, pp. 511-521, Nov. 2008.

[14] R. R. Harrison, R. J. Kier, C. A. Chestek, V. Gilja, P. Nuyujukian, S. Ryu, B. Greger, F. Solzbacher, and K. V. Shenoy, “Wireless neural recording with single low-power integrated circuit,” *IEEE Trans. Neural Syst. Rehab. Eng.*, vol. 17, no.4, pp. 322-329, Aug. 2009.

[15] A. B. Schwartz, X. T. Cui, D. J. Weber, and D. W. Moran, “Brain-controlled interfaces: movement restoration with neural prosthetics,” *Neuron*, vol. 52, no. 1, pp. 205-220, Oct. 2006.

[16] H. Miranda, V. Gilja, C. A. Chestek, K. V. Shenoy, and T. H. Meng, “HermesD: a high-rate long-range wireless transmission system for simultaneous multichannel neural recording applications,” *IEEE Trans. on Biomed. Circuits and Systems*, vol. 4, no. 3, pp. 181-191, June 2010.

[17] J. Yamamoto and M. A. Wilson, “Large-scale chronically implantable precision motorized microdrive array for freely behaving animals,” *J. Neurophysiol*, 100, pp. 2430–2440, July 2008.

[18] C. Cheng, X. Huo, and M. Ghovanloo, “Towards a magnetic localization system for 3-D tracking of tongue movements in speech-language therapy,” *IEEE Eng. in Med. and Biol. Conf.*, pp. 563-566, Sept. 2009.

[19] P. McMenamin, U. Jow, M. Kiani, and M. Ghovanloo, “Real Time Control of a Wireless Powering and Tracking System for Long-Term and Large-Area Electrophysiology Experiments,” *IEEE Biomed. Circ. Sys. Conf.*, Nov. 2012.

[20] U. Jow, M. Kiani, X. Huo, and M. Ghovanloo, “Towards a smart experimental arena for long-term electrophysiology experiments,” *IEEE Biomed. Circ. Sys. Conf.*, pp.121–124, Nov. 2011.

[21] U. Jow, M. Kiani, X. Huo, and M. Ghovanloo, “Towards a smart experimental arena for long-term electrophysiology experiments,” *IEEE Trans. on Biomed. Circuits and Systems*, accepted for publication.

[22] M. Ghovanloo, “Systems and methods for providing wireless power to a protable unit,” U.S. Patent Application 20110074349, May 28, 2009.

[23] U. Jow and M. Ghovanloo, “Geometrical design of a scalable overlapping planar spiral coil array to generate a homogeneous magnetic field,” *IEEE Trans. Magnetics,* submitted for publication.

[24] R. R. Harrison, P. T. Watkins, R. J. Kier, R. O. Lovejoy, D. J. Black, B. Greger, and F. Solzbacher, “A low-power integrated circuit for a wireless 100-electrode neural recording system,” *IEEE J. Solid-State Circuits*, vol. 42, no. 1, pp. 123–133, Jan. 2007.

[25] M. S. Humayun, J. D. Weilanda, G. Y. Fujiia, R. Greenbergb, R. Williamsonb, J. Littleb, B. Mechb, V. Cimmarustib, G.V. Boemela, G. Dagneliec, and E. de Juan, Jr., “Visual perception in a blind subject with a chronic microelectronic retinal prosthesis,” *Vision Research*, vol. 43, pp. 2573-2581, Nov. 2003.

[26] J. D. Weiland, W. Liu, and M. S. Humayun, “Retinal Prosthesis,” *Annual Review of Biomedical Eng.*, vol. 7, pp. 361-401, 2005.

[27] S. Gabriel, R. W. Lau, and C. Gabriel, “The dielectric properties of biological tissues: II. Measurements in the frequency range 10 Hz to 20 GHz,” *Phys. Med. Biol.*, vol. 41, pp. 2251-2269, Nov. 1996.

[28] V. Singh, A. Qusba, A. Roy, R. A. Castro, K. McClure, R. Dai, R. J. Greenberg, J. D. Weiland, M. S. Humayun, and G. Lazzi, “Specific absorption rate and current densities in the human eye and head induced by the telemetry link of a retinal prosthesis,” *IEEE Trans. Ant. Propagation*, vol. 57, no. 10, pp. 3110–3118, Oct. 2009.

[29] J. Kim, D. Oh, J. Yoon, S. Cho, N. Kim, J. Cho, Y. Kwon, C. Cheon, and Y. Kim, "In vitro and in vivo measurement for biological applications using micromachined probe," *IEEE Trans. Microwave Theory Tech.*, vol. 53, Issue 11, pp. 3415-3421, Nov. 2005.

[30] S. Ozeria, D. Shmilovitza, S. Singera, and C.-C. Wang, "Ultrasonic transcutaneous energy transfer using a continuous wave 650 kHz Gaussian shaded transmitter," *Ultrasonics*, vol. 50, Issue 7, pp. 666-674, June 2010.

[31] S. Ozeria and D. Shmilovitz, "Ultrasonic transcutaneous energy transfer for powering implanted devices," *Ultrasonics*, vol. 50, Issue 6, pp. 556-566, May 2010.

[32] T. Ishiyama, Y. Kanai, J. Ohwaki, and M. Mino, "Impact of a wireless power transmission system using an ultrasonic air transducer for low-power mobile applications." *IEEE Ultrasonics Symposium*, vol. 2, pp.1368–1371, Oct. 2003.

[33] Y. Zhu, S. O. R. Moheimani, and M. R. Yuce, "Ultrasonic energy transmission and Conversion Using a 2-D MEMS Resonator," *IEEE Electron Device Letters*, vol. 31, no.4, pp. 374-376, Apr. 2010.

[34] A. Denisov and E. Yeatman, "Ultrasonic vs. inductive power delivery for miniature biomedical implants," *International Conference on Body Sensor Networks*, pp. 84-89, June 2010.

[35] W. C. Brown, "The history of power transmission by radio waves," *IEEE Trans. Microwave Theory Tech.*, vol. 32, no. 9, pp. 1230–1242, Sept. 1984.

[36] K. Finkenzeller, *RFID Handbook: Fundamentals and Applications in Contactless Smart Cards and Identification 2nd Ed*. John Wiley & Sons, Ltd. 2003.

[37] Powercast, [Online], Available: http://www.powercastco.com/

[38] Powerbeam, [Online], http://www.powerbeaminc.com/

[39] J.-P. Curty, N. Joehl, C. Dehollain, and M. J. Declercq, "Remotely powered addressable UHF RFID integrated system", *IEEE J. of Solid-State Circuits*, vol. 40, no. 11, pp. 2193-2202, Nov. 2005.

[40] Y.-H. Suh and K. Chang, "A high-efficiency dual-frequency rectenna for 2.45- and 5.8-GHz wireless power transmission," *IEEE Trans. Microwave Theory Tech.*, vol. 50, no. 7, pp. 1784–1789, July 2002.

[41] A. S. Y. Poon, S. O'Driscoll, and T. H. Meng, "Optimal frequency for wireless power transmission into dispersive tissue," *IEEE Trans. on Antennas and Propagation*, vol. 58, no. 5, pp. 1739-1750, May 2010.

[42] N. Tesla, "Apparatus for transmitting electrical energy," US Patent 1,119,732, Dec. 1, 1914.

[43] J. M. Fernandez, and J. A. Borras, "Contactless battery charger with wireless control link," US Patent 6,184,651, Feb. 6, 2001.

[44] J. Hirai, T.-W. Kim, and A. Kawamura, "Study on intelligent battery charging using inductive transmission of power and information," *IEEE Trans. on Power Electronics*, vol.15, no.2, pp. 335-345, Mar. 2000.

[45] A. Kurs, A. Karalis, R. Moffatt, J. D. Joannopoulos, P. Fisher, and M. Soljacic," Wireless power transfer via strongly coupled magnetic resonances," *Science*, vol. 317, pp. 83–86, July 2007.

[46] A. Karalis, J. D. Joannopoulos, and M. Soljacic, "Efficient wireless nonradiative mid-range energy transfer," *Ann. Phys.*, vol. 323, no. 1, pp. 34–48, Jan. 2008.

[47] Wireless Power Consortium, Qi standard, [Online]. Available: http://www.wirelesspowerconsortium.com/

[48] Wildcharge, [Online]. http://www.shoppureenergy.com/

[49] eCoupled:, [Online]. http://ecoupled.com/

[50] Splashpower.[Online]. http://splashpower.com/

[51] WiTricity, [Online]. http://www.witricity.com/

[52] Ndigo,[Online]. http://www.ndigobusiness.com/

[53] Powermat,[Online]. http://www.powermat.com/

[54] J. C. Schuder, H. E. Stephenson, Jr., and J. F. Townsend, "Energy transfer into a closed chest by means of stationary coupling coils and a portable high-power oscillator," *Trans. Amer. Soc. Artif. Int. Organs*, vol. 7, no. 1, pp. 327–331, Apr. 1961.

[55] G. Vandevoorde and R. Puers, "Wireless energy transfer for stand-alone systems: a comparison between low and high power applicability." *Sensors and Actuators*, vol.92, no.1-3, pp.305–311, Aug. 2001.

[56] M. Kiani, U. Jow, and M. Ghovanloo, "Design and optimization of a 3-coil inductive link for efficient wireless power transmission," *IEEE Trans. Biomed. Circuits Syst.*, vol. 5, no. 6, pp. 579–591, Dec. 2011.

[57] W. H. Ko, S. P. Liang, and C. D. F. Fung, "Design of radio-frequency powered coils for implant instruments," *Med. Biol. Eng. Computing*, vol. 15, no.6, pp. 634-640, 1977.

[58] G. Lazzi, "Thermal effects bioimplants," *IEEE Eng. in Med. Biol. Magazine*, vol. pp. 75-81, Sept. 2005.

[59] *IEEE Standard for Safety Levels with Respect to Human Exposure to Radio Frequency Electromagnetic Fields, 3 kHz to 300 GHz*, IEEE Standard C95.1, 1999.

[60] Federal Communication Commission, Wireless Medical Telemetry, [Online], Available: http://wireless.fcc.gov/services/index.htm?job=service_home&id=wireless_medical_telemetry

[61] N. N. Donaldson and T. A. Perkins, "Analysis of resonant coupled coils in the design of radio frequency transcutaneous links," *Med. Biol. Eng. Computing*, vol. 21, no. 5, pp. 612–627, Sept. 1983.

[62] C. M. Zierhofer and E. S. Hochmair, "High-efficiency coupling-insensitive transcutaneous power and data transmission via an inductive link," *IEEE Trans. Biomed. Eng.*, vol. 37, no.7, pp. 716-722, July 1990.

[63] C. M. Zierhofer and E. S. Hochmair, "Geometric approach for coupling enhancement of magnetically coupled coils," *IEEE Trans. Biomed. Eng.*, vol. 43, no. 7, pp.708-714, July 1996.

[64] W. J. Heetderks, "RF powering of millimeter and submillimeter-sized neural prosthetic implants," *IEEE Trans. Biomed. Eng.*, vol. 35, pp. 323-327, May 1988.

[65] C. R. Neagu, H. V. Jansen, A. Smith, J. G. E. Gardeniers, and M. C. Elwanspoek, "Characterization of a planar microcoil for implantable microsystems," *Sensors Actuators A*, vol. 62, Issue 1-3, pp. 599-611, July 1997.

[66] G. A. Kendir, W. Liu, R. Bashirullah, G. Wang, M. S. Humayun, and J. Weiland, "An optimal design methodology for inductive power link with Class-E amplifier," *IEEE Trans. Circuits Syst., Reg. Papers*, vol. 52, no. 5, pp. 857–866, May 2005.

[67] S. C. Q. Chen and V. Thomas, “Optimization of inductive RFID technology,” *Proc. IEEE Intl. Symp. Electronics and Environment*, pp. 82–87, May 2001.

[68] M. W. Baker and R. Sarpeshkar, “Feedback analysis and design of RF power links for low-power bionic systems,” *IEEE Trans. on Biomed. Circuits and Systems*, vol. 1, no. 1, pp. 28-38, Mar. 2007.

[69] F. E. Terman, Radio *Engineers Handbook*. New York: McGraw-Hill, 1943.

[70] Z. Yang, W. Liu, and E. Basham, “Inductor modeling in wireless links for implantable electronics,” *IEEE Trans. Magnetics*, vol. 43, no. 10, pp. 3851-3860, Oct. 2007.

[71] M. R. Shah, R. P. Phillips, and R. A. Normann, “A study of printed spiral coils for neuroprosthetic transcranial telemetry applications,” *IEEE Trans. Biomed. Eng.*, vol. 45, pp. 867-876, July 1998.

[72] J. A. Von Arx and K. Najafi, “A wireless single-chip telemetry-powered neural stimulation system,” *Digest IEEE Intl. Solid-State Circuits Conf.*, pp. 214-215, Feb. 1999.

[73] M. Töpper, M. Klein, K. Buschick, V. Glaw, K. Orth, O. Ehrmann, M. Hutter, H. Oppermann, K. F. Becker, T. Braun, F. Ebling, H. Reichl, S. Kim, P. Tathireddy, S. Chakravarty, and F. Solzbacher, “Biocompatible hybrid flip chip microsystem integration for next generation wireless neural interfaces,” *Proc. IEEE Elec. Components Tech. Conf.*, pp. 705-708, May 2006.

[74] S. Kim, K. Zoschke, M. Klein, D. Black, K. Buschick, M. Toepper, P. Tathireddy, R. R. Harrison, H. Oppermann, and F. Solzbacher, “Switchable polymer-based thin

film coils as a power module for wireless neural interfaces," *Sensors Actuators A*, vol. 136, pp. 467-474, Nov. 2007.

[75] A. Alomainy, Y. Hao, and F. Pasveer, "Numerical and experimental evaluation of a compact sensor antenna for healthcare devices," *IEEE Trans. on Biomed. Circuits and Systems*, vol. 1, no. 4, pp. 242–249, Dec. 2007.

[76] T. Dissanayake, K. P. Esselle, and M. R. Yuce, "Dielectric loaded impedance matching for wideband implanted antennas," *IEEE Trans. Microwave Theory Tech.*, vol. 57, no. 10 , pp. 2480-2487, Oct. 2009.

[77] S. Soora, K. Gosalia, M. S. Humayan, and G. Lazzi, "A comparison of two and three dimensional dipole antennas for an implantable retinal prosthesis," *IEEE Trans. Antennas Propag.*, vol. 56, no. 3, pp. 622–629, Mar. 2008.

[78] F. W. Casadei, M. Gerold, and E. Baldinger, "Implantable blood pressure telemetry system," *IEEE Trans. Biomed. Eng.*, vol. BME-19, Issue 5, pp. 334–341, May 1972.

[79] J. D. Meindl and A. J. Ford, "Implantable telemetry in biomedical research," *IEEE Trans. Biomed. Eng.*, vol. BME-31, Issue 12, pp. 817–823, Dec. 1984.

[80] H. V. Allen, J. W. Knutti, and J. D. Meindl, "Integrated power controllers and RF data transmitters for totally implantable telemetry," *Biotelemetry Patient Monit.*, vol. 6, pp. 147–159, 1979.

[81] B. Smith, P.H. Peckham, M. W. Keith, and D. D. Roscoe, "An externally powered, multichannel, implantable stimulator for versatile control of paralyzed muscle," *IEEE Trans. Biomed. Eng.*, vol. BME-34, Issue 7, pp. 499–508, July 1987.

[82] K. D. Wise, D. J. Anderson, J. F. Hetke, D. R. Kipke, and K. Najafi, “Wireless implantable microsystems: High-density electronic interfaces to the nervous system,” *Proc. IEEE*, vol. 92, pp. 76–97, Jan. 2004.

[83] L. S. Theogarajan, “A low-power fully implantable 15-channel retinal stimulator chip,” *IEEE J. Solid-State Circuits*, vol. 43, no. 10, pp. 2322-2337, Oct. 2008.

[84] M. Zhou, W. Liu, G. Wang, M. Sivaprakasam, M.R. Yuce, J. Weiland, and M. S. Humayun, “A Transcutaneous data telemetry system tolerant to power telemetry interference,” *the 28th Annual International Conference of the IEEE Engineering in Medicine and Biology Society*, pp. 5884-5887 Sept. 2006.

[85] M. Sawan, S. Hashemi, M. Sehil, F. Awwad, M. Hajj-Hassan, and A. Khouas, “Multicoils-based inductive links dedicated to power up implantable medical devices: modeling, design and experimental results,” *Biomedical Microdevices*, vol. 11, no. 5, pp. 1059-1070, June 2009.

[86] J. Kim and Y. Rahmat-Samii, “Implanted antennas inside a human body: Simulations, designs, and characterization,” *IEEE Trans. Microw.Theory Tech.*, vol. 52, no. 8, pp. 1934–1943, Aug. 2004.

[87] T. Takura, T. Somekawa, F. Sato, H. Matsuki, and T. Sato, “Improvement of communication area for implantable signal transmission system with ferrite chip core,” *J. Appl. Phys.*, vol. 99, p. 08R909, Apr. 2006.

[88] S. I. Kwak, K. Change, and Y. J. Yoon, “Small spiral antenna for wideband capsule endoscope system,” *IEE Electronics Letters*, vol. 42, no. 23, pp. 1328-1329, Nov. 2006.

[89] D. H. Hubel and T. N. Wiesel “Receptive fields and functional architecture of monkey striate cortex,” *J. Physiology*, vol. 195, pp.215-243, Mar. 1968.

[90] E. K. Miller “The prefrontal cortex: complex neural properties for complex behavior,” *Neuron*, vol. 22, pp. 15-17, Jan. 1999.

[91] A. Belayev, I. Saul, Y. Liu, W. Zhao, M. D. Ginsberg, M. A. Valdes, R. Busto, and L. Belayev, “Enriched environment delays the onset of hippocampal damage after global cerebral ischemia in rats,” *Brain Research*, vol. 964, no. 1, pp. 121-127, Feb. 2003.

[92] R. R. Harrison, “The design of integrated circuits to observe brain activity,” *Proc. IEEE*, vol. 96, no. 7, pp. 1203–1216, July 2008.

[93] A. M. Sodagar, K. D. Wise, K. Najafi, “A fully integrated mixed-signal neural processor for implantable multichannel cortical recording,” *IEEE Trans. Biomed. Eng.*, vol. 54, no. 6, pp. 1075-1088, June 2007.

[94] P. Mohseni, K. Najafi, S. J. Eliades, and X. Wang, “Wireless multichannel biopotential recording using an integrated FM telemetry circuit,” *IEEE Trans. Neural Sys. Rehab.*, vol. 13, no. 3, pp. 263-271, Sept. 2005.

[95] M. Yin and M. Ghovanloo, “A low-noise preamplifier with adjustable gain and bandwidth for biopotential recording applications,” *Proc. IEEE Intl. Symp. on Circuits and Systems*, pp. 321-324, May 2007.

[96] [Online]. Available: http://www.trianglebiosystems.com/

[97] N. Chaimanonart, K. R. Olszens, M. D. Zimmerman, W. H. Ko, and D. J. Young, “Implantable RF power converter for small animal in vivo biological monitoring, *Proc. IEEE 27th Eng. in Med. and Biol. Conf.*, pp. 5195-5197, Aug. 2005.

[98] R. E. Millard and R. K. Shepherd, “A fully implantable stimulator for use in small laboratory animals,” *J. Neuroscience Methods*, vol. 166, pp. 168-177, July 2007.

[99] P. Cong, N. Chaimanonart, W. H. Ko, and D. J. Young, “A wireless and batteryless 130mg 300μW 10b implantable blood-pressure-sensing microsystem for real-time genetically engineered mice monitoring”, *Digest of technical papers IEEE Intl. Solid-State Circuits Conf.*, pp. 428-429, Feb. 2009.

[100] [Online]. Available: http://minimitter.respironics.com/home/

[101] K. Hatanaka, F. Sato, H. Matsuki, S. Kikuchi, J. Murakami, M. Kawase, and T. Satoh, “Power transmission of a desk with a cord-free power supply,” *IEEE Trans. on Magnetics*, vol. 38, no. 5 , pp. 3329–3331, Sept. 2002.

[102] S. Y. R. Hui and W. W. C. Ho, “A new generation of universal contactless battery charging platform for portable consumer electronic equipment,” *IEEE Trans. on Power Electronics*, vol. 20, no. 3, pp. 620-627, May 2005.

[103] J. Gao, “Traveling magnetic field for homogeneous wireless power transmission,” *IEEE Trans. Power Delivery*, vol. 22, no.1, pp. 507-514, Jan. 2007.

[104] M. Takamiya, T. Sekitani, Y. Miyamoto, Y. Noguchi, H. Kawaguchi, T. Someya, and T. Sakurai, “Design solutions for a multi-object wireless power transmission sheet based on plastic switches,” *Proc. IEEE Intl. Solid-State Circuits Conf.*, pp. 362–363, Feb. 2007.

[105] J. R. Manns, M. W. Howard, and H. Eichenbaum, “Gradual changes in hippocampal activity support remembering the order of events,” *Neuron*, vol. 56, no.3, pp. 530-540, Nov. 2007.

[106] D. McCormick, A. P. Hu, P. Nielsen, S. Malpas, and D. Budgett. “Powering implantable telemetry devices from localized magnetic fields,” *Proc. IEEE Eng. Med. Biol. Soc. Conf.*, pp. 2331–2335, Aug. 2007.

[107] D. Russell, D. McCormick, A. Taberner, P. Nielsen, P. Hu, D. Budgett, M. Lim, and S. Malpas. “Wireless power delivery system for mouse telemeter,” *IEEE Biomed. Circ. Sys. Conf.*, pp. 273–276, Nov. 2009.

[108] S. S. Mohan, M. del Mar Hershenson, S. P. Boyd, and T. H. Lee, “Simple accurate expressions for planar spiral inductances,” *IEEE J. Solid-State Circuits*, vol. 34, no. 10, pp. 1419-1424, Oct. 1999.

[109] P. Pieters, K. Vaesen, S. Brebels, S. F. Mahmoud, W. DeRaedt, E. Beyne, and R. P. Mertens, “Accurate modeling of high-Q spiral inductors in thin-film multilayer technology for wireless telecommunication applications,” *IEEE Trans. Microwave Theory Tech.*, vol. 49, no. 4, pp. 589-599, Apr. 2001.

[110] R. K. Hoffmann, *Handbook of Microwave Integrated Circuit*. Norwood, MA: Artech House, 1987.

[111] S. Gevorgian, H. Berg, H. Jacobsson, and T. Lewin, “Basic parameters of coplanar-strip waveguides on multilayer dielectric/semiconductor substrates, Part 1: high permittivity superstrates,” *IEEE Microwave Magazine*, vol. 4, no. 2, pp. 60-70, June 2003.

[112] I. J. Bahl and R. Garg, “Simple and accurate formulas for a microstrip with finite strip thickness,” *Proc. IEEE*, vol. 65, Issue 11, pp. 1611-1612, Nov. 1977.

[113] H. A. Wheeler, “Formulas for the skin effect,” *Proc. of the IRE*, vol. 30, no. 9, pp. 412-424, Sept. 1942.

[114] W. B. Kuhn and N. M. Ibrahim, “Analysis of current crowding effects in multiturn spiral inductors,” *IEEE Trans. Microwave Theory Tech.*, vol. 49, no. 1, pp. 31-38, Jan. 2001.

[115] R. K. Ulrich and L. W. Schaper, *Integrated Passive Component Technology*, ch11, Hoboken, NJ: Wiley-IEEE Press, 2003.

[116] N. O. Sokal and A. D. Sokal, “Class-E—A new class of high-efficiency tuned single-ended switching power amplifiers,” *IEEE J. Solid-State Circuits*, vol. SSC–10, no. 2, pp. 168-176, June 1975.

[117] Cochlear Corporation, Nucleus Freedom Implant, [Online], Available: http://www.cochlearamericas.com/Products/23.asp

[118] D. M. Pozar, *Microwave Engineering*, ch. 4, 2nd ed., New York, NY: John Wiley & Sons, 1998.

[119] R.A. Normann, E.M. Maynard, P.J. Rousche, and D.J. Warren, “A neural interface for a cortical vision prosthesis,” *Vision Research*, vol. *39*, pp. 2577-2587, 1999.

[120] M. Kiani and M. Ghovanloo, “An RFID-based closed loop wireless power transmission system for biomedical applications,” *IEEE Trans. on Circuits and Systems II*, vol. 57, no. 4, pp. 260-264, Apr. 2010.

[121] F. W. Grover, *Inductance Calculations: Working Formulas and Tables.* New York: Van Nostrand, 1946.

[122] M. Nadeem, T. Thorlin, O.P. Gandhi, and M. Persson, “Computation of electric and magnetic stimulation in human head using the 3-D impedance method,” *IEEE Trans. Biomed. Eng.*, vol. 50, no. 7, pp. 900-907, July 2003.

[123] N. Suzuki, Y. Nagai, Y. Ohtani and Y. Ichinose, “A study on antenna coils for wireless ID tags,” *Microwave Conference Proceedings, Asia-Pacific Conf. Proceedings*, vol. 3, pp. 1077-1080, Dec. 1997.

[124] I. Oppermann, M. Hamalainen, and J. Iinatti, *UWB Theory and Applications.* NJ: Wiley, 2004.

[125] D. Andreuccetti, R. Fossi, C. Petrucci “Dielectric properties of body tissue,” [Online]. Available: http://niremf.ifac.cnr.it/tissprop/#over

[126] Plexon's headstages for multi-channel neuronal recording, [Online]. Available: http://www.plexon.com/product/Headstages.html/

[127] S. B. Lee, H. M. Lee, M. Kiani, U. Jow, and M. Ghovanloo, “An inductively-powered scalable 32-channel wireless neural recording system-on-a-chip for neuroscience applications,” Accepted for publication in *IEEE Trans. on Biomed. Circuits and Systems*.

[128] Research animal, Long-Evens rat [Online]. Available: http://www.criver.com/en-US/ProdServ/ByType/ResModOver/ResMod/Pages/Long-EvansRat.aspx

[129] E. Waffenschmidt and T. Staring, “Limitation of inductive power transfer for consumer applications,” *Proc. European Conf. Power Electronics and Applications*, pp. 1–10, Sept. 2009.

[130] C. P. Yue and S. S. Wong, “On-chip spiral inductors with patterned ground shields for Si-based RF IC’s,” IEEE J. Solid-State Circuits, vol. 33, pp. 734–752, May 1998.

[131] M. Soma, D.G. Galbraith, and R.L. White, “Radio-frequency coils in implantable devices: misalignment analysis and design procedure,” IEEE Trans. Biomed. Eng., vol. 34, pp. 276–282, Apr. 1987.

[132] J. M. Fernandez, and J. A. Borras, “Contactless battery charger with wireless control link,” US patent no. 6184651, Feb. 2001.

[133] K. Gosalia, M. S. Humayun, and G. Lazzi, “Impedance matching and implementation of planar space-filling dipoles as intraocular implanted antennas in a retinal prosthesis,” *IEEE Trans. Antennas Propag.*, vol. 53, no. 8, pp. 2365–2373, Aug. 2005.

VITA

UEI-MING JOW

Uei-Ming Jow received a B.E. degree in electrical engineering from Tatung University, in Taipei, Taiwan in 1999, and a M.S. degree in electronic engineering from the National Taiwan University of Science and Technology in Taipei, Taiwan in 2001. From 2001 to 2006, he joined the Industrial Technology Research Institute in Hsinchu, Taiwan, and worked in Electronics Research & Service Organization as a RF engineer. He was involved at the analysis and design of electromagnetic compatibility for high speed digital circuit as well as embedded RF circuits packaging technology. He is now working towards his Ph.D. degree at the Georgia Institute of Technology. His main research interests are neural and bionic implants, integrated analog circuit design, and wireless implantable biomedical systems.